University of Crete
Department of Physics

Foundation for Research & Technology-Hellas
Institute of Electronic Structure &Laser

PhD Thesis

"Surface acoustic wave devices for gas sensing applications"

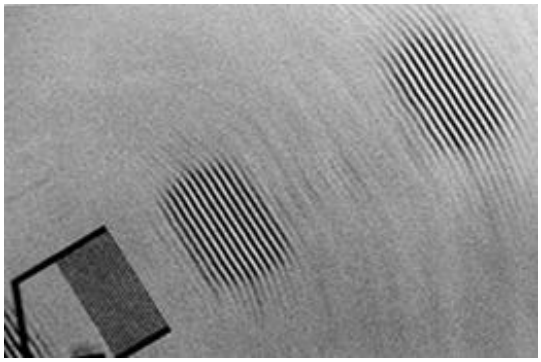

Konstantinos Moschovis

Heraklion

2016

Table of Contents

Acknowledgements

This PhD work has been carried out at the Transparent Conductive Materials and Devices group of the Institute of Electronic Structure and Laser (IESL)/Foundation for Research and Technology-Hellas (FORTH), under the supervision of Professor George Kiriakidis.

First of all I would like to thank my supervisor, Prof. G. Kiriakidis, for his constant interest, ample concern, steady encouragement, critical guidance and above all his long lasting friendship throughout the whole duration of this work and beyond.

In addition, I would like to thank my ex-colleague (now Co-owner at Three99) and friend Dimitris Dovinos for his invaluable help and contribution in setting up the whole experimental apparatus regarding the gas manifold system and the sensitivity raw data measurement acquisition program.

I am also grateful to RMIT University, Melbourne-Australia for hosting in its facilities in Sensor Technology Laboratory, a short part of this experimental work in the framework of a Greek-Australian bilateral collaboration.

Finally, I am deeply grateful to the Physics Department of the University of Crete for giving me the opportunity to broaden my studies and research interests to the highest postgraduate level, and to the Foundation for Research and Technology-Hellas for supplying not only the facilities and means to complete this work but also for the financial support throughout my postgraduate studies.

Scientific output

This work resulted in the following scientific output:

Refereed Journals:

1. V. Binas, I. Kortidis, E. Gagaoudakis, K. Moschovis, G. Kiriakidis, "Ageing resistant InOx ozone sensing films", accepted for publication in *Sensor Letters,* vol.14, No.xx, (2016), doi:10.1166/sl.2016.3665.
2. G. Kiriakidis, K. Moschovis, I. Kortidis, V. Binas, "Ultra-low gas sensing utilizing metal oxide thin films", *Vacuum* 86, Issue 5, (2012), pp 495-506 ***(13 citations*)***
3. I.Kortidis, K. Moschovis, F.A. Mahmoud, G. Kiriakidis, "Structural analysis of aerosol spray pyrolysis ZnO films exhibiting ultra low ozone detection limits at room temperature", *Thin Solid Films*, 518, (2009), 1208–1213 ***(17 citations)***
4. G. Kiriakidis, K. Moschovis, I. Kortidis, and R. Skarvelakis, "Highly Sensitive InOx Ozone Sensing Films on Flexible Substrates", *Journal of Sensors*, Hindawi Publishing Corporation, Volume 2009, Article ID 727893, (2009) ***(5 citations)***
5. G. Kiriakidis, M. Suchea, S. Christoulakis, K. Moschovis, T. Kitsopoulos, J. Stoemenos, "Nano-structural and surface characteristics of non-stoichiometric In_2O_{3-x} thin films", *International Journal of Nanotechnology (IJNT)*, Volume 6-Issue 1/2 (2009), 208-218 ***(1 citation)***
6. G. Kiriakidis, J. Kortidis, K. Moschovis, and D. Dovinos "On the Road to Inexpensive, sub-ppb, Room Temperature Ozone Detectors", *Sensor Letters* Vol.6, No6, (2008), 812–816 ***(6 citations)***
7. M. Suchea, S. Christoulakis, K. Moschovis, N. Katsarakis, G. Kiriakidis, "ZnO transparent thin films for gas sensor applications", *Thin Solid Films* 515, (2006), 551-554 ***(183 citations)***

**citations according to Scopus database*

Book chapter

G. Kiriakidis, K. Moschovis, and S.B. Sadale, "Systems and Set-ups for Effective Sensing Response Applications" (chapter 10), Book Title: *Sensors for Environment, Health and Security-Advanced Materials and Technologies*, NATO Science for Peace and Security-C: Environmental Security, published by Springer in cooperation with NATO Diplomacy Division, 2008

Abstract

Gas sensors have been extensively used to detect and monitor a wide variety of volatile and other radical gases. In particular, gas sensors have a huge variety of applications such as in environmental quality control, public safety, medical applications, automotive applications and for air conditioning systems in aircrafts, spacecrafts, vehicles and houses. According to a recent industrial market report published in 2014 (http://www.grandviewresearch.com/industry-analysis/gas-sensors-market), global gas sensors market size was estimated at USD 1.78 billion in 2013, and is expected to grow at a CAGR of 5.1% from 2014 to 2020.

Technological advances, primarily due to enhanced manufacturing processes and embedded electronics is expected to drive the gas sensors market, for example, in the automotive sector, hazardous emissions led to the framing of legislations for emission control and created the need to monitor gas concentration. CO and NOx sensing devices are deployed for this purpose, contributing to the global revenue growth. In addition, oxygen sensing products are deployed in automobiles for cabin air quality maintenance. Various types of combustible and toxic substances used in industrial processes such as H_2S (Hydrogen Sulfide), NO_2 (Nitrogen Dioxide), etc. pose high risk for workers in the vicinity. Therefore, it is important to continuously monitor concentration of these substances in industrial environments to avoid any mishaps. Demand for these devices in order to ensure occupational health and safety is on the rise across numerous industry production lines such as process and manufacturing industries.

Semiconducting metal oxides (MOs) such as SnO_2, TiO_2, ZnO and In_2O_3 particularly in their slightly off-stoichiometric form, are used for gas sensing applications due to their sensitivity to conductivity changes in an ambient or controllable gas composition, which arises from charge transfer interactions with oxidizing and reducing reactive gases such as O_2, NO_x, CO, H, hydrocarbons (HC), volatile organic compounds (VOC)

and ozone (O_3). The latter is a strong multi-purpose oxidizing gas that plays a fundamental role in the formation of photo-chemical smog in urban polluted areas. The sensitivity and response speed of MO-based gas sensing films strongly depend on film's surface structural and properties (e.g. porosity, grain size, etc).

In the present work a considerable amount of scientific research has been dedicated to a systematic research on the suitability of metal oxide films to be used as an effective active layer on top of a Surface Acoustic Wave (SAW) device aiming to sensing minute hazardous gas concentrations in the parts-per-billion (ppb) range. In_2O_3 and ZnO were the two metal oxide candidates we have focused on in terms of gas sensitivity based on past experience of the group not only on depositing and characterizing these materials but mainly due to their unique properties. These materials were deposited mainly via two methods. Aerosol Spray Pyrolysis (home-made device apparatus) and DC Magnetron Sputtering (Alcatel System) were the two techniques used for depositing ZnO while DC Magnetron Sputtering was used for depositing In_2O_{3-x}. These techniques (especially DC Magnetron Sputtering) were employed due to process stability, excellent film properties, remarkable material's ageing characteristics and trusted experience gained through years on studying various metal oxide materials with the specific sputtering system. World record ultra low (low-ppb) ozone detection limits for both materials were achieved.

Establishing extremely low ozone concentrations of the order of 6ppb through a conventional conductometric technique utilizing In_2O_{3-x} thin films on rigid and flexible substrates and assuring result reproducibility the work proceeded by adopting In_2O_{3-x} as active layer on top of surface acoustic structures and devices to exploit possible further enhancement on the film sensitivity levels. Such an enhancement may result from an induced interaction of the oxidizing/reducing gas molecules with the In_2O_{3-x} selective layer that perturbs the electrical boundary conditions at the surface of the SAW device and consequently may affect critical

propagation characteristics, such as velocity and amplitude of the applied electro-mechanical waves. In this way any changes in the frequency characteristics of the sensing layer may be correlated with a corresponding gas concentration being targeted.

Regarding the applied SAW devices for gas sensing in the present work, two major approaches have been employed. In the first case, layered SAW devices (delay line structures) were fabricated on XY-$LiNbO_3$ wafers. DC Magnetron sputtering was used to deposit In_2O_{3-x} as active layer on the top. Sensors were developed with 20nm and 100nm In_2O_{3-x} film thicknesses operating at the low frequencies of 138.2MHz and 139.6MHz. The above mentioned sensors were examined towards oxidizing gases such as NO_2 and O_3 as well as on reducing gases such as H_2. At a later stage, additional DC sputtered In_2O_{3-x} films with thickness of the order of 100nm were deposited onto commercially available SAW filters operating in a wide range of central frequencies at medium to high values spanning from 139MHz-930MHz. All depositions were carried out under identical conditions and the only parameter varied was the filter's central operating frequency. The filter responses were also tested over a range of operating temperatures again towards oxidizing and reducing gases such as NO_2 and H_2 respectively with varying concentrations demonstrating a remarkable agreement with conventional conductometric techniques.

In conclusion, a high sensitivity in the range of a few ppbs from the combined SAW structures / In_2O_{3-x} sensitive layer coating has been achieved based on a combination of growth parameters and film structure, demonstrating the applicability of this technique to be applied for low gas detection limits.

1. Metal-oxide gas sensors

Today there is an imperative need to control and to monitor the air quality not only in home facilities but also in industrial premises and urban atmospheres in general [1.1], [1.2]. The tightening each year of worldwide environmental regulations has pushed scientific community to develop cost effective and efficient sensors to cover this field [1.3], [1.4]. There are mainly three broad types of gaseous species that should be monitored and detected. Toxic gas species such as CO, SO_2, NO_x, O_3 etc, corrosive species such as CL_2, F_2, HF etc and explosive species such as CH_4, hydrocarbons, nitrous compounds etc. Toxic gases are essentially being monitored in cities and homes, the corrosive gases are being monitored in chemical, petrochemical and food industries and finally the explosive species are associated to public and work security (mines etc).

Among the different useful solid-state sensors, metal oxide (MO) ones have exhibited very encouraging performances on sensing a number of oxidizing and reducing gases. Their operating characteristics, especially sensitivity, are controlled by three independent factors. The ability of the material to absorb the gas and interact with it (the receptor function), the ability of the material to convert the signal caused by chemical interaction of the oxide surface into electrical signal (the transducer function) and finally there are some other phenomena that have to do with peculiarities of the sensor construction itself that can affect inner grains accessibility for the gases detected.

Although there are some drawbacks that affect their overall performance such as selectivity issues, MO gas sensors responding to minute concentrations (ppb range) of specific hazardous gases such as ozone may be very valuable in dedicated applications targeting purification, deodorizing and sterilization processes in water treatment plans, food industry, air conditioning systems, (HVAC), pharmaceutical and chemical industries [1.5].

Ever since Taguchi conceived the idea of semiconductor based metal oxide gas sensors in 1972 [1.6] followed by the pioneering work of Takada in 1989 [1.7], many patents have been developed during the last decades [1.8], [1.9], [1.10] and at the moment it is an item commercialized by many international companies [1.11], [1.12], [1.13]. In addition, a considerable amount of research is being published along these lines due to the fact that this technology is broadly interdisciplinary.

Of the wide range of available sensing material growth techniques, RF reactive and DC magnetron sputtering, spray pyrolysis (SP), sol-gel, thermal evaporation, pulsed laser deposition (PLD), chemical vapour deposition (CVD), and aqueous chemical growth (ACG) are the most commonly addressed. From the materials side and in as far as oxidizing gases are concerned, the most promising candidates studied so far are the oxides of In, Sn, W and Zn. The potential of metal oxides to achieving detection limits in the ppb range was demonstrated more than ten years ago by Wlodarski and co-workers [1.14] utilizing In_2O_3 thin films prepared by the sol-gel technique. They reported detectable sensor responses down to 45ppb ozone concentrations at medium range temperatures of around 200°C. Those In_2O_3 ozone sensors were grown on a sapphire substrate with interdigitated comb structures utilizing a conventional conductometric set-up. On the same material grown by RF magnetron sputtering applying the RGTO (Reothaxial Growth and Thermal Oxidation) technique, keeping the substrate at 250°C, the group of Sberveglieri from Brescia [1.15] reported stable, reversible and reproducible responses to ozone with sensitivities in the range of 5-200ppb. However, these devices had shown their maximum sensitivity to ozone at elevated temperatures (400°C) while a 4nm Au coating layer was employed as a catalyst to enhance ozone responses. The same group was also involved on reporting work dealing with thermally evaporated WO_3 thin films for ozone sensing [1.16]. Their results

exhibited a dynamic response to 25ppb ozone for films exposed to a 24hr annealing process at 190°C.

Additionally, corresponding work of Aguir and co-workers [1.17] on WO_3 thin films grown by RF reactive magnetron sputtering from a metallic tungsten target exhibited a relative dense surface structure with fine grains of about 30nm and sensitivities to ozone of the order of 50ppb at temperatures of 200°C and above. Similar research work has been carried out on SnO_2 targeting the material nanocomposition and fundamental properties for potential applications in environmental monitoring. In a direct comparison of SnO_2 with In_2O_3, Korotcenkov and co-workers [1.18] have speculated that superior properties in as far as ozone detection is concerned should be expected for In_2O_3 films due to distinct surface structure with the polar nature of a pure oxygen terminated sub-plane exhibiting a low binding energy for some oxygen atoms thus leading to fast response and recovery times and enhanced ozone sensitivity levels.

Indeed, while PLD grown SnO_2 films even doped with Pt demonstrated detection limits not better than 25ppb [1.19], Fechete and collaborators [1.20] in a study on SAW (surface acoustic wave) devices have reported record ozone detection limits of non-stoichiometric In_2O_{3-x} films as low as 10ppb at 230°C, with response and recovery times of less than 1min.

These results have triggered subsequent efforts for optimization of material composition (stoichiometry, crystallinity, porosity, etc) which along with better control of the growth processes may lead to the targeted sub-ppb detection levels. Should that be achieved, metal oxide ozone sensors would have a distinct advantage over their expensive and troublesome spectroscopic counterparts.

Along these lines, encouraging results have been presented by Baraton and co-workers [1.21] on a SnO_2 based chemical sensor composed of 15nm nanoparticles exhibiting sensitivity response to ozone at the 15ppb level at 30%RH. The material was grown by screen-printing technology while the operating temperature was optimized at 120°C.

References

[1.1] T. Nakahara, "Development of gas sensors and cultivation of new markets for air quality", *Proceedings of the 38th Chemical Sensor Symposium* (2004), p.73.

[1.2] H. Akimoto, "Global air quality and pollution" *Science* (2003), Dec 5;302(5651), 1716-9.

[1.3] Directive 2008/50/EC of the European Parliament and of the Council of 21 May 2008, on "*Ambient air quality and cleaner air for Europe*"

[1.4] http://unfccc.int/resource/docs/convkp/kpeng.pdf "Kyoto protocol to the United Nations framework convention on climate change", United Nations 1998.

[1.5] G.S. White, "Ozone", *Handbook of chlorination and alternative disinfectants* p.1203-1261, Fourth Edition, Van Nostrand Reinhold, New York, (1999)

[1.6] N. Taguchi, Gas Detection devices, British Pat.1,280, 809, (1972).

[1.7] T. Takada, "Ozone detection by In_2O_3 thin film gas sensor", *Chemical Sensor Technology* 2 (1989), 59-70, Kodansha LTD. Tokyo.

[1.8] S. Sakai. Patent number: 4535315 (1985).

[1.9] S. Yagawara, W. Ohta, Patent number: 5250170 (1993).

[1.10] M.J. Donelon, P. Kikuchi, M.E. Nottingham, Patent number: 6585872 B2 (2003).

[1.11]http://www.ipm.fraunhofer.de/fhg/ipm_en/solutions_services/proces smonitoring/sensors/index.jsp.

[1.12] http://www.fisinc.co.jp./en/products/basic.html.

[1.13] http://www.figarosensor.com/products/common(1104).pdf.

[1.14] W. Wlodarski, S. Hong-Tao, A. Gurio, W. Gopel, *Inter. Conf. on Solid State Sensors and Actuators*, Issue 16-19, June 1997, p 573 - 576 vol.1, DOI, 10.1109/SENSOR.1997.613715 (1997).

[1.15] G. Faglia, B. Allieri, E. Comini, L.E. Depero, L. Sangaletti, G. Sberveglieri, "Electrical and structural properties of RGTO-In_2O_3 sensors for ozone detection" *Sensors and Actuators B* 57 (1999), 188–191.

[1.16] C. Cantalini, S. Santucci, M. Passacantando, G. Sberveglieri, M. Z. Atashbar, Y. Li, W. Wlodarski, "Vacuum thermally evaporated WO_3 thin film ozone sensor", *Conference on Optoelectronic and Microelectronic Materials and Devices, IEEE Proceedings* (1999), 298-301.

[1.17] K. Aguir, C. Lemire, D.B.B. Lollman, "Electrical properties of reactively sputtered WO_3 thin films as ozone gas sensor", *Sensors and Actuators B* 84 (2002), 1–5.

[1.18] G. Korotcenkov, I. Blinov, M. Ivanov, J.R. Stetter, "Ozone sensors on the base of SnO_2 films deposited by spray pyrolysis", *Sensors and Actuators B* 120 (2007), 679–686.

[1.19] T.K.H. Starke, G.S.V. Coles "High sensitivity ozone sensors for environmental monitoring produced using laser ablated nanocrystalline metal oxides", *IEEE Sensors Journal* (2002) Vol. 2, No 1, p14-19.

[1.20] A.C. Fechete, S.J. Ippolito, K. Kalandar-zadeh, W. Wlodarski, A.S. Holland, K. Galatsis, G. Kiriakidis, N. Katsarakis, N. Katharakis, *Sensors 2004 Proceedings of IEEE,* vol.3, p.1510-1513.

[1.21] M. I. Baraton, NATO/ASI Vichy (2007), Sept. 16-27.

2. Selecting the sensitive layer

In this chapter all of the scientific work has been dedicated to the extensive research on the suitable metal oxide material to be used as effective active layer on top of surface acoustic wave devices for sensing minute hazardous gas concentrations. In_2O_{3-x} and ZnO were the two metal oxide candidates we have focused on in terms of gas sensitivity due to the past experience [2.1], [2.2], [2.3], [2.4] of the group not only on depositing and characterizing these materials but mainly due to their unique properties. These materials were deposited mainly via two methods. Aerosol Spray Pyrolysis (home-made device apparatus) and DC Magnetron Sputtering (Alcatel System) were the two techniques used for depositing ZnO while DC Magnetron Sputtering was the only method used for depositing In_2O_{3-x}. These techniques (especially DC Magnetron Sputtering) were employed due to process stability, excellent film properties, remarkable material's ageing characteristics and trusted experience gained through years of depositing various metal oxide materials with the specific sputtering system. Ozone detection limits for both materials were examined.

2.1 ZnO thin films grown by DC Magnetron Sputtering

2.1.1 Deposition and sensing parameters

ZnO thin films with thickness up to 1μm were deposited onto Corning glass and silicon substrates in an Alcatel DC Magnetron Sputtering system using a 99.999% pure metallic Zn and ZnO ceramic targets both with a diameter of 150mm. The base pressure of the ultra high vacuum (UHV) chamber was below $5x10^{-7}$mbar while, during the deposition, the pressure was $8x10^{-3}$mbar and the substrate temperature was 27°C (RT). The depositions were conducted under two different plasma current settings (I=0.44A and I=0.25A) and under varying Ar-to O_2 flow ratios. The film thickness was measured using an Alphastep profilometer. The surface morphology (grain size and surface roughness) was measured with a Nanoscope III atomic force microscope (Digital Co. Instruments,

USA). The crystal structure of the deposited films was determined by X-ray diffraction (XRD) using a Rigaku Diffractometer with CuKα X-rays. For conductivity studies all films were deposited onto Corning glass substrates, which had thermally-evaporated NiCr ohmic contacts applied in a UHV chamber evacuated, prior to deposition, to below 10^{-6} mbar.
The apparent changes in the film conductivity were used as a means to determine their sensing responses. Thus two different techniques were applied, namely the direct measure of conductivity (conductometric) analysed below, and the effect of carrier density on the propagation of surface acoustic wave (SAW) presented in detail in section 3. The conductivity measurements were carried out in a special designed reactor [2.5] at room temperature in a home-made system at FORTH. For photoreduction the samples were directly irradiated in vacuum by the UV light of a mercury pencil lamp at a distance of approximately 3cm for 20min in order to achieve a steady state. For the subsequent oxidation, ozone was produced up-stream in the presence of UV and the chamber was backfilled with oxygen and ozone at a pressure of 560Torr. This treatment lasted 40min, after which no further changes of the conductivity could be observed. Finally, the chamber was evacuated and the photoreduction–oxidation cycle described above was repeated a few times. An electric field (1 or $10V \times cm^{-1}$) was applied during the whole cycling procedure to the samples and the electrical current was measured with an electrometer. Current–voltage (I–V) measurements were always performed before the cycling started in order to ensure the ohmic nature of the contacts.

2.1.2 Study of the film morphology

AFM imaging of the surfaces of ZnO thin films deposited at room temperature from metallic and ceramic targets, under varying Ar-to-O2 flow ratios, are shown in figure 2.1.

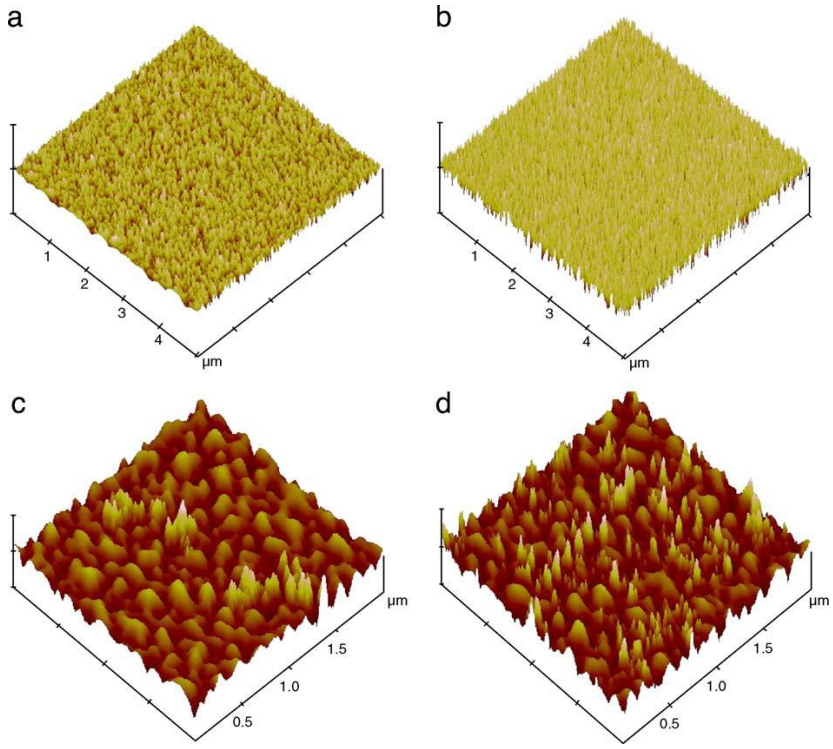

Figure 2.1: AFM 3D images of as-deposited ZnO thin films at room temperature with Ar ratios of respectively (a) 0%, z-range 50nm/div (b) 27% from Zn metallic target, z-range 50nm/div (c) 100%, z-range 30nm/div (d) 90% from ZnO ceramic target, z-range 30nm/div.

AFM characterization for the films deposited from a metallic target (Fig. 2.1a, 2.1b) revealed a granular, polycrystalline morphology with grain size decreasing and roughness increasing as the oxygen partial pressure in the plasma decreases. This characteristic behavior was observed for two different plasma current settings namely I=0.44A and I=0.25A. However, in the case of films grown from a ceramic target (Fig. 2.1c, 2.1d) the surface had a complete different morphology, which was mainly dominated by grain agglomerations and very tall features. The grain size, derived as described above from the AFM measurements, varied from 50 to 20nm for ZnO deposited from a metallic target. For

ZnO films deposited from a ceramic target, agglomeration dimensions varied from 500 to 50nm. The subgrain dimensions were measured and found to be in the range of 10–50nm.

2.1.3 Correlation of growth parameters with film properties

Since the plasma current is correlated with the growth rate in the sense that higher plasma current corresponds to a higher deposition rate, the above microstructural changes are directly attributed to the film growth rate variation.

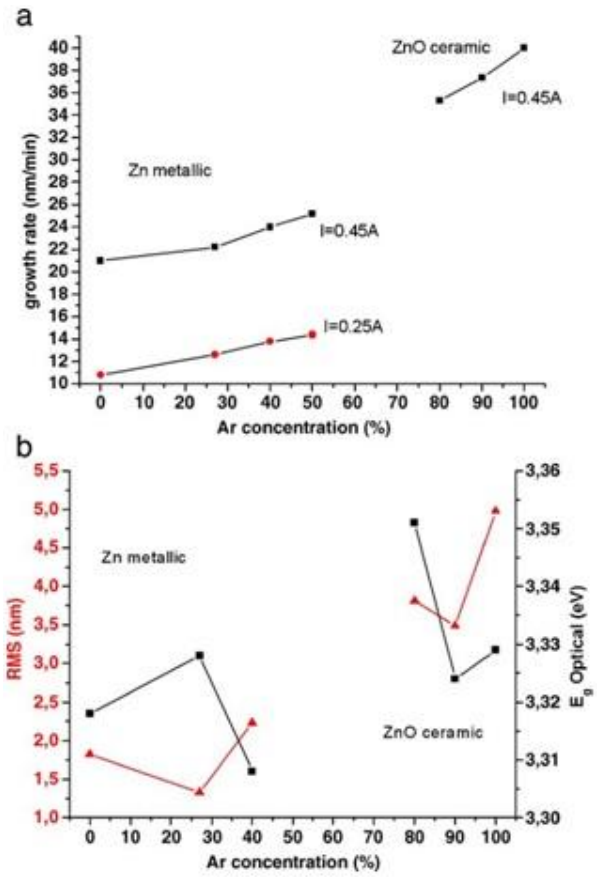

Figure 2.2: (a) Film growth rates versus Ar concentration in plasma, (b) optical band gap (squares) and RMS variations (triangles) versus Ar concentration in plasma.

At the same time, the growth rate increases when the O_2 concentration decreases due to the presence of Ar atoms in the plasma (Fig. 2.2a).
For films grown from a metallic target, we observed that films deposited at higher O_2 ratio (Fig. 2.1a) have shown bigger, better-formed grains,

formed by the aggregation of many small particles, whereas those deposited at higher Ar ratio (Fig. 2.1b) had a uniform grain distribution and smaller size.

For films grown from a ceramic target, the growth rate had a remarkable increase compared with the metallic target case due to the high Ar ion concentration in the plasma. The surface roughness variations of the ZnO thin films deposited at different O_2/Ar ratios are shown in Fig.2.2b (triangles). The scan area for surface roughness was 5×5 μm. One can observe that the surface roughness (RMS) generally increased with increasing Ar concentration in the plasma for both target materials.

The as-deposited ZnO thin films were found to be highly transparent in the visible wavelength region with an average transmittance of 90%. The optical energy gap E_{gap} was derived assuming a direct transition between the edges of the valence and the conduction band, for which the variation in the absorption coefficient with the photon energy hv is given by:

$$a(hv) = A(hv - E_{gap})^{1/2} \quad (1)$$

In Eq. (1), E_{gap} denotes the optical energy gap between the valence and the conduction band. "Tauc" plots of a^2 versus hv give by extrapolation of the linear region of the resulting curve, the optical band gap value E_{gap}. The calculated values of the direct optical energy gap varied between 3.31 and 3.35eV for ZnO thin films depending on target composition and Ar/O_2 ratio. The variations of the optical energy gap could be attributed to changes in the film defect density. In figure 2.2b (squares), the dependence of the optical energy gap on Ar/O_2 ratio for ZnO films grown at RT is depicted. It is observed that films deposited from a ceramic target exhibit, in general, a larger E_{gap}, which can be attributed to the Burstein–Moss shift (BM shift) due to the filling of the lowest levels of the conduction band with carriers in degenerate

semiconductors [2.6]. Moreover, higher O_2 concentration in the plasma leads to more carriers and larger E_{gap} for both target materials.

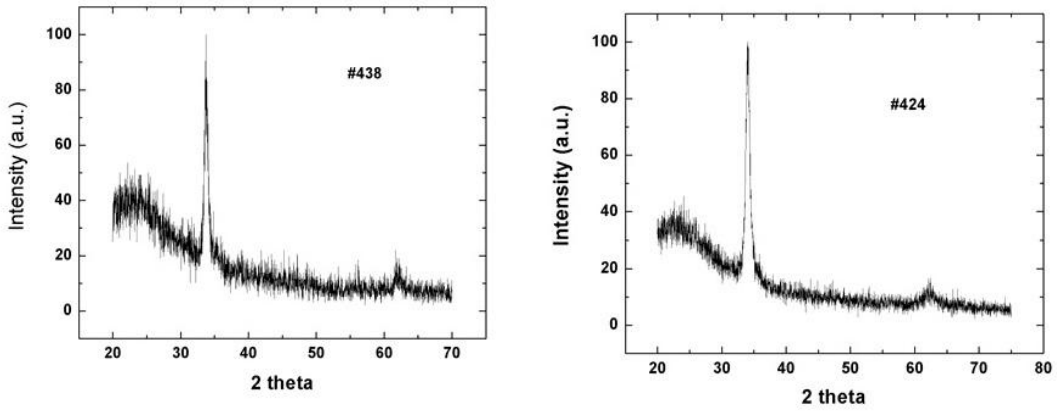

Figure 2.3: The XRD spectra for ZnO films from a) metallic, b) ceramic targets.

The XRD measurements revealed that all deposited films are polycrystalline and show a preferred growth orientation along the c-axis, i.e. (002) plane, which is perpendicular to the substrate (Fig. 2.3).

The effect of the target material and the O_2/Ar gas ratio on the conductivity changes under ozone exposure was studied. In general, the films sputtered from a ceramic target exhibit higher conductivity values (~0.1–10Ω^{-1}cm^{-1}), which are in accordance with already reported values for rf sputtered ZnO films [2.7]. It seems that sputtering from a ceramic target leads to higher carrier concentration and thus to an increased conductivity.

The conductivity results are in agreement with the optical measurements that revealed higher E_{gap} for the films sputtered from a ceramic target due to the presence of carriers inside the conduction band (BM shift). The photoreduction treatment resulted in an increase of the conductivity of up to seven orders of magnitude for ZnO thin films sputtered from a metallic target and only up to three orders of magnitude for ZnO thin films sputtered from a ceramic target. Subsequent ozone oxidation leads to conductivity changes of up to six

orders for the ZnO films sputtered from a metallic target and up to one order for ZnO thin films sputtered from a ceramic target as shown in figures 2.4a,b. This behavior was completely reversible through many cycles of photoreduction and oxidation treatments. The surface-to-volume ratio is smaller in the case of ZnO films deposited from a ceramic target due to the presence of big agglomerates on the surface (Fig. 2.1c,d). This results in the decreased sensitivity for those films, which is observed in figure 2.4b. On the contrary films sputtered from a metallic target display smaller grains and thus show higher surface-to-volume ratio leading to increased sensitivity to ozone according to the Barsan and Weimar model of grain boundary scattering sensing mechanism [2.8].

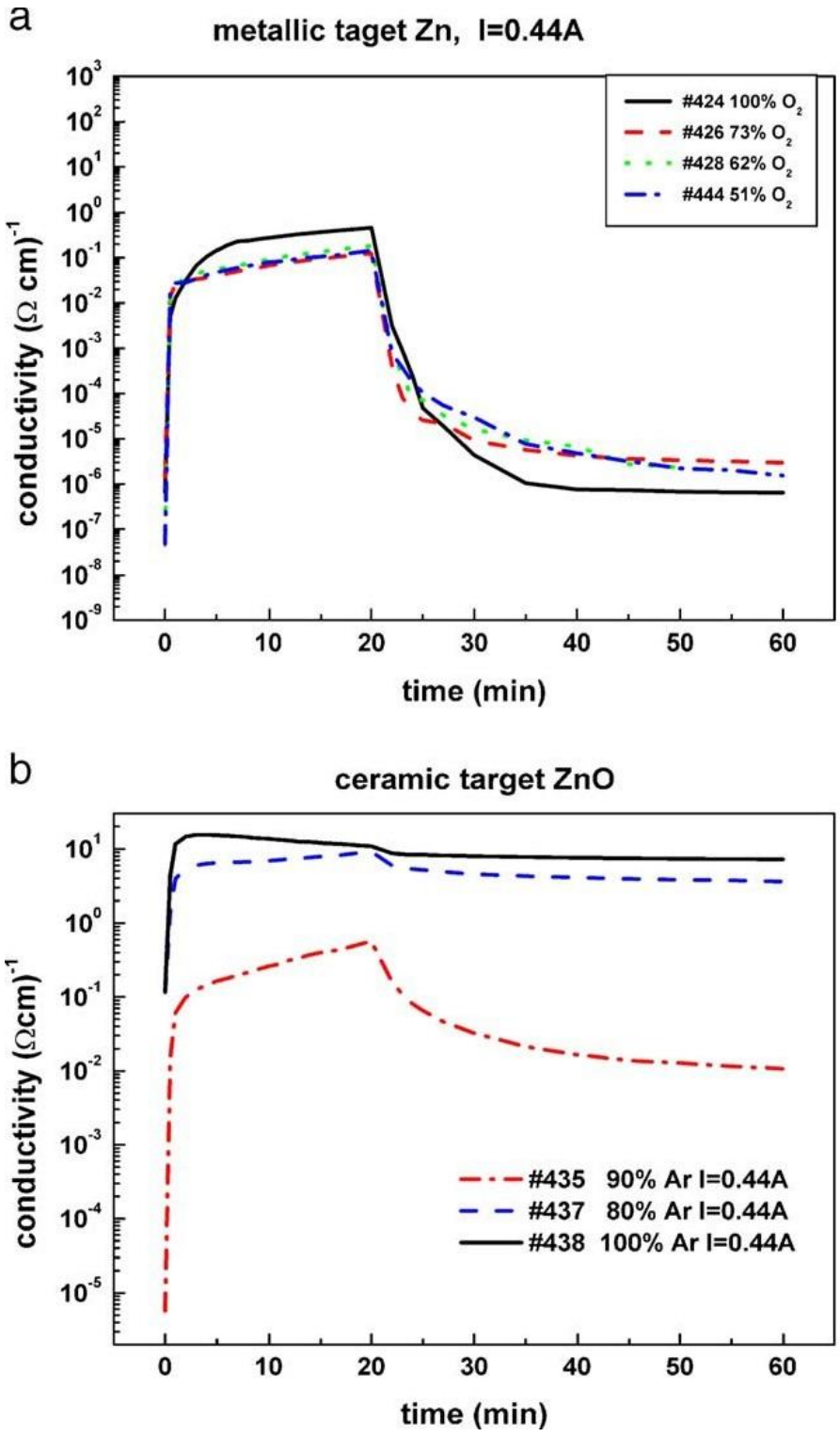

Figure 2.4: Photoreduction/oxidation curves for 100nm films grown from (a) Zn metallic target, (b) ZnO ceramic target.

The morphology of ZnO films, deposited on (100) Si wafers covered by a 3nm-thick SiO_2, was examined by conventional TEM analysis. Figures 2.5a and 2.5b reveal the morphology of a typical 50nm thick film grown

from a 99.999% pure Zn metallic target using 100% O_2 plasma gas with constant flow of 16sccm. Figure 2.6, which shows the diffraction patterns for Fig. 2.5a and 2.5b TEM images, reveals a strong preferred structural orientation. The arc diffraction patterns are superimposed with the diffraction spots of the Si substrate. This configuration permits the indexing of the arcs with high precision. Therefore the film was identified as the hexagonal form of the ZnO. From all the arcs the (0002) one, which is close to the (200)* Si double reflection, has the highest intensity as is evident in figure 2.6. This means that the grains are grown preferentially along the [0001] direction which is almost perpendicular to the plane of the Si wafer. The DF (dark field) micrograph from the arc (0002) depicted in figure 2.7 reveals that the columnar grains extend from the SiO_2 surface up to the film surface. It is worth noticing that near the SiO_2 surface small grains not exhibiting the columnar structure do exist. The mean width of the columnar grains was estimated to be 20nm.

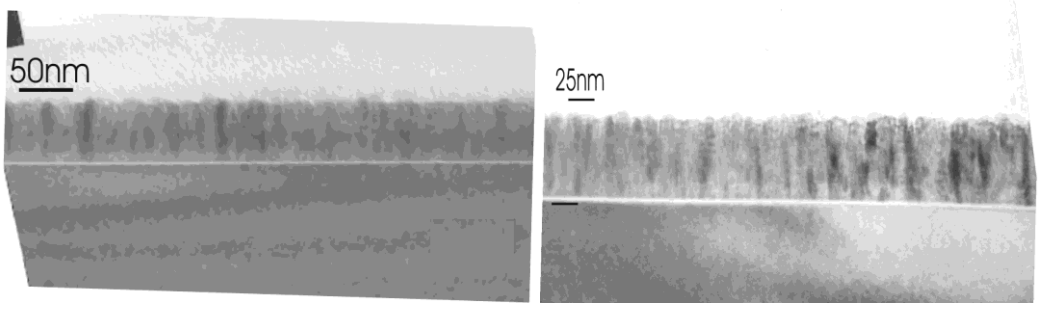

Figure 2.5. (a) TEM images exhibit morphology of a typical 50nm thick ZnO film, (b) images at higher magnification.

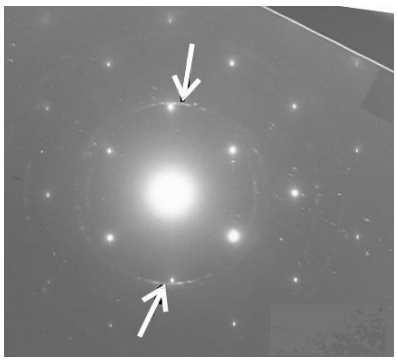

Figure 2.6: Diffraction arcs reveal strong preferred orientation.

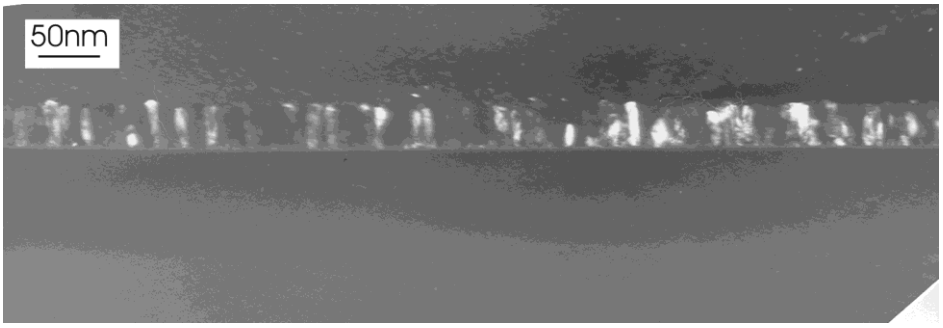

Figure 2.7: Dark Field (DF) micrograph exhibiting ZnO columnar mode structure.

Figure 2.8 illustrates consecutive cycles of photoreduction-oxidation processes for a 325nm ZnO film deposited by dc magnetron sputtering (100%O_2, Zn metallic target) where a conductivity variation of seven orders of magnitude can easily be observed. Each photoreduction lasted 17 minutes while each subsequent oxidation lasted 28 minutes resulting in 45 minutes total cycle duration.

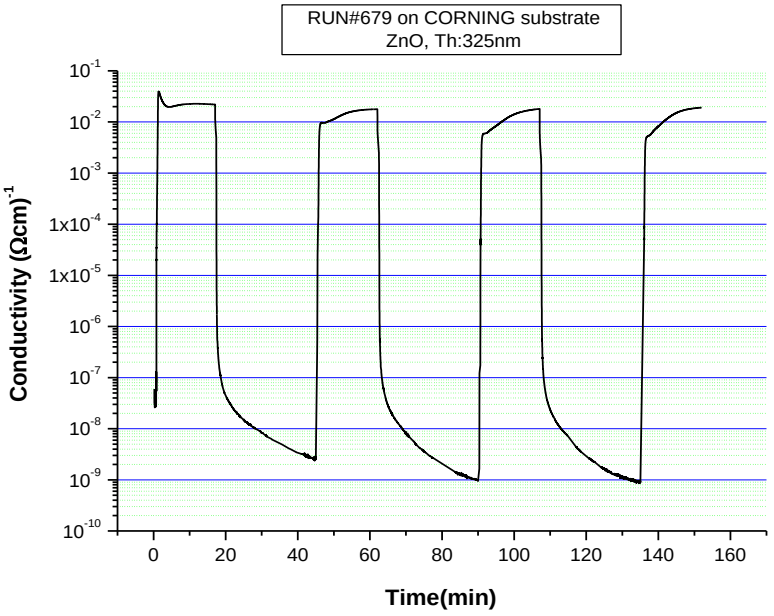

Figure 2.8: Typical photoreduction-oxidation process of a 325nm ZnO film.

All photoreduction-oxidation experiments concerning films were carried out in a specially designed cell fabricated especially for these

measurements. The photoreduction process was carried out at a pressure of 10^{-2}mbar by exposing the films to the UV light of a mercury pencil lamp with an average intensity of 4mW/cm^2 at a wavelength of 254nm, placed at a distance of 30mm from the surface of the films as illustrated in figure 2.9.

For the oxidation process ozone was created by a similar lamp placed away from the sample surface and along the oxygen flow direction. The oxidation process was carried out at a pressure of 800mbar.

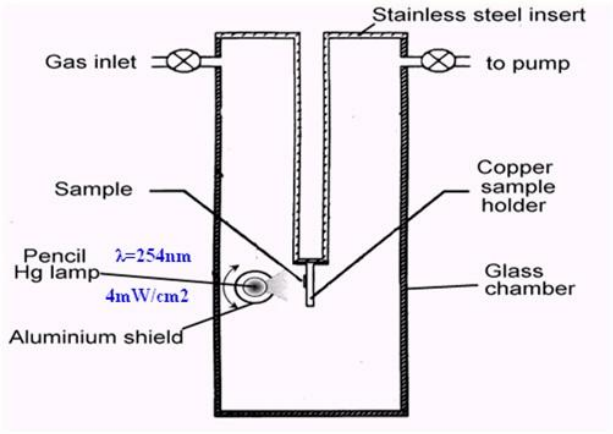

Figure 2.9: Schematic illustration of the apparatus used for the photoreduction-oxidation of thin films.

2.1.4 Correlation of film transport properties with sensing characteristics

In order to establish the film's sensitivity responses towards low and ultra-low ozone levels, two approaches were applied: conductometric and SAW. For the first one, a whole new homemade experimental setup has been designed and implemented. This setup comprised the glass cell shown in figure 2.9, a mass flow controller system with PTFE tubes (Fig. 2.10) and an ozone analyzer delivering accurate ozone levels. The operation of the mass flow controllers as well as the continuous monitoring of the conductivity variations were fully computerized controlled and recorded automatically through a specially developed

labview program. The schematic illustration of this setup is depicted figure 2.11.

Figure 2.10: Mass flow controller system for gas sensitivity.

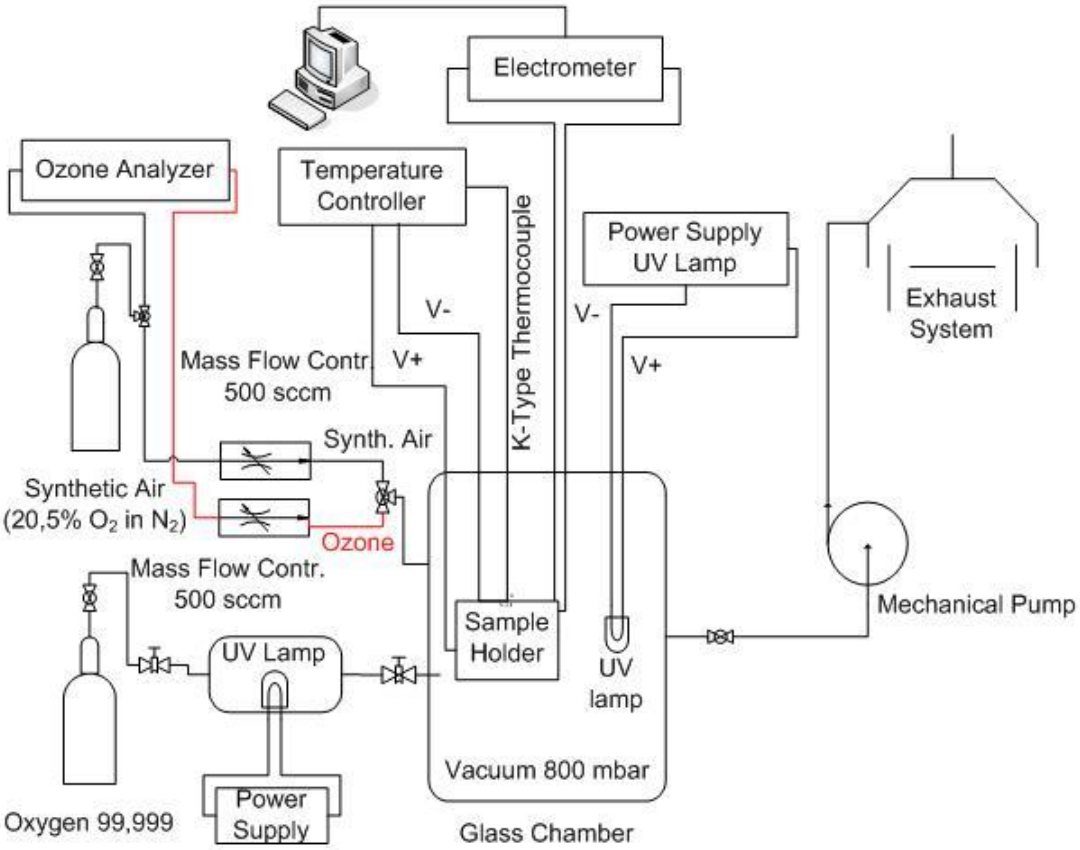

Figure 2.11: Gas sensitivity apparatus.

In order to examine further the potential of the material to be used as active layer on top of surface acoustic wave (SAW) devices, we examined the sensitivity of sputtered ZnO thin films towards extremely low ozone levels utilizing the apparatus of figure 2.11.

Figure 2.12 demonstrates six consecutive cycles of the photoreduction/oxidation process for the ZnO carried out in three different stages. In Stage A, the film is being photo-reduced using a UV pencil style lamp at 254nm (4.5mW/cm^2) at a pressure of ~10^{-2}mbar.

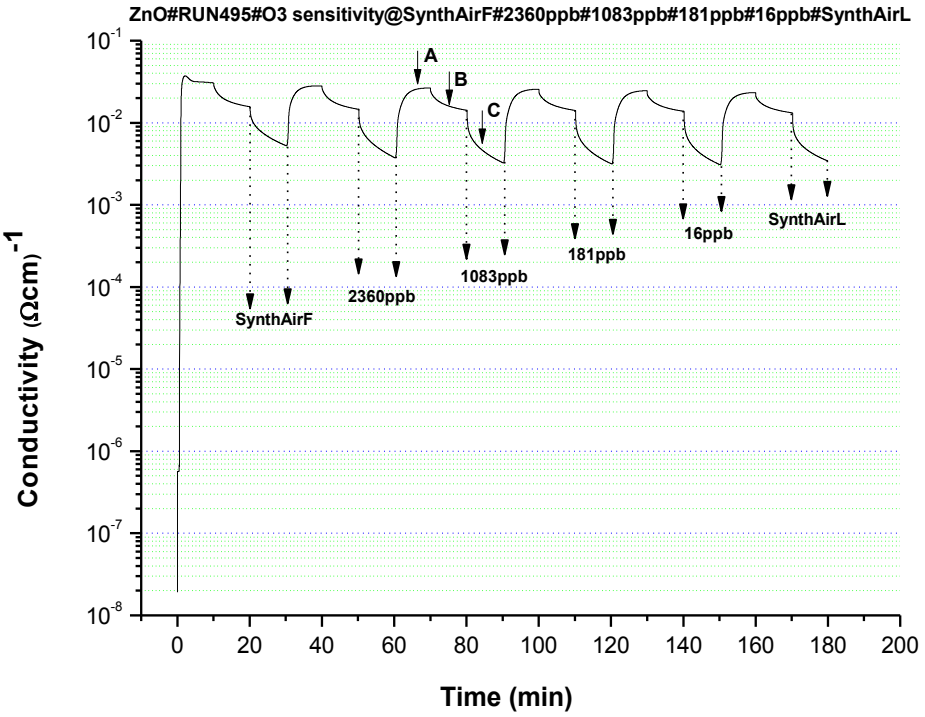

Figure 2.12: Photoreduction-oxidation process of the sputtering grown ZnO films.

In a usual n-type metal-oxide semiconductor (MOS) sensor, environmental oxygen species are adsorbed on the sensor surface and receiving electrons from the MOS. These trapped negative charges cause an upward band bending and an electron-depleted region to reduce the conductance. When the sensor is under UV light, with photon energy larger than the bandgap, the holes created in the MOS will migrate from the bulk to the surface and react with the adsorbed

oxygen species, and the electrons co-produced will be released back to the conduction band of the semiconductor. As a result the conductance will increase as shown in figure 2.13a, for the typical current response of a MOS sensor under UV exposure. Stage A consists of three distinct regions: the fast-rise region (I), the slow-rise region (II), and the constant region (III). Region (I) is attributed to the generation of electron-hole pairs upon excitation with UV light which consequently increases carrier density. Region (II) is due to the hole migration from the bulk to the surface, and recombination reaction between the adsorbed oxygen species. Region (II) is much slower than region (I) since the time needed for a chemical reaction is much longer than that of electronic process. Finally, region (III) is when the concentration of the adsorbed oxygen reaches a dynamic equilibrium in an atmospheric environment (depletion saturated).

The results of this photoreduction stage follow the well-accepted vacancy model based on which conductance rises due to the well accepted vacancy generation process of $O_2 \rightarrow V_0\mu + 2e^- + \frac{1}{2}O_2(gas)$ by which for every oxygen bond breaking a mobile vacancy is formed along with two free electrons leading to an increase of the free carriers within the film [2.2].

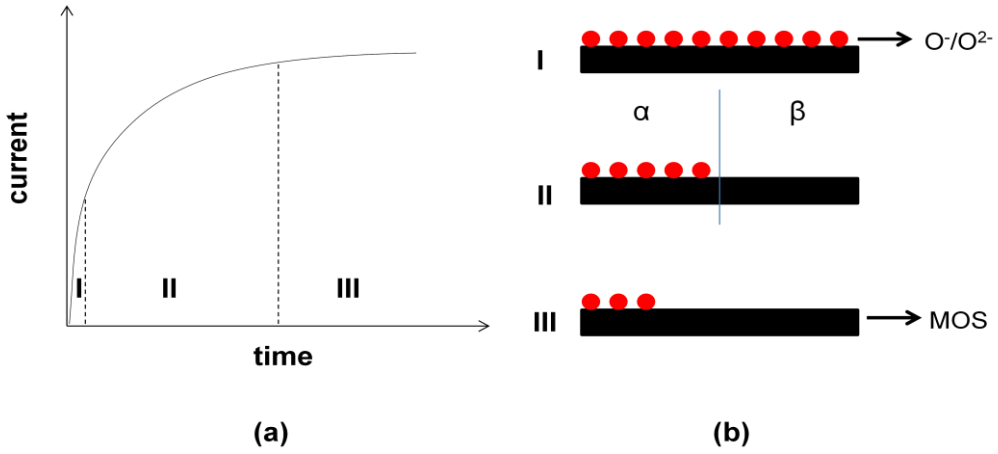

Figure 2.13: (a) Schematic illustration of the current response of a MOS sensor under UV irradiation, (b) Schematic illustration of the adsorbed oxygen species on a MOS sensor surface.

Correspondingly, the schematic concentrations of adsorbed oxygen species in these regions are described in figure 2.13b. Because the carrier generation process takes place much faster than the desorption of oxygen species, the latter can be neglected in region (I), where the surface is dominated by oxygen adsorption. As the time goes on, however, in region (II) a gradual decrease of oxygen concentration occurs, until equilibrium concentration is reached in the atmospheric environment (III). Therefore two types of surfaces can be found on the MOS; α is where the MOS surface is adsorbed with oxygen species and β is without.

In Stage B the UV lamp is switched-off, followed by a reduction in conductivity probably due to an inherent oxidation process associated with absorption of residual oxygen in the chamber. In the final Stage C the film is exposed to four accurately controlled ozone concentrations of 2360, 1083, 181, and 16ppb in synthetic air (20.5%O_2 in N_2) which is used as a reference signal under a flow of 500sccm with subsequent annihilation of vacancies. All measurements were carried out at room temperature (RT).

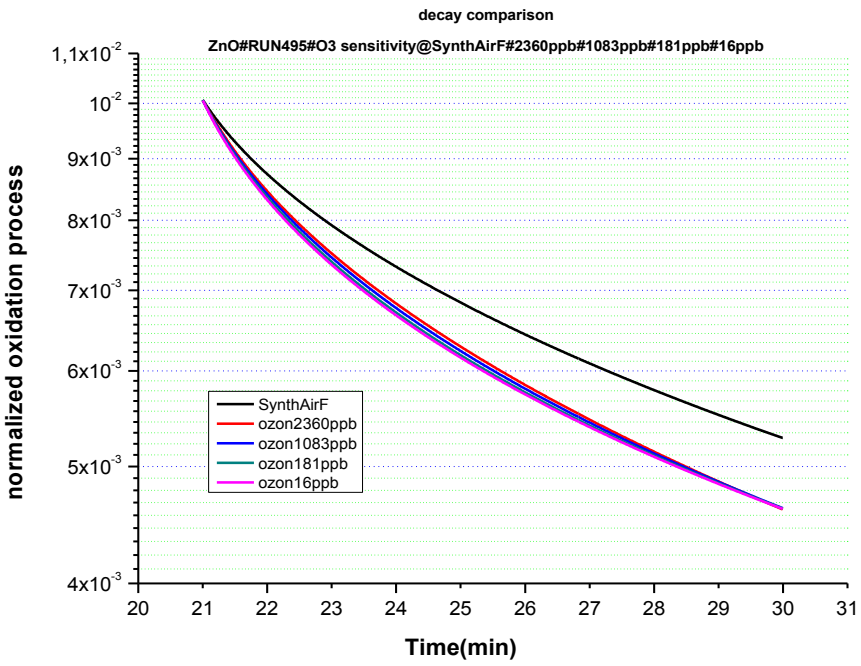

Figure 2.14: Normalized exponential decays from 2360 to 16ppb ozone exposures.

Interestingly, when the exponential decay curves were plotted in a normalized form (Fig. 2.14) it was apparent that there was no clear distinction between the different ozone concentrations denoting a major drawback of the subject material grown by sputtering, in detecting specific accurate ozone concentrations.

For the second sensing approach of SAW, full account of the technique and corresponding results are presented in section 3.

2.2 ZnO thin films grown by Aerosol Spray Pyrolysis (ASP)

The ZnO films, grown by the ASP technique, were fabricated in a home-made aerosol spray pyrolysis system. Figure 2.15 is a detailed schematic of the deposition apparatus and deposition technique [2.9].

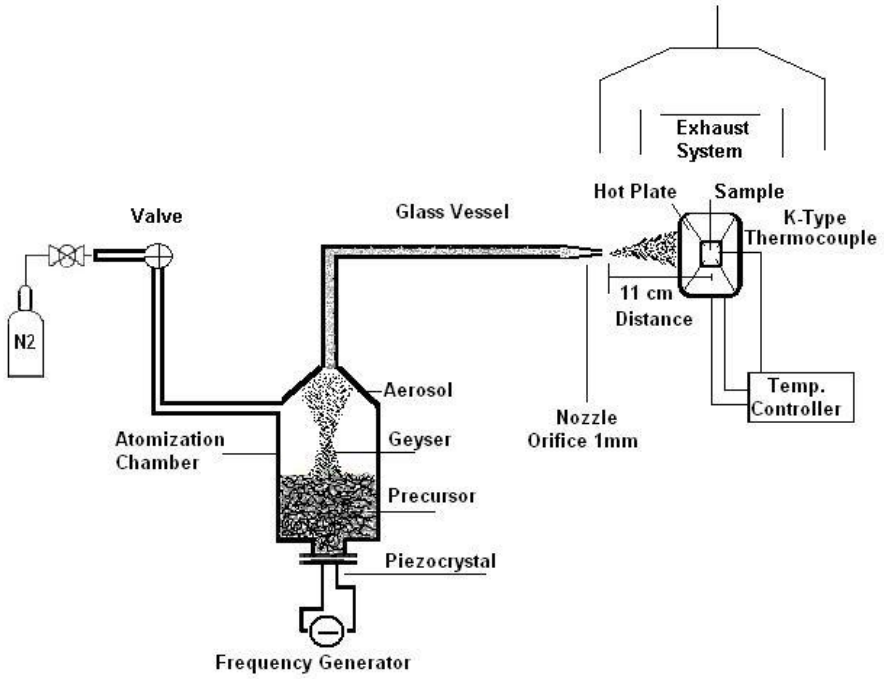

Figure 2.15: Schematic of a home-made aerosol spray pyrolysis system.

In this deposition technique, a starting solution, containing Zn precursors, is sprayed by means of a nozzle, assisted by a carrier gas, over a heated substrate. When the fine droplets impinge on the substrate, the solid compounds react to become a new chemical

compound. Using different deposition times, ZnO thin films were deposited onto Corning glass substrates (25.4×25.4mm^2) with geometrically-ordered NiCr contacts (for conductivity measurements) at 350°C. A solution of 0.1M zinc nitrate dehydrate $Zn(NO_3)_2$ (purity > 99%, Sigma-Aldrich, USA) was used as a precursor, prepared by dissolving it in deionised water. The nozzle was placed at the fixed distance of 110mm from the substrate during deposition. The solution flow rate was held constant at 300ml·h^{-1}. Nitrogen was used as the carrier gas, at a pressure of 0.5bar. When aerosol droplets come close to the heated substrates, a pyrolytic process occurs and highly adherent ZnO films are produced, in line with previous work by Perednis et al. [2.10]. These technological parameters were optimized to guarantee the deposition of films with good adherence, repeatability and reproducibility of their morphological and structural properties in a form suitable for the gas sensor application.

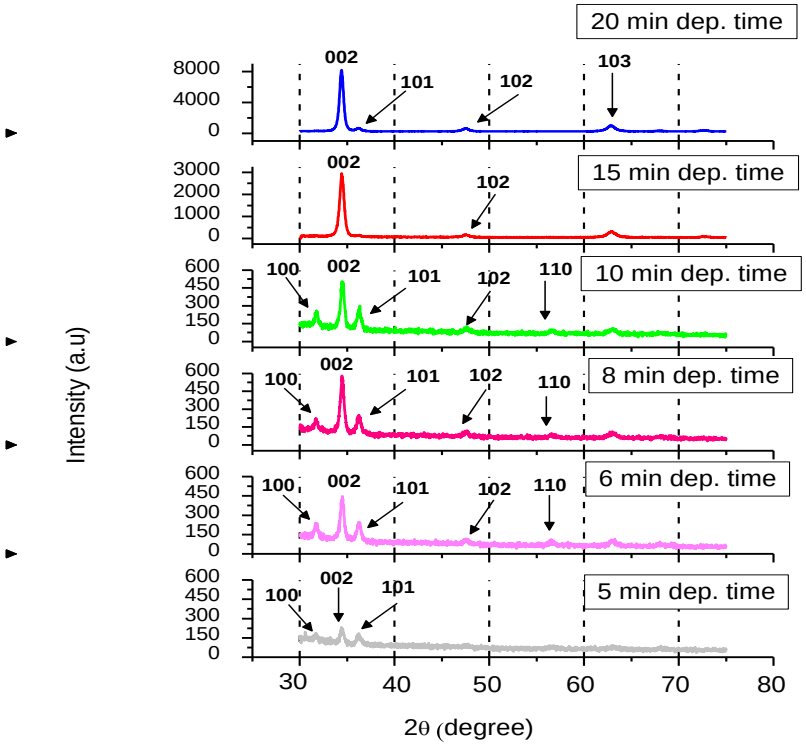

Figure 2.16: XRD characteristic patterns of ASP ZnO films formed using various deposition times.

X-ray diffraction analyses recorded for 2θ values from 30 to 80 degrees are shown in figure 2.16 and revealed that all the films were polycrystalline in nature and free of impurities. It was observed that the intensity of the peaks increased with increasing deposition time of the films, which in turn led to an increase in film thickness which is in line with previous work by van Heerden et al [2.11]. The peaks were identified as the (100), (002), (101), (102), (110) and (103) planes of reflection for a single phase ZnO wurtzite structure [2.12] denoting a clear growth preferred orientation, that of (002) i.e perpendicular to the film substrate.

Additional TEM analysis carried out on these samples revealed once more the films' columnar growth structure as shown in the corresponding bright field (BF) and dark field (DF) micrographs of figure 2.17 and the related diffraction pattern of figure 2.18 where diffraction arcs instead of rings are apparent. Layers parallel to the interface exhibiting dark and bright contrast were also observed and are denoted by arrows in figure 2.17. These layers cannot be attributed to impurities because no other rings except those corresponding to the ZnO compound were detected. These layers can only be attributed to variations in the deposition rate due to instability of the apparatus.

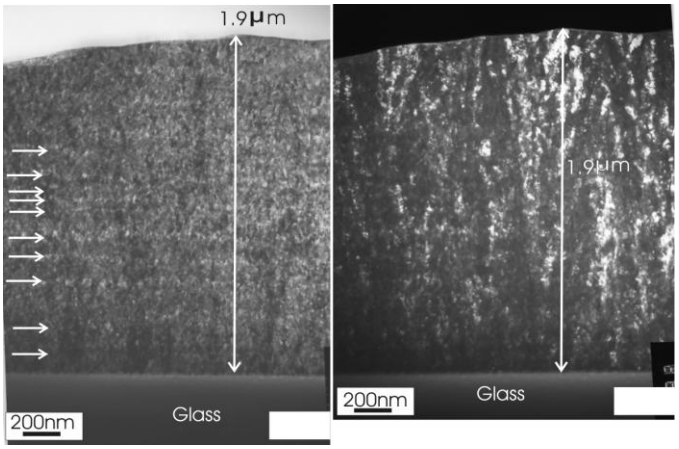

Figure 2.17: Bright Field (BF) and Dark Field (DF) micrographs exhibiting ZnO columnar mode structure.

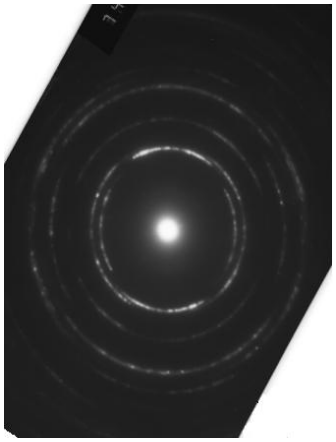

Figure 2.18: Diffraction pattern of ASP grown ZnO exhibiting diffraction arcs indicative of a columnar growth structure.

SEM surface analysis shown in figure 2.19 revealed a circular spreading of the impinging droplets with an average diameter of 70μm. In figure 2.20, the highlighted circled area "A" depicts a higher magnification of the droplet border while figure 2.21 shows the expected highly porous film surface originating from its columnar growth nature. Identical film structures on spray pyrolysis films were reported by Singh et al. [2.13]. The average lateral surface grain size of this highly porous material was of the order of 100nm making these films ideal as gas sensing elements. Indeed, by growing these films on Corning glass substrates with geometrically-ordered ohmic contacts and exposing them to a photo-reducing/oxidation cyclic process, their sensing response to ultra-low ozone concentrations was tested.

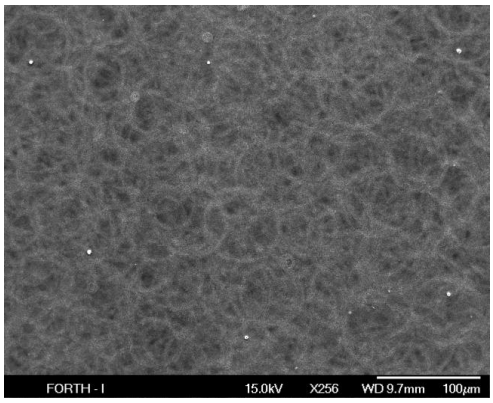

Figure 2.19: SEM image revealing overlapping circular droplet spreading.

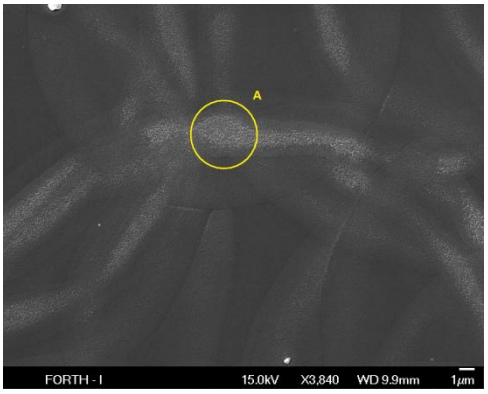

Figure 2.20: Higher magnification droplet overlapping.

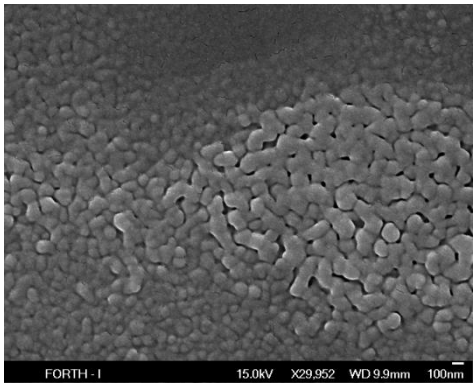

Figure 2.21: Magnification of the area "A" revealing a highly porous film surface**.**

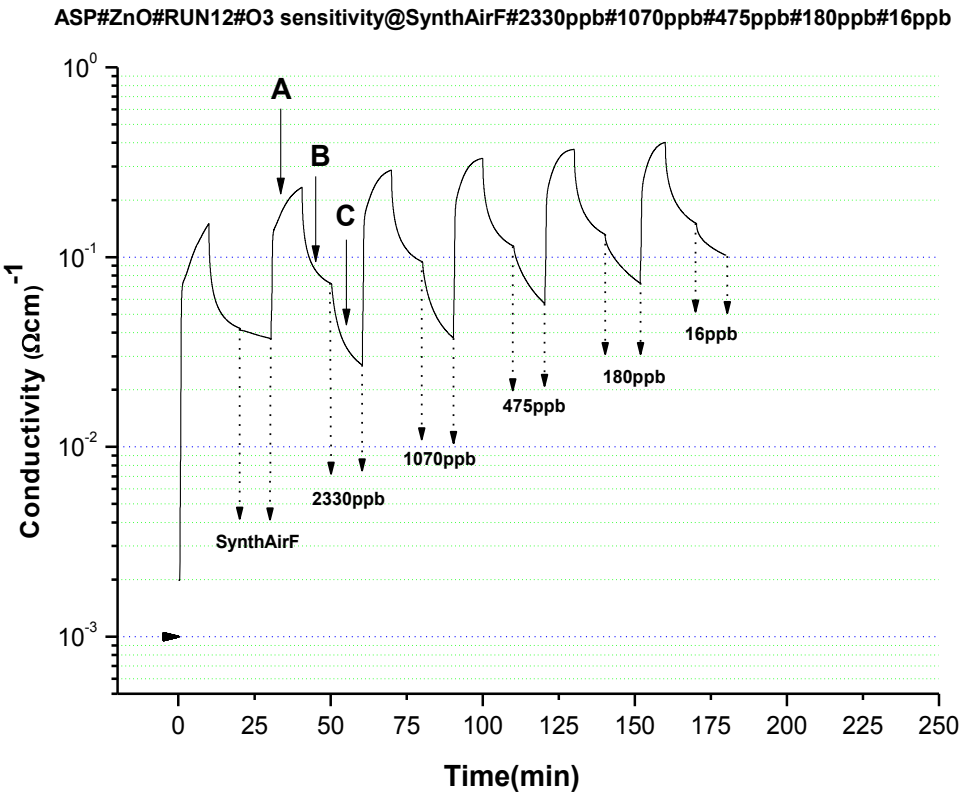

Figure 2.22: Photoreduction-oxidation process of an ASP grown ZnO film.

As in the case of sputtered ZnO films similar sensitivity measurements were carried out for the spray pyrolysis samples. Again, following the three different stages A, B, C described previously, the films were exposed to accurately controlled ozone concentrations ranging from 2330ppb to 16ppb in synthetic air (20.5%O_2 in N_2) which was used as a reference signal. To ensure that these responses were well separated from each other and moreover from the synthetic air carrier gas (introduced into the test chamber under a flow of 500sccm flow), all the exponential decay curves were plotted in a normalized form.

Figure 2.23 depicts the normalized comparison of the exponential decay curves during the oxidation processes at the corresponding ozone concentrations. All measurements were carried out at room temperature (RT). In clear contrast to ZnO films grown by sputtering, for the ASP films there was a clear distinction between the exponential decay curves, denoting the dual ability of these ZnO films both to monitor and

separate the various ozone concentrations down to the very low level of 16ppb and, in addition, to allow resolution of these responses from those of the synthetic air, used as the reference signal.

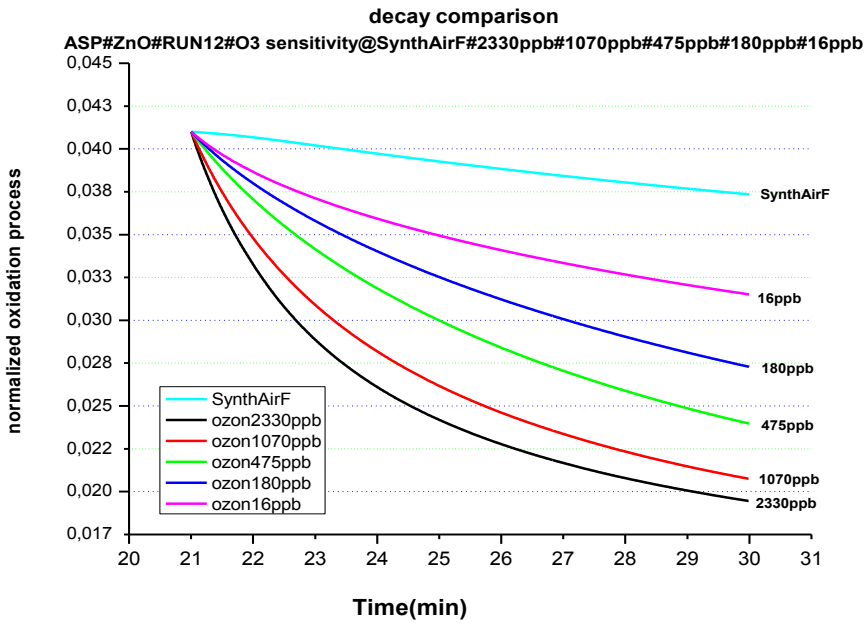

Figure 2.23: Normalized exponential decays from 2330 to 16ppb ozone exposures.

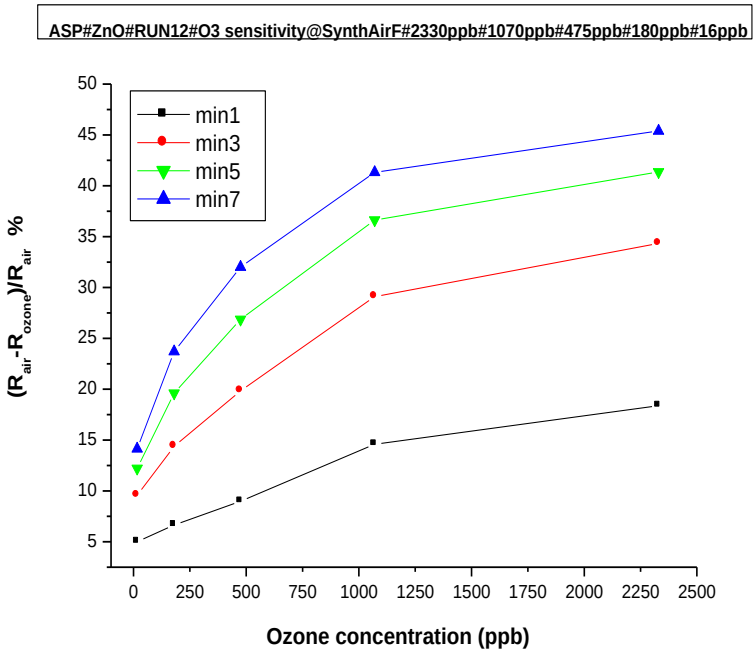

Figure 2.24: Sensing responses at ozone concentrations from 2330 to 16ppb.

Indeed, figure 2.24 represents the recorded ozone responses in the 1st, 3rd, 5th and 7th, minute of the oxidation decay process demonstrating the dynamics of the material to provide reliable readouts even within the first minute of the exposure. It can easily be seen that a 5% sensing response at 16ppb ozone concentration within the 1st minute of the exposure duration is well recorded, as well as a 10% sensing response at the same ozone level concentration within the 3rd minute of the exposure duration. These sensor responses exceed by far those reported by Chien and co-workers on ozone utilizing nanorod ZnO structures [2.14].

This detection limit of 16ppb for spray pyrolysis thin films at room temperature is the lowest ever reported in the open literature for MO gas sensors at RT. Past spray pyrolysis films had demonstrated a grain size of the order of 2μm and thus compared to their sputtering counterparts made of grain sizes of 40 to 100nm were proved to be inferior. In this study the applied ASP technique has produced films with grain sizes of the order of 80nm well within the range of those produced by sputtering. Combination of fine grain sizes together with high porosity with porous sizes of the same order (~100nm) lead to ozone sensing responses of the low ppb range.

In order to verify once more the ability of this material to sense such an ultra low ozone limit, all the measurements have been repeated this time using another sample. Figure 2.25 demonstrates again six consecutive cycles of the photo-reduction/oxidation process for another ZnO spray pyrolysis sample under the same stages A, B, C which have been previously thoroughly described.

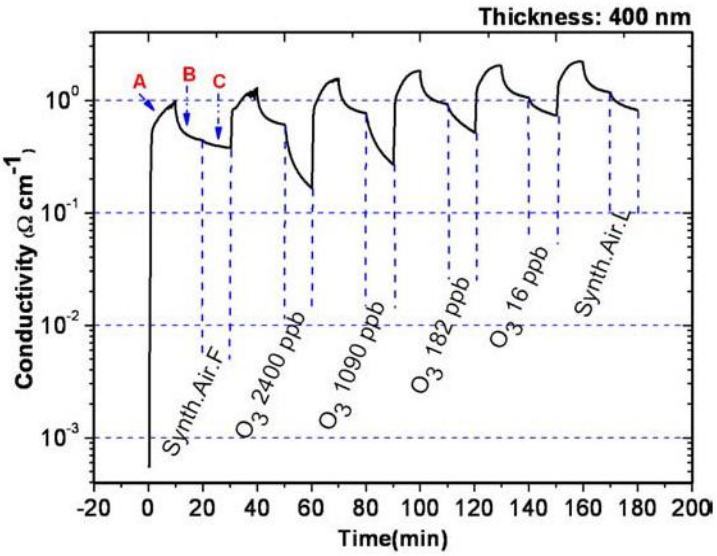

Figure 2.25: Photoreduction-oxidation process of another ASP grown ZnO film.

Once more, figure 2.26 depicts the corresponding normalized comparison of the exponential decay curves during the oxidation processes towards the relative ozone concentrations. All measurements were carried out at room temperature (RT) as in the previous sample.

Figure 2.26 demonstrates again that the rate of response to the different ozone concentrations is characteristic for each one separately, and with a remarkable reproducibility verified experimentally.

Furthermore, the film responses at various concentrations with respect to the synthetic air, plotted as a function of time (Fig. 2.27), has shown once more a satisfactory resolution (3.5% from synthetic air) for the ultra low ozone level of 16ppb within the first minute of exposure which corresponds to a fairly quick detection response time for any practical application.

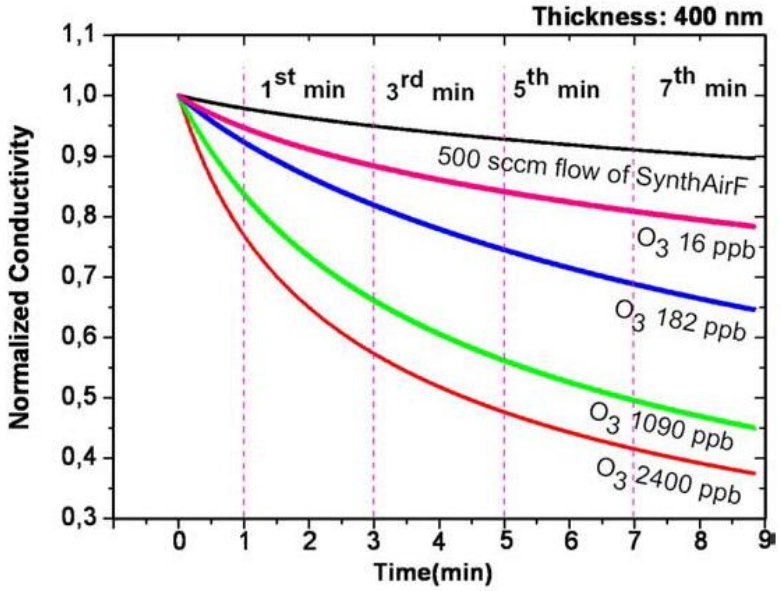

Figure 2.26: Normalized exponential decays from 2400 to 16ppb ozone exposures.

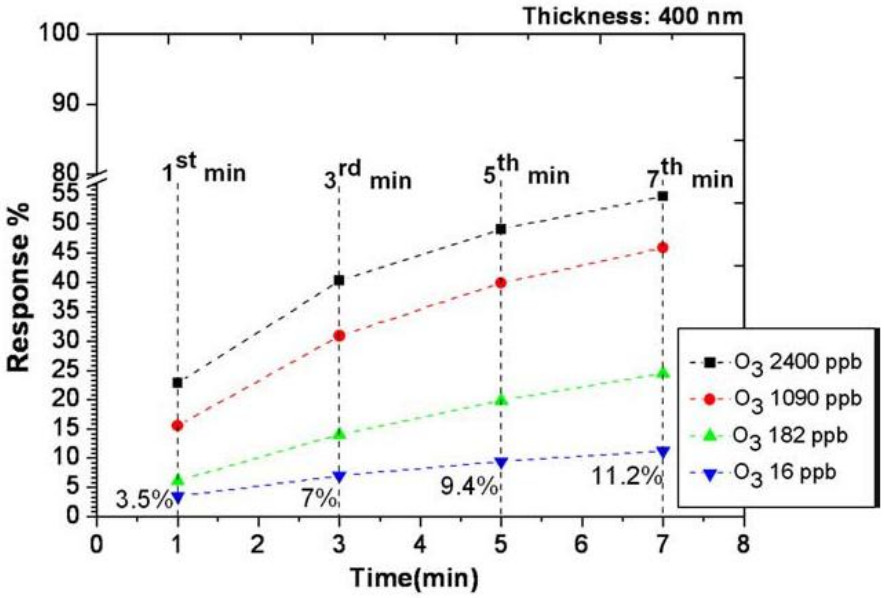

Figure 2.27: Sensing responses at ozone concentrations from 2400 to 16ppb.

Corresponding commercial ozone sensors are claiming a response time of a few minutes and only at high (>8ppm) ozone levels [Ozone Solutions , Inc. M's Ozone Badge].

2.3 In_2O_{3-x} thin films grown by DC Magnetron Sputtering

Similar analysis was carried out for In_2O_{3-x} films grown by dc magnetron sputtering on Corning glass, Si, and flexible (PET) substrates. Figure 2.28 demonstrates the high level of transparency for a thin (240nm) In_2O_{3-x} film deposited on both glass and PET substrates. Optical transparency of more than 85%, detected by UV-VIS spectroscopy was maintained for both substrates and the optical band-gap (E_g) was calculated to be 3.75eV [2.15].

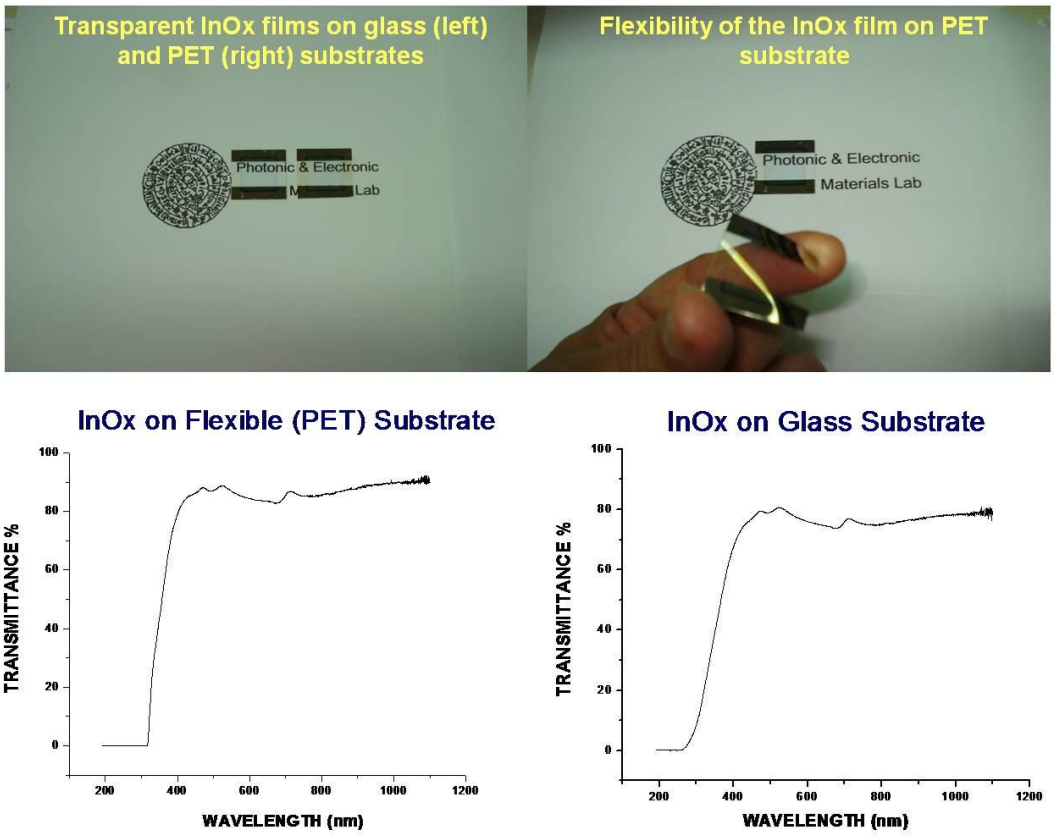

Figure 2.28: Optical transparency of In_2O_{3-x} films on PET substrates (left) and Corning glass (right).

2.3.1 Structural study

Structural analysis, utilizing cross-section TEM (XTEM), carried out in these films revealed a crystalline columnar morphology which is an inherent property of the growth technique independent of the selected substrate. A typical 240nm thick film on Si is shown in the XTEM micrograph in figure 2.29. The following layers were distinguished in this film. Initially an amorphous 8nm thick layer is created at the interface with the Si substrate. This is attributed to a SiO_2 layer, which was formed by inserting the wafer in the oxidizing atmosphere of the chamber. The formation of the crystalline In_2O_{3-x} was confirmed by taking diffraction patterns from the In_2O_{3-x}/Si interface where the diffraction rings from the polycrystalline In_2O_{3-x} were superimposed onto the diffraction spots of the Si substrate, as shown in the inset of figure 2.29. Thus the diffraction rings were indexed having as reference the Si spots and it was found that they correspond to those from the In_2O_{3-x} compound. The 111 In_2O_{3-x} ring, perpendicular to the Si-substrate, is more intense revealing a preferred [111] orientation of the In_2O_{3-x} grains.

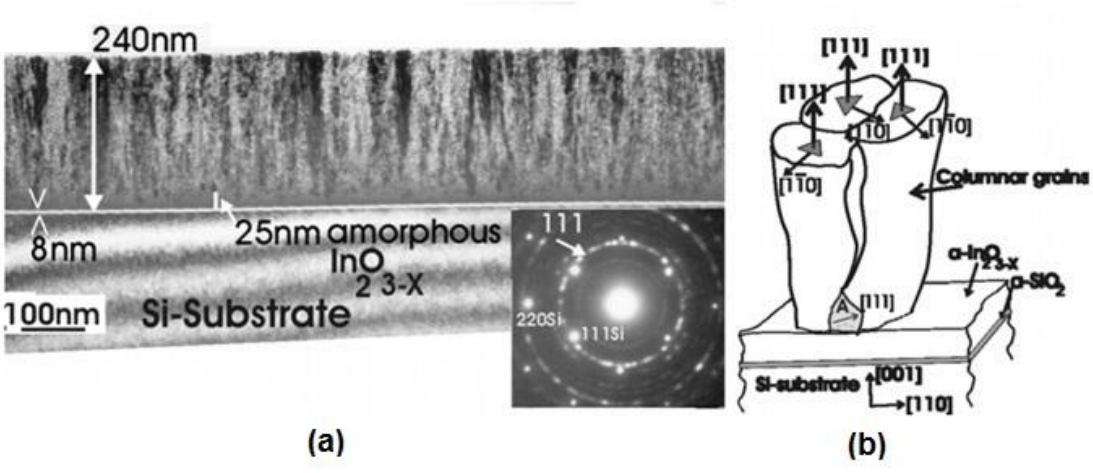

Figure 2.29: (a) XTEM micrograph: the Si wafer has the [001] orientation; film thickness is 240nm and the crystallites are columnar. Between the Si and the In_2O_{3-x} film an 8nm thin amorphous SiO_2 layer is observed. The corresponding diffraction patterns from the Si-substrate and the overgrown film are shown in the inset. (b) Schematic representation of the columnar growth.

The amorphous In_2O_{3-x} near the In_2O_{3-x}/Si interface is shown in higher magnification in figure 2.30a. The amorphous-crystalline interface is rather wavy while frequent rows of voids are observed between the grains (shown by arrows). These rows are denoted by the letter A (insert of figure 2.30a). The mean width of the columnar grains is estimated to be 20nm. This is evident in the dark field (DF) micrograph in figure 2.30b, which was taken from the 111 diffraction In_2O_{3-x} ring. In some cases the grains seem to be significantly wider, as marked by the letter B. In reality they consist of neighbouring slightly disoriented grains as evident in the high magnification micrograph (insert of figure 2.30b).

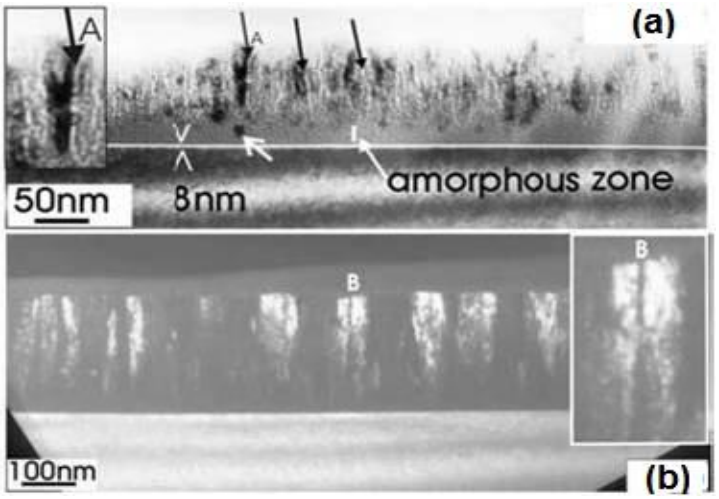

Figure 2.30: (a) High magnification image of amorphous In_2O_{3-x} near the In_2O_{3-x}/Si interface. Rows of vacancies are observed between the grains shown by arrows. In the inset the row A is shown at higher magnification. (b) Dark field (DF) micrograph taken from the [111]-diffraction In_2O_{3-x} ring. The mean width of the columnar grains was estimated to be 20nm. The area denoted by the letter B is shown at higher magnification in the inset.

The In_2O_{3-x} films were also studied via Planar View TEM (PVTEM) observation after thinning the Si-substrate from the backside, first by mechanical ground and then by Ar ion milling, leaving the uppermost part of the In_2O_{3-x} film intact. The morphology of the film is shown in figure 2.31a while the corresponding diffraction pattern is shown in the inset of figure 2.31a. The diffraction rings are the same as these in the

inset of figure 2.29a. Having the electron beam almost perpendicular to the foil, the observed images in figures 2.31a,b are the projections of the columnar grains on the plane of the foil (Fig. 2.29b). Therefore the observed size of the grains by PVTEM corresponds to the width of the columnar grains observed in cross-section. The mean width of the grains estimated from figure 2.31a is also 20nm. This is confirmed from the DF micrograph taken from the [111] ring, shown in figure 2.31b, while grains as small as 13nm and large up to 27nm also exist. Rotating the specimen for 45° around an axis as shown in Figure 2.31c the grains are elongated revealing their columnar character. Also the [111] diffraction ring was split in two intensive arcs shown by arrows in the corresponding diffraction pattern in the inset of figure 2.31c.

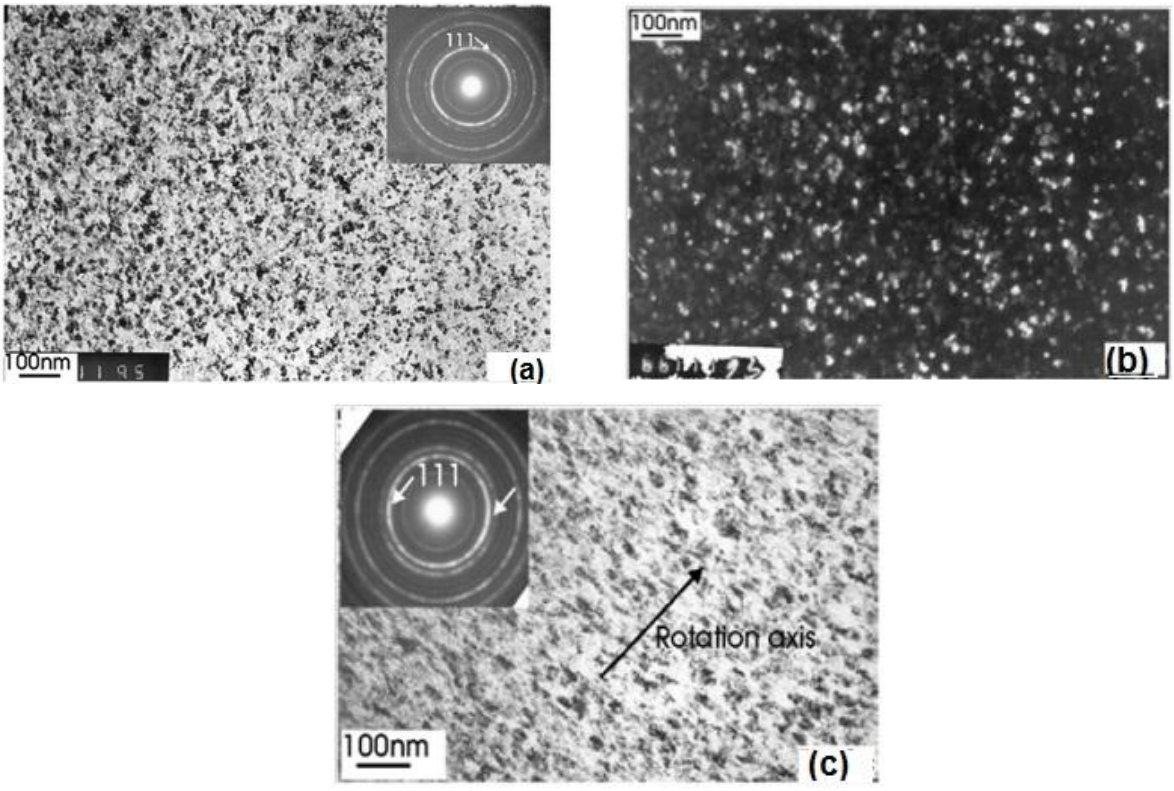

Figure 2.31: (a) PVTEM micrograph: the mean width of the grains is also 20nm. In the inset the corresponding: diffraction pattern (b) DF micrograph taken from the [111] ring. (c) Rotating the specimen for 45° around an axis parallel to the plane of the film, the grains became elongated revealing the columnar character of the grains. The [111] diffraction ring was split in to two intense arcs, shown in the inset.

In the case of the specimens prepared for PVTEM observation part of the In_2O_{3-x} film was also etched from the backside so that the average of the remaining thickness was of the order 100nm. PVTEM specimens exhibiting the total thickness of the In_2O_{3-x} film were prepared by etching the Si substrate by a solution of HNO_3 and HF, which leaved the In_2O_{3-x} film intact. In this case thick areas including the In_2O_{3-x} film and a thin layer of non-etched Si substrate were studied by PVTEM as shown in figure 2.32a. Similarly, partial etching at the grain boundaries having a large portion of vacancies already seen in figure 2.30a cannot be excluded. This explains the fingerprint morphology of the film shown in figure 2.32a.

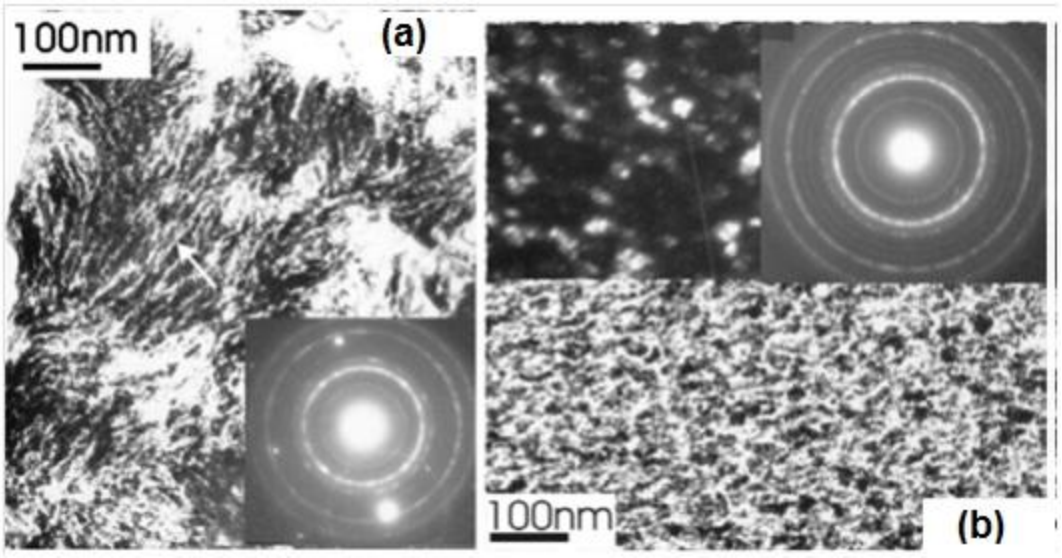

Figure 2.32: (a) PVTEM fingerprint morphology of film on Si prepared by chemical etching. The corresponding diffraction pattern is shown in the inset. Diffraction spots spot the Si-substrate superimposed. (b) PVTEM observations on indium oxide film on NaCl substrate. The thickness of this film is estimated about 150nm. Inset at the right corner, diffraction pattern coincides with the already observed In_2O_{3-x} rings. Inset at the left-hand corner, DF micrograph from the same specimen taken from the (111) ring.

Due to the superposition of the In_2O_{3-x} film and the Si-substrate the related diffraction pattern shown in the inset of figure 2.32, includes both Si spots and rings from the In_2O_{3-x} film. These are exactly the same as in the diffraction rings of the In_2O_{3-x} film thinned by Ar ion beam.

For Indium Oxide films grown on NaCl substrates, film preparation was made by dissolving the NaCl and picking-up the In_2O_{3-x} film on a copper grid; only specimens for PVTEM observation can be prepared by this method. The thickness of this film was roughly estimated to be around 150nm. The morphology of the grains is shown in figure 2.32b and it is very similar with this already observed in figures 2.31a,b.
By tilting the specimens for about 45° the grains take an elongated shape like the observed in figure 2.31c, strongly suggesting that the grains are columnar. This reveals that the columnar morphology is an inherent property of the mode of growth and is independent of the selected substrate. The diffraction pattern coincides with the already observed In_2O_{3-x} rings. The DF micrograph from the same specimen is shown in the inset of figure 2.32b. The mean width of the grains was estimated to be 22nm.
From the TEM characterization we have concluded that In_2O_{3-x} was polycrystalline with a columnar mode of growth and that the film was amorphous in its early stage of growth while turning into crystalline after a critical thickness regardless of the selected growth substrate.
This is mainly attributed to the incubation time, which is needed in order an amorphous material to generate nucleation centres at a given temperature. In the present case incubation time is the deposition time because the specimens were not subjected to subsequent annealing [2.16]. The observed same morphology of the films deposited on Si and NaCl substrates ensures that the procedure for the TEM specimen preparation of the In_2O_{3-x} films on Si does not affect the structure of the films.

2.3.2 Gas sensing analysis

It is well known that the basic mechanism of gas detection is the interaction of the gaseous species with the surface of the semiconducting sensitive metal oxide layer [2.8]. The main mechanism responsible for the observed conductivity changes in these metal oxide films is the formation and annihilation of oxygen vacancies when the film experiences a UV irradiation whose associated energy is higher than the bonding energy between metal and oxygen [2.17]. This leads to oxygen release from the film in the gaseous form, leaving behind two valence electrons in the vacant site. If both electrons remain in the vacancy, the neutrality charge is preserved and the vacancy has zero effective charge. If one or both of the localized electrons are excited and transferred away from the vacancy, the vacancy is left with an effective positive charge. The charged oxygen vacancy (singly or doubly ionized) becomes an electron-trapping site where one or two electrons can be made available for conduction. The formation of doubly charged oxygen vacancies can be applied by the defect equation [2.18] applied to ZnO when exposed to UV light:

$$(Zn^{2+}O^{2-})_{surf} + (h\nu)_{UV} \rightarrow (Zn^{2+}O^{-})_{surf} + e,$$

$$(Zn^{2+}O^{-})_{surf} + (h\nu)_{UV} \rightarrow Zn^{2+} + O_{surf} + 2e,$$

$$2O_{surf} \rightarrow O_{2\,(g)}.$$

On a reverse mechanism a subsequent oxidation in ozone leads to annihilation of the charged oxygen vacancies by incorporation of oxygen into the film by surface recombination, leading to

$$(Zn^{2+}O^{-})_{surf} + O_3 \rightarrow (Zn^{2+}O^{2-})_{surf} + 3/2\ O_{2\,(g),}$$

thus, the charge carrier concentration decreases drastically.

However, since sensitivity is measured in terms of film conductivity which is directly affected by the size of the grain and thus the volume and type of scattering mechanisms that the free electrons are experiencing, it has been shown [2.19] that films with grain size an

order of magnitude larger than the estimated electron mean free path of 3nm (around 20nm in our case) will not be free of grain boundary scattering limitations and thus exhibiting higher conductivity. This is an explanation also for the enhanced gas sensitivities reported below based on In_2O_{3-x} films.

For the case of indium oxide we subjected the films to SIMS analysis (Fig. 2.33) and found out that, in comparison with the bulk composition i.e. over 10nm in depth where the In:O ratio is 0.68 giving a stoichiometry $In_2O_{2.94}$ the non-conducting sample exhibited a surplus of oxygen, for example at 2nm depth the In/O ratio is 0.65 giving a stoichiometry of $In_2O_{3.08}$. This situation was inverted for the conducting sample which now exhibited a deficit of oxygen, for example at 2nm depth the In:O ratio is 0.7 giving a stoichiometry of $In_2O_{2.86}$ [2.20].

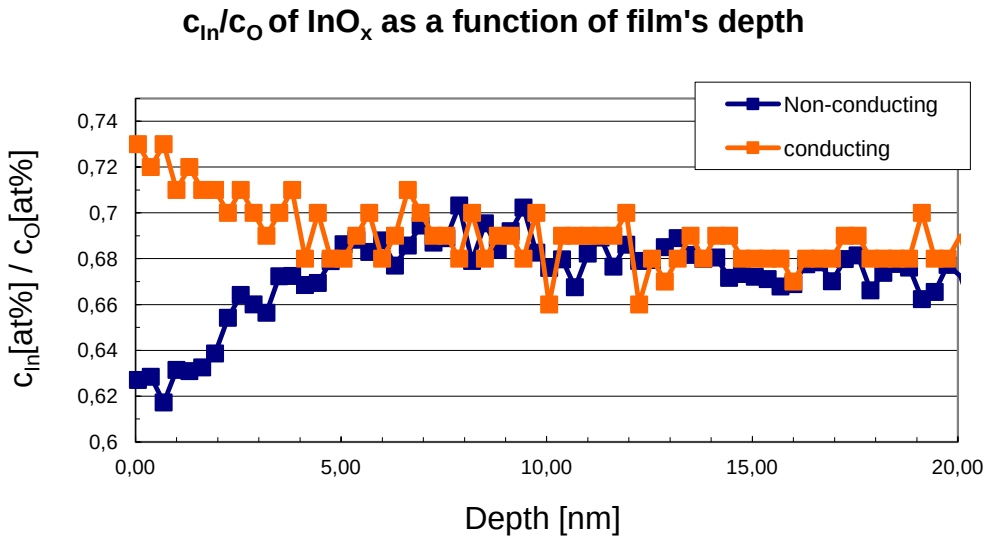

Figure 2.33: In:O atomic ratio as a function of depth in the near surface region derived from SIMS-depth profiles.

This non-stoichiometric characteristic of In_2O_{3-x} and other similar Metal-Oxides such as Zn, studied here too, makes them very active in "redox" reactions since the electron configuration of the solid may be altered. Strong reaction of the material with oxidizing species is expected due to

the material's oxygen deficient surface and therefore a subsequent reduction process, as a rule, leads to the formation of free carriers, which greatly increase the material's conductivity, a fact that is crucial for sensor applications.

Subsequently, In_2O_{3-x} films were tested towards extremely low ozone concentrations in terms of sensitivity, speed of response, repeatability and ageing characteristics.

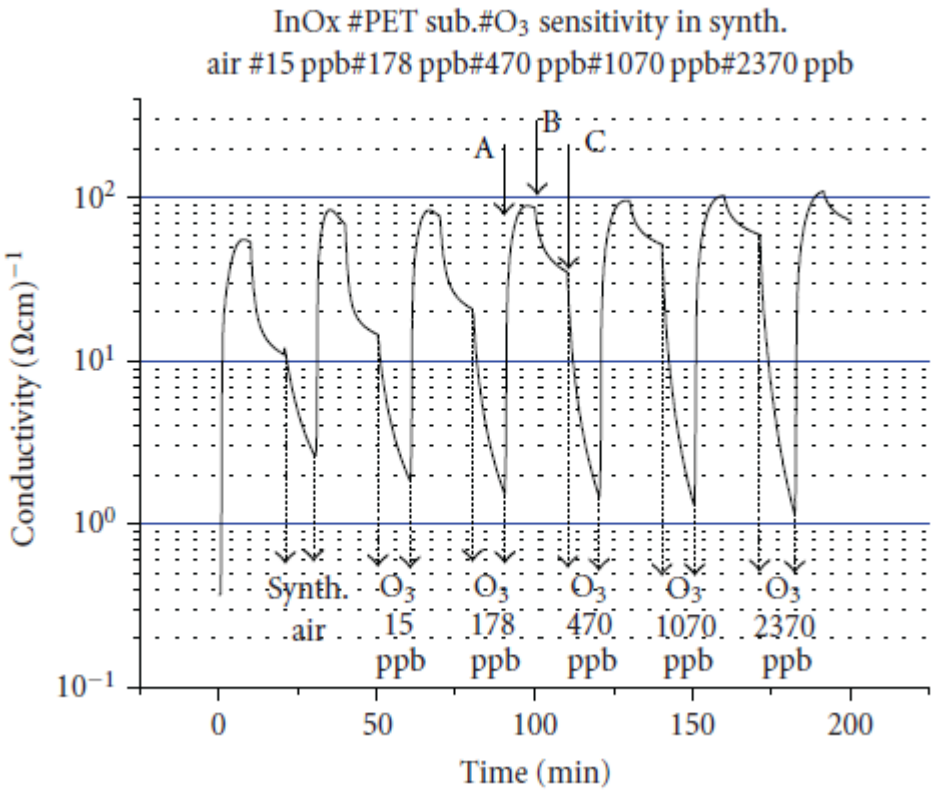

Figure 2.34: Photoreduction-oxidation of the sputtering grown In_2O_{3-x} films.

Figure 2.34 exhibits six circles of photoreduction-oxidation process for the In_2O_{3-x} films in three stages. During photoreduction (stage A), films reach 60% of their steady state conductivity within the first minute and a maximum value of 102$(\Omega\ cm)^{-1}$ after five minutes of the UV light exposure in vacuum. The conductance rise when the film is illuminated with UV light is due both to the generation of free carriers within the film as explained earlier, and to photo-desorption of surface species with a subsequent thinning of the electron depletion layer near the film

surface. Consequently, the applied UV lamp was switched-off (stage B) and a reduction in conductivity of the order of 30% was recorded, probably due to an inherent oxidation process associated by absorption of residual oxygen in the chamber. During the following stage (C) the films were exposed to accurately controlled ozone concentrations in synthetic air (used as reference) ranging from 1070 to 15ppb.

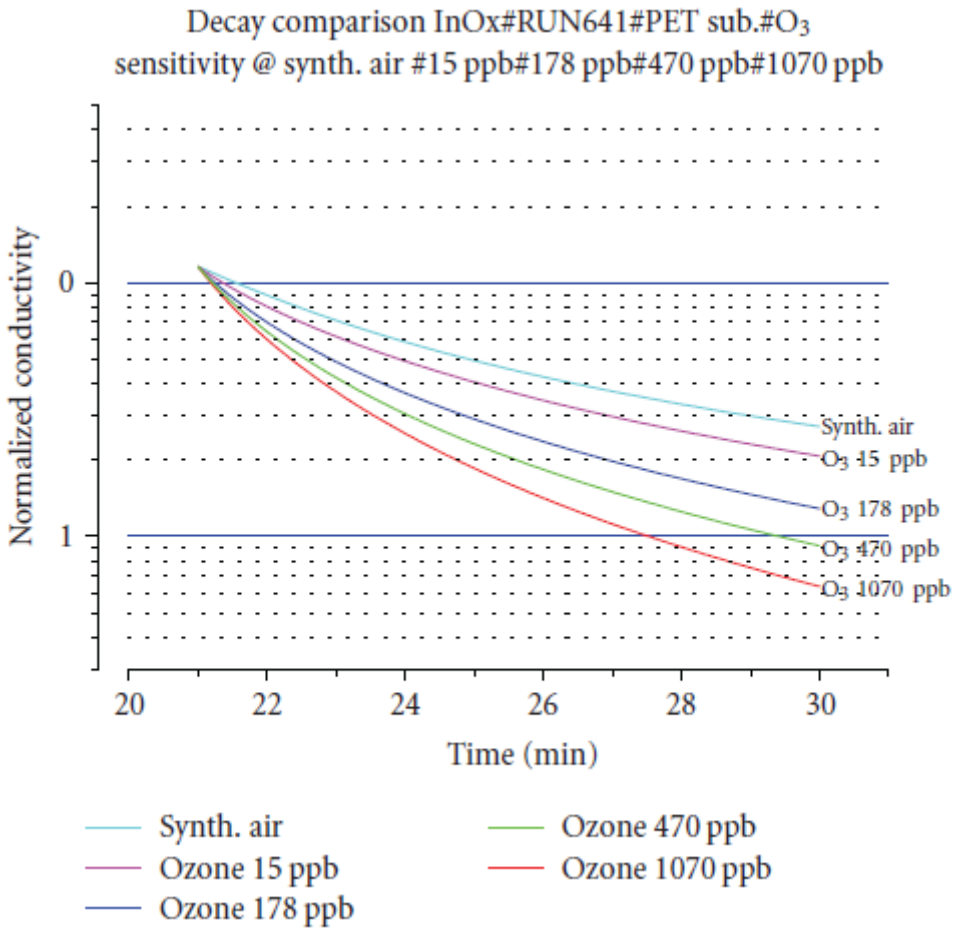

Figure 2.35: Normalized exponential decays from 1070 to 15ppb ozone exposures.

Figure 2.35 shows a normalized comparison of the exponential decays during the oxidation process at the above ozone concentrations. Although previous results utilizing SnO_2 [2.21] and aerosol spray pyrolysis of ZnO [2.22] have shown corresponding sensitivity levels for ozone of the order of 15ppb too, to our knowledge, this is the first time that such extremely low sensing levels are reported for metal oxide thin

films at room temperature (RT) on flexible substrates. The differences in the exponential decay is a measure, on the one hand, of the efficiency of these films to screen the various ozone concentrations down to the extremely low level of 15ppb and on the other, to resolve these responses from the synthetic air, used as reference signal, within the first minute of the analysis.

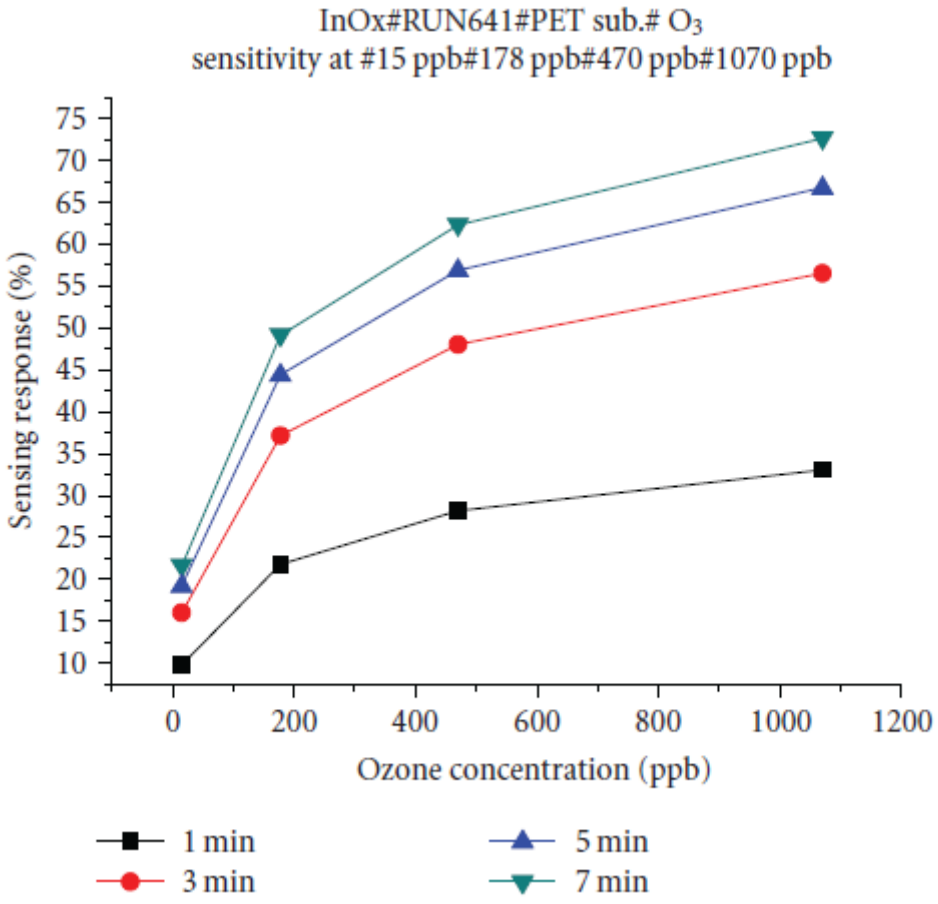

Figure 2.36: Sensing responses at ozone concentrations from 1070 to 15ppb.

Indeed, figure 2.36 depicts the recorded differences in the 7, 5, 3 and 1 minute of the oxidation decay process, demonstrating the material's capacitance to resolve extremely low ozone concentrations (15ppb) while providing reliable readouts (10% sensing response) within the first minute of the exposure time.

In order to prove further the ability of the material to sense yet extremely low ozone concentrations with satisfactory resolution between

closely spaced ozone levels, we have repeated the previous experiment this time using even lower concentration values. Figure 2.37 exhibits five consecutive cycles of photoreduction/oxidation process for In_2O_{3-x} films, towards 6, 16, 60 and 100ppb ozone levels. Figure 2.38 depicts the normalized comparison of the exponential decay curves during the oxidation processes at the corresponding ozone concentrations while figure 2.39 represents the recorded ozone responses in the 1st, 3rd, 5th, 7th, minute of the oxidation decay process. Once more the dynamic ability of the material itself not only to provide reliable readouts even at the ultra low ozone concentration of 6ppb but to separate with satisfactory resolution between closely spaced and extremely low ozone exposures is being demonstrated.

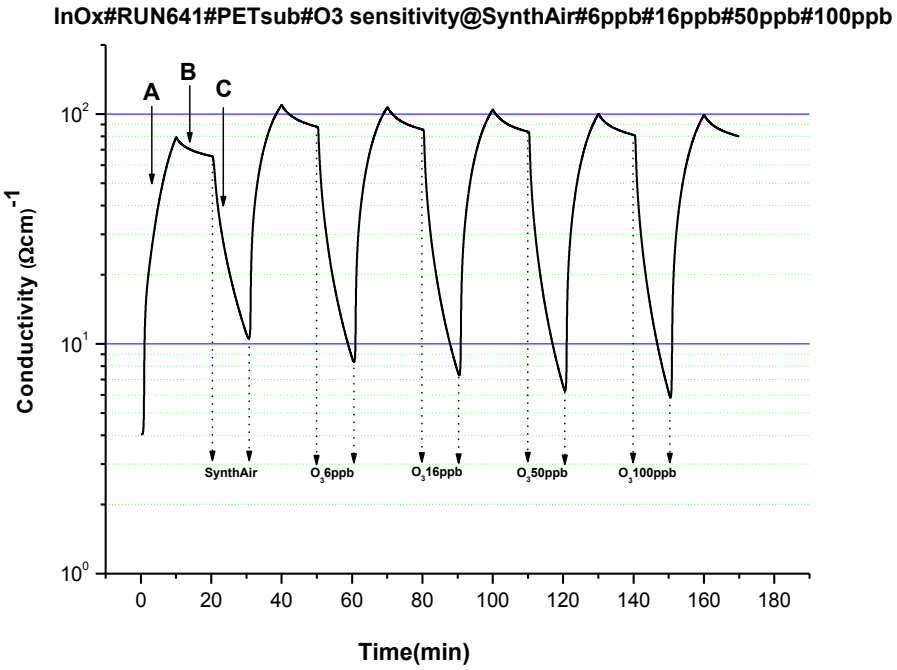

Figure 2.37: Photoreduction-oxidation process of the sputtering grown In_2O_{3-x} films.

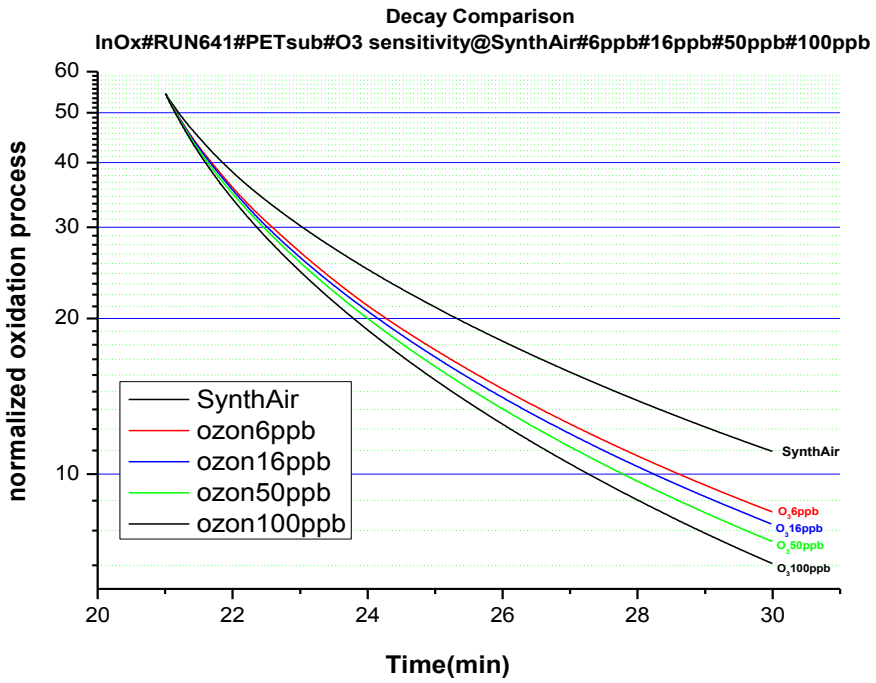

Figure 2.38: Normalized exponential decays from 100 to 6ppb ozone exposures.

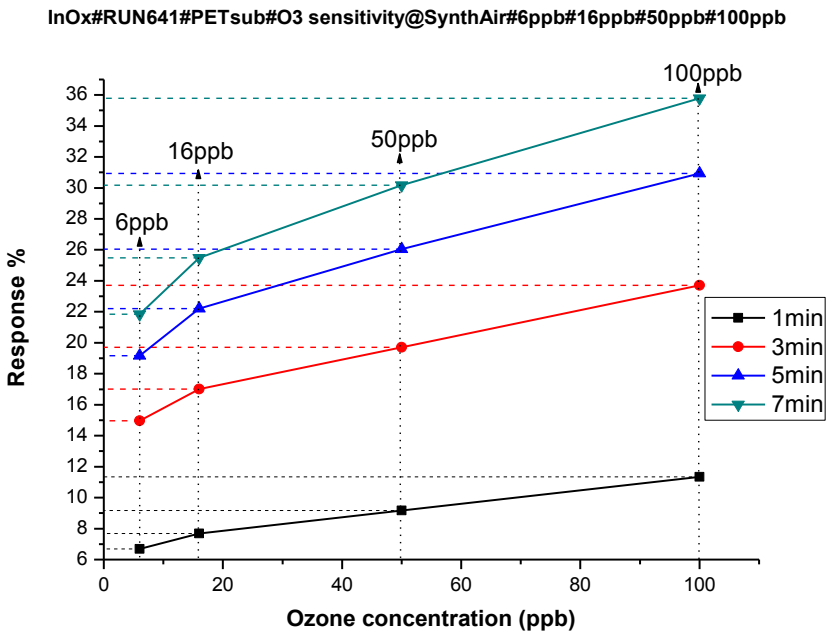

Figure 2.39: Sensing responses at ozone concentrations from 100 to 6ppb.

In order to realize and assess further the ability of the material to sense the extremely low ozone concentration of 6ppb and verify once more the repeatability as well as the reproducibility of our results, additional measurements were carried out.

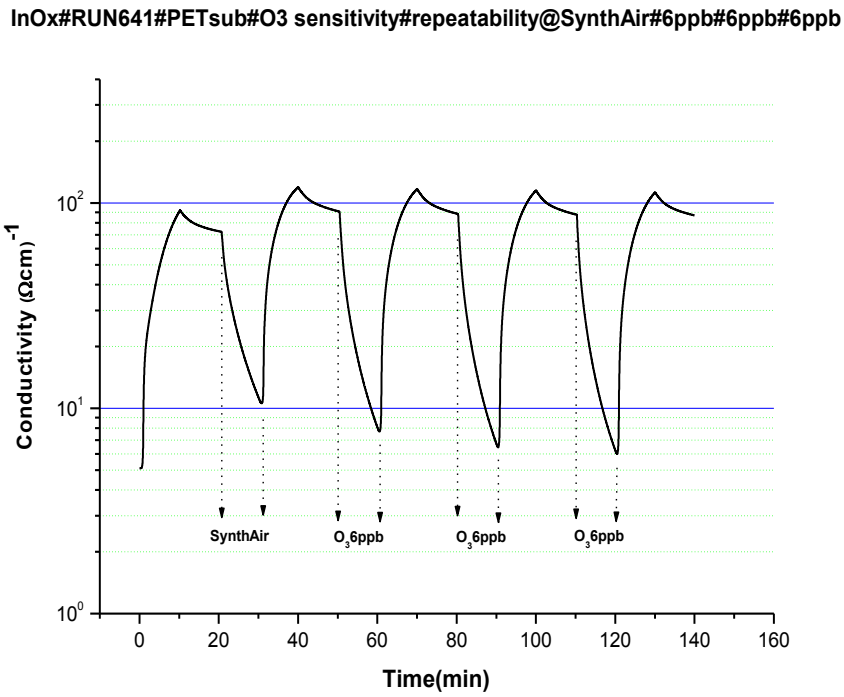

Figure 2.40: Sensor repeatability towards 6 ppb ozone.

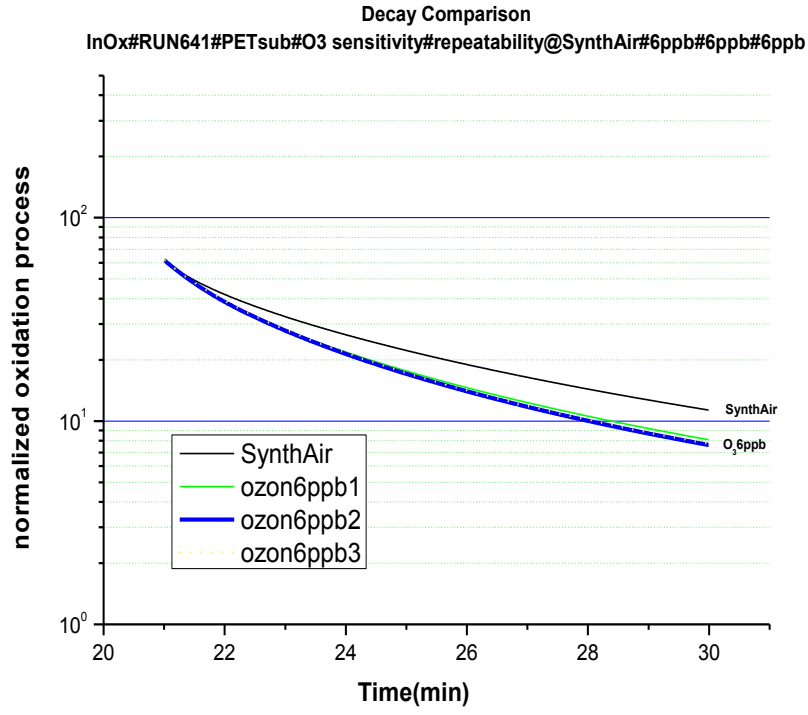

Figure 2.41: Exponential decay overlap towards 6ppb ozone.

Figure 2.40 represents three different and well-separated cycles of the In_2O_{3-x} film exposure towards the same ozone concentration of 6ppb

(again synthetic air is used as reference signal) under the same operating conditions, while figure 2.41 depicts the corresponding normalized comparison plots of their exponential decay curves.

As can be easily observed from figure 2.41, the overlap of the oxidation decay curves is apparent, demonstrating the remarkable ability of the material to reproduce the same signal under the same extremely low ozone concentration of 6ppb (sensor repeatability) as well as its remarkable recovery (Fig. 2.40) back to its original background condition following different exposures.

To our knowledge this is the first time that such extremely low sensing levels are ever reported for metal oxide thin films at room temperature (RT) on flexible substrates.

2.3.3 Ageing of In_2O_{3-x} films

Prior to studying In_2O_{3-x} films as active layers on top of SAW structures, certain key material elements were reevaluated in terms of ageing through a time period of seven (7) years after films fabrication date. Transmittance, surface structure, transport and above all sensing properties were reexamined to verify the retention of the films' technical characteristics. During this seven years period no special storage conditioning measures were taken (Temperature 12-30°C, Relevant Humidity 20% to 60%, Pressure ~1Torr). Any adsorbed species on the surface are expected to be a thin film of contaminants which upon exposure to UV (prior to sensing process) should be desorbed. This is supported also from the fact that no effect of surface contaminants on the film sensing characteristics was detected.

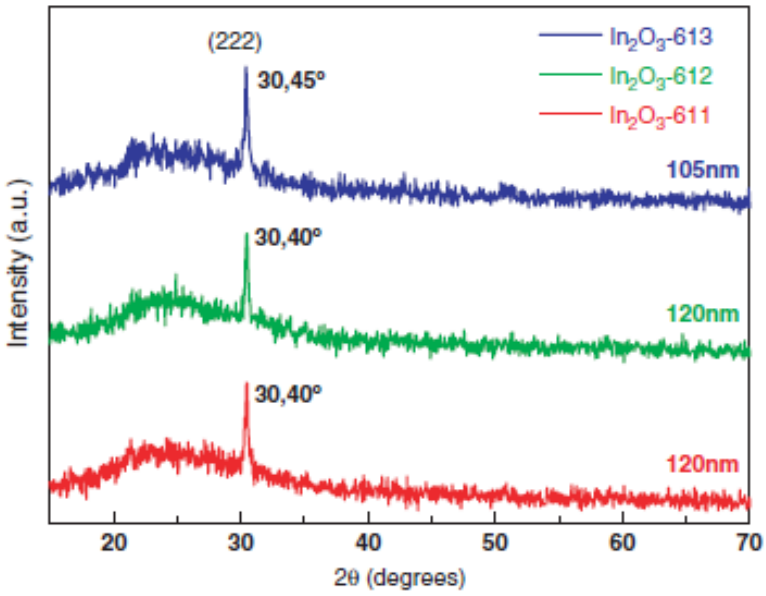

Figure 2.42: XRD patterns of three In_2O_{3-x} films with same thickness and deposition parameters exhibiting consistency of film deposition parameters.

Figure 2.42 reveals the X-ray spectra of a typical set of oxygen deficient In_2O_{3-x} samples of the same thickness and deposition parameters exhibiting a remarkable consistency and reproducibility of the films structural characteristics. Comparable XRD analysis of an initial and

aged representative sample (Fig. 2.43) has revealed, within experimental error, the retention of the film's structural characteristics.

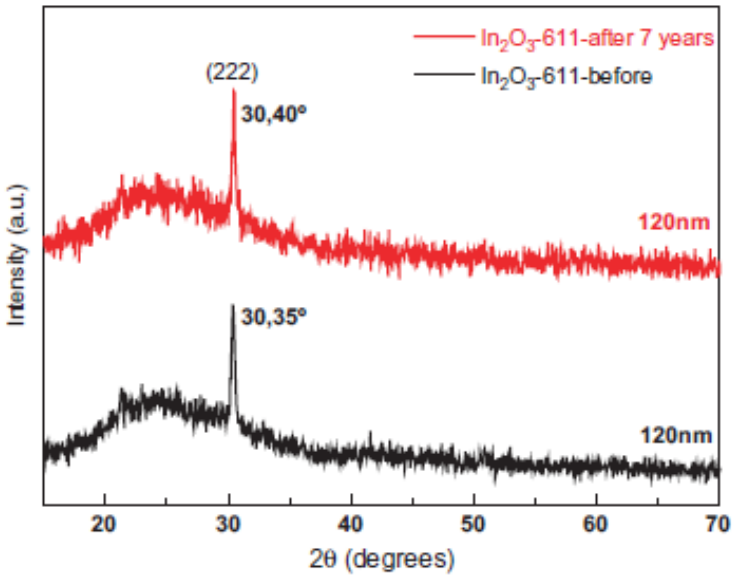

Figure 2.43: XRD patterns of the In_2O_{3-x} (sample 611) evaluated twice, once in its production year and the second 7 years later.

Detailed analysis of the films crystalline size (D) was made by applying Scherrer's formula:

$$D = \frac{0.94\lambda}{B\cos\theta_B},$$

where λ =0,154nm corresponds to K_a edge of Cu, B is the FWHM and θ_B is the angle corresponding to the maximum intensity. In addition, the lattice constant (a_0) was calculated from the equation:

$$\frac{1}{d^2} = \frac{h^2 + k^2 + l^2}{a_0{}^2},$$

where d is the distance between the adjacent planes in the set (hkl). In our case, the above equation was applied for the set of (222) planes due to their dominant intensity. Table 2.1 demonstrates results on the crystalline size (D) and the lattice constant (a) values of the samples

before and after seven years of ageing. It was concluded that both (D) and (a) values remained, within experimental error, insignificantly affected by the ageing process.

Sample	Before		After 7 years ageing	
	D (nm)	a_o (nm)	D (nm)	a_o (nm)
In_2O_{3-x} / 611	26	1.019	30	1.016
In_2O_{3-x} / 612	29	1.017	33	1.016
In_2O_{3-x} / 613	25	1.018	25	1.018

Table 2.1: Crystalline size and lattice constant values of In_2O_{3-x} films before and after seven years.

The retention of the film structural properties was not totally unexpected as any environmentally induced processes such as oxidation, diffusion, etc, would probably influence the films' surface and optical characteristics rather than their bulk properties and thus should reflect mainly on their sensing ability. For this reason the films' morphology and sensing responses were investigated in more detail. Scanning Electron Microscopy (SEM) images of the typical film morphology before and after ageing, shown in figure 2.44, revealed that they retained their initial uniformity and texture to a large extent.

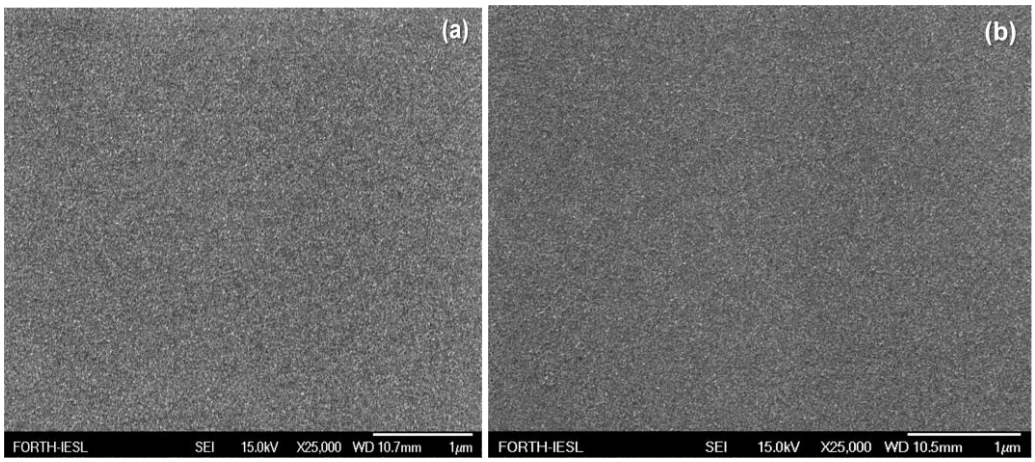

Figure 2.44: Scanning Electron Microscopy images of In_2O_{3-x} sample 611, (a) in 2007 and (b) in 2014.

In as far as the films' optical properties were concerned the initial as-deposited microcrystalline In_2O_{3-x} films were found to be highly

transparent with a transmittance well over 80% a typical characteristic of a wide band-gap metal oxide [2.23]. This characteristic high transmittance value was also retained almost unchanged even after seven years ageing, covering both the visible as well as the near-infrared light regions, as shown in figure 2.45a.

Consequently, the optical energy gap was derived from transmittance measurements. For direct transitions the variation of the absorption coefficient (α) with the photon energy (hv) is given by

$$\alpha = A\left(hv - E_g\right)^{1/2}$$

where E_g is the optical energy gap between the valence and the conduction bands. By plotting (α^2) versus (hv) and extrapolating the linear region of the resulting curve we obtained an energy gap value (E_g) of 3.94±0.01eV before and after 7 years ageing (Fig. 2.45b).

Complementary to the above structural, morphological and optical characteristics, the set of tested films was exposed to an oxidizing environment, in order to re-evaluate their response sensitivities, years after their fabrication date. Figure 2.46 demonstrates three comparative In_2O_{3-x} film responses towards ozone (>5 ppm) following a photo-reduction process (with UV light 254nm, 2 mW/cm^2) of the sample surface. These measurements were carried out at room temperature (twice for each sample, i.e. one for the deposition year and one seven years later) and are presented under the same axis for comparison. Apart from the fully reversible behavior, it can be easily derived that the materials retained their sensing properties in a very satisfactory and reproducible way over time with conductivity variations of 7-8 orders of magnitude being recorded even seven years after film's fabrication date. Such a significant sensing characteristic is promoting In_2O_{3-x} films as effective and durable ageing resistant ozone sensing element materials.

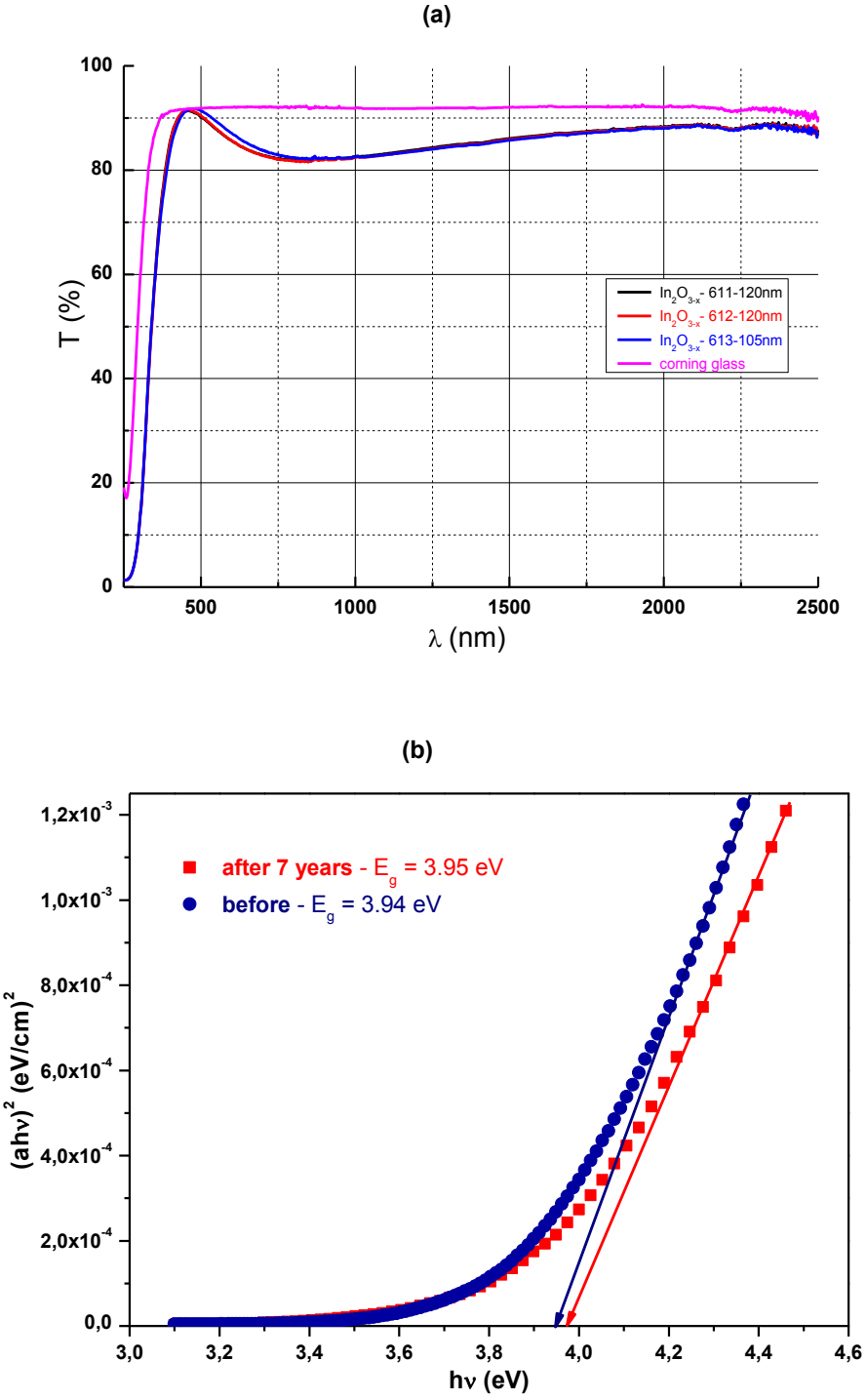

Figure 2.45: (a) Optical transmission spectra of In_2O_{3-x} films after 7 years, (b) optical energy gap before and after 7 years ageing.

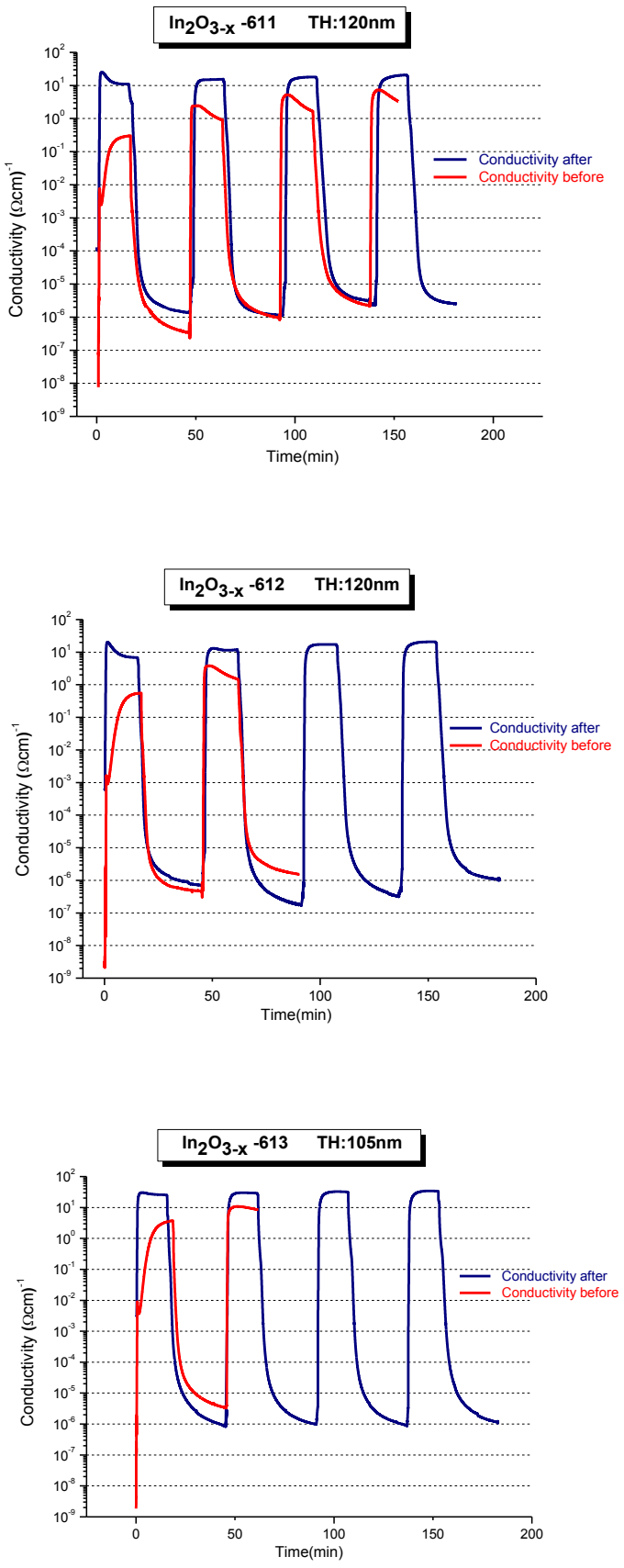

Figure 2.46: Conductivity measurements of In_2O_{3-x} films before and after 7 year ageing.

The above mentioned results reveal the remarkable characteristic of In_2O_{3-x} films to retain unaltered properties like transparency, surface morphology, crystallinity, and optical bandgap, against a significant time span of seven years. In addition, the very strong recorded conductivity changes of up to 8 orders of magnitude on these samples upon photoreduction with UV light and subsequent oxidation in ozone atmosphere denote the material's potential use as an effective and reliable ageing resistant O_3 sensor. Sensing films like those reported here may constitute an excellent solution for low cost, low energy (room temperature) operation in dedicated environmental applications such as clean rooms, operating theatres and other.

2.4 Sensitive layer selection

Regarding ZnO thin films prepared by DC Magnetron Sputtering, they were not able to provide distinct responses towards different ozone concentrations. Instead, all responses, irrespectively of the different ozone levels, were overlapping themselves (Fig. 2.14) thus denoting a major drawback of the subject material in detecting specific accurate ozone concentrations.

On the other hand, while the ZnO films prepared by Aerosol Spray Pyrolysis (ASP) provided ultra high sensitivity towards 16ppb O_3 concentration, the deposition process itself exhibited two intrinsic drawbacks: i) instability during deposition causing variations in the film's deposition rate (Fig. 2.17), ii) high substrate temperature (350°C) with a risk of damaging the delicate SAW structures and devices during deposition.

On the contrary, as far as In_2O_{3-x} films are concerned, once ultra low ozone concentrations of the order of 6ppb were detected within the first minute of exposure and the repeatability as well as the reproducibility of the results was assured, together with the ultimate ageing characteristics of the material, it was decided to adopt In_2O_{3-x} as the active layer on top of surface acoustic wave (SAW) structures and devices to exploit a further enhancement or at least achieving similar sensitivity levels. Such an enhancement may be the result of an induced interaction of the oxidizing/reducing gas molecules with the In_2O_{3-x} selective layer that perturbs the electrical boundary condition at the surface of the SAW device and consequently affects the propagation characteristics, such as the velocity and amplitude of the electro-mechanical waves. In this way changes in the frequency characteristics of the sensor can be correlated with the corresponding gas concentration being targeted.

References

[2.1] C. Xirouchaki, G. Kiriakidis, T.F. Pedersen, H. Fritzsche, "Photoreduction and oxidation of as-deposited microcrystalline indium oxide", *J. Appl. Phys.* 79, 9349 (1996).

[2.2] C. Xirouchaki, K. Moschovis, E. Chatzitheodoridis, G. Kiriakidis, H. Boye, P. Morgen, "Structural and Chemical Characterization of As-Deposited Microcrystalline Indium Oxide Films Prepared by dc Reactive Magnetron Sputtering", *Journal of Electronic Materials*. 28, No1 (1999) 26–34.

[2.3] M. Bender, E. Gagaoudakis, E. Douloufakis, E. Natsakou, N. Katsarakis, V. Cimalla, G. Kiriakidis, E. Fortunato, P. Nunes A. Marques, R. Martins, "Production and characterization of zinc oxide thin films for room temperature ozone sensing", *Thin Solid Films* 418 (2002) 45–50.

[2.4] N. Katsarakis, M. Bender, V. Cimalla, E. Gagaoudakis, G. Kiriakidis, "Ozone sensing properties of DC-sputtered, *c*-axis oriented ZnO films at room temperature", *Sensors and Actuators B* 96 (2003) 76–81.

[2.5] M. Bender, N. Katsarakis, E. Gagaoudakis, E. Hourdakis, E. Douloufakis, V. Cimalla, G. Kiriakidis, "Dependence of the photoreduction and oxidation behavior of Indium oxide films on substrate temperature and film thickness", *J. Appl. Phys.* 90 (2001) 5382.

[2.6] A. Roth, J.B. Webb, D.F. Williams, "Band-gap narrowing in heavily defect-doped ZnO", *Phys. Rev. B* 25 (1982) 7836.

[2.7] A. Asadov, W. Gao, Z.Li, J.Lee, M. Hodgson, "Correlation between structural and electrical properties of ZnO thin films", *Thin Solid Films* 476 (2005) 201.

[2.8] Nicolae Barsan, Udo Weimar, "Conduction Model of Metal Oxide Gas Sensors", *Journal of Electroceramics* 7 (2001), 143.

[2.9] I. Kortidis, K. Moschovis, F.A. Mahmoud, G. Kiriakidis, "Structural analysis of aerosol spray pyrolysis ZnO films exhibiting ultra low ozone detection limits at room temperature", *Thin Solid Films* 518 (2009) 1208–1213.

[2.10] Perednis D, Gauckler LJ. "Thin Film Deposition Using Spray Pyrolysis", *Journal of Electroceramics* 14 (2005), 103-111.

[2.11] J.L van Heerden, R Swanepoel, "XRD analysis of ZnO thin films prepared by spray pyrolysis", *Thin Solid Films* 299*,* (1977)*,* 72-*77.*

[2.12] S.A. Studenikin, N. Golego, M. Cocivera "Optical and electrical properties of undoped ZnO films grown by spray pyrolysis of zinc nitrate solution" *J Appl Phys*. 83, 2104 (1998).

[2.13] P. Singh, A. Kumar, Deepak, D. Kaur "Growth and characterization of ZnO nanocrystalline thin films and nanopowder via low-cost ultrasonic spray pyrolysis" *Journal of Crystal Growth* 306, (2007), 303-310.

[2.14] Forest Shih-Sen Chien, Chang-Ren Wang, Yu-Lin Chan, Hsiao-Lan Lin, Min-Hung Chen, Ren-Jang Wu, "Fast-response ozone sensor with ZnO nanorods grown by chemical vapor deposition", *Sensors and Actuators B* 144, (2010), 120-125.

[2.15] G. Kiriakidis, K.Moschovis, I. Kortidis, R. Skarvelakis, "Highly Sensitive InOx Ozone Sensing Films on Flexible Substrates" Hindawi publishing corporation *Journal of Sensors,* vol. 2009, Article ID 727893, 5 pages doi:10.1155/2009/727893.

[2.16] Edelman, F., Cytermann, C., Brener, R., Eizenberg, M., Khait, Yu.L., Weil, R. and Beyer, W. "Crystallization in fluorinated and hydrogenated amorphous silicon thin films", *J. Appl. Phys.* 75, (1995), p.7875.

[2.17] R. Martins, E. Fortunato, P. Nunes, I. Ferreira, A. Marques, M. Bender, N. Katsarakis, V. Cimalla, G. Kiriakidis, "Zinc oxide as an ozone sensor", *J. Appl. Phys.* 96 (2004), 1398.

[2.18] P.K. Kofstad "Nonstoichiometry, diffusion and electrical conductivity in binary metal oxides (Science & Technology of Materials)", *John Wiley & Sons Inc (April 5, 1972).*

[2.19] G. Kiriakidis, M. Suchea, S. Christoulakis, P. Horvath, T. Kitsopoulos , J. Stoemenos, "Structural characterization of ZnO thin films deposited by dc magnetron sputtering", *Thin Solid Films* 515 (2007) 8577–8581.

[2.20] G. Kiriakidis, M. Suchea, S. Christoulakis, N. Katsarakis, "High performance gas sensing materials based on nanostructured metal oxide films", *Rev.Adv.Mater.Sci*. 10 (2005), 215-223.

[2.21] G. Kiriakidis, K. Moschovis, and S. B. Sadale, "Systems and set-ups for effective sensing response applications" *Sensors for Environment, Health and Security: Advanced Materials and Technologies*, M.-I. Baraton, Ed., vol. 24, pp. 159–178, Springer, New York, NY, USA, 2009.

[2.22] S.J. Ippolito, S. Kandasamy, K. Kalantar-zadeh, et al., "Highly sensitive layered ZnO/LiNbO3 SAWdevice with InO*x* selective layer for NO_2 and H_2 gas sensing" *Sensors and Actuators B*, vol. 111-112 (2005), 207–212.

[2.23] J.E. Medvedeva, A.J. Freeman, "Combining high conductivity with complete optical transparency: A band structure approach", *Europhys. Lett.* 69, 583 (2005).

3. SAW Devices

As far as the second approach is concerned and further to the above mentioned experiments, DC sputtered In_2O_{3-x} thin films, with thickness of the order of 100nm, were deposited onto conventional delay line structures as well as onto commercially available SAW filters whose operating frequency varied from 139MHz-930MHz. Before describing thoroughly the experimental procedure that was followed, a brief introduction into SAW filter theory is presented below.

3.1 Basic operational principles

In general, a surface acoustic wave is a type of mechanical wave motion which travels along the surface of a solid material. The wave was discovered by Lord Rayleigh in 1887 [3.1], and is often named after him. Rayleigh showed that SAWs could explain one component of the seismic signal due to an earthquake, a phenomenon not previously understood. These days, acoustic waves are often used in electronic devices. At first sight it seems odd to use an acoustic wave for an electronic application, but acoustic waves have some particular properties that make them very attractive for specialized purposes. For example many wristwatches have a quartz crystal used for accurate frequency generation, and this is an acoustic resonator though it uses bulk acoustic waves rather than surface waves.

As far as gas sensors are concerned, the first report of a SAW device employed for gas sensing was in 1979 by Wohltjen and Dessy [3.2]. In their paper, they investigated the operation of a 2-port delay line SAW device utilizing a quartz and $LiNbO_3$ piezoelectric substrate. Following this work, reports emerged in literature on a variety of SAW-based sensors for monitoring gases such as: sulfur dioxide (SO_2) [3.3], hydrogen (H_2) [3.4], [3.5], humidity (H_2O), carbon dioxide (CO_2) [3.6], hydrogen sulfide (H_2S) [3.7], nitrogen oxide (NO) [3.8], [3.9], organophosphorous compounds [3.10], as well as many others. SAW-based vapor sensors have also been extensively investigated [3.11].

A basic SAW device, shown in figure 3.1, consists of two interdigital transducers (IDTs) on a piezoelectric substrate such as quartz. The area between the input IDT and output IDT is called the delay line, because the wave takes some time to travel between the transducers-typically 1μs for 3mm of path length which is very compact compared to EM waves that, in free space, need 300m of path for 1μs delay. The fact that the acoustic waves travel that slowly and large delays are obtainable, is their basic advantage.

The IDTs consist of interleaved metal electrodes which are used to launch and receive the waves, so that an electrical signal is converted to an acoustic wave and then back to an electrical signal. The IDT geometry is capable of almost endless variation, leading to wide variety of devices. Starting around 1970, SAW devices were developed for pulse compression radar, oscillators, and band-pass filters for domestic TV and professional radio. In the 1980s the rise of mobile radio, particularly for cellular telephones, caused a dramatic increase in demand for filters [3.12]. New high-performance SAW filters emerged and vast numbers, around 3 billion annually, are now produced.

The metal film used to make the IDTs should be thick enough, to offer low electrical resistance and thin enough, to avoid excessive mechanical load to the acoustic wave. Typical materials for IDTs are aluminium or gold with nominal thickness around 100nm.

The teeth of the comb electrodes are arranged with a certain pitch between them, and a surface wave is excited most strongly when its wavelength λ is the same as the pitch of the electrode teeth. The equation $f_0 = v/\lambda$ describes the relation between the center frequency (f_0) and the propagation velocity (v) of a surface wave.

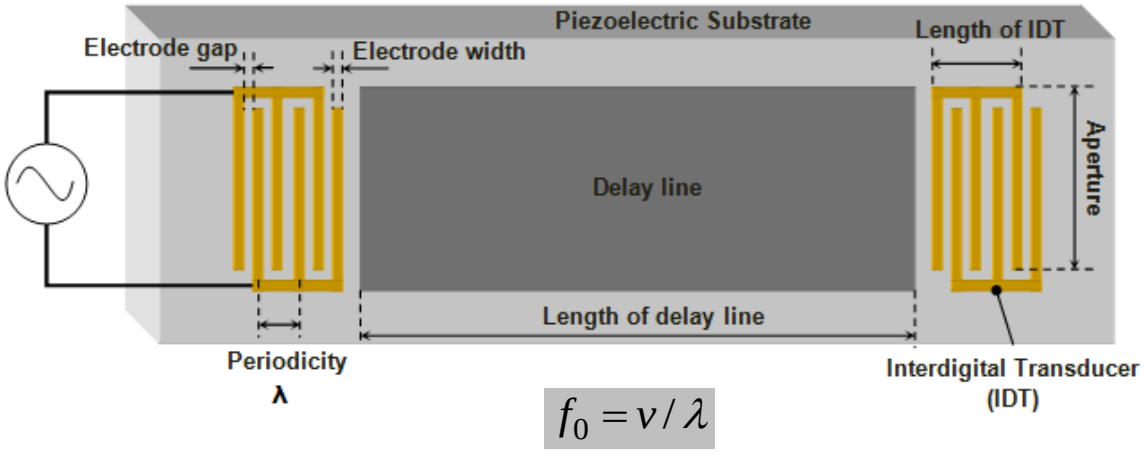

Figure 3.1: Basic SAW device setup (top view).

In the simplest case (an isotropic material), the atoms move in the plane which includes the surface normal and the propagation direction. Figure 3.2 shows a SAW travelling along the plane surface of a solid material [3.12]. As the wave passes, each atom of the material traces out an elliptical path, repeating the path of each cycle of the wave motion. The atoms move by smaller amounts as one looks further into the depth, away from the surface. Thus the wave is guided along the surface with its amplitude decaying into the depth. In order for the wave to behave as a true surface wave, the substrate needs to be at least a few wavelengths thick, so that the wave amplitude is negligible at the lower surface. Practical substrates satisfy this need easily and these usually have a thickness of 0.5 to 1.0mm, chosen to give adequate strength to tolerate stresses involved in fabrication and operation.

The device shown in figure 3.1 can be regarded as a basic bandpass filter. The reason is that the individual sources (electrode gaps) in the input IDT generate waves with alternating signs, and they add up in phase if the SAW wavelength (λ) equals the transducer pitch. This occurs at the "centre frequency". If the frequency is changed then the waves generated by the sources are not quite in phase, and the total amplitude decreases progressively as the frequency is changed. Hence the device has a bandpass characteristic, with the strongest response at

the centre frequency. The bandwidth is approximately $1/\mathrm{T}$ where T is the transducer length in time units (=physical length÷SAW velocity).

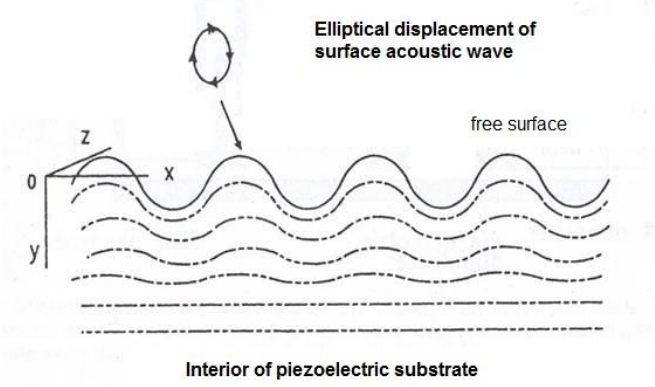

Figure 3.2: Basic surface acoustic wave propagation mode.

Mathematically wise, when an array of fingers is excited as occurs with an IDT the wave potential for a rightward propagating wave ϕ^{+}, evaluated at a certain position z, is a vector sum of the contributions from each finger:

$$\varphi^{+}(z) = \mu_s \sum_{n=0}^{N_f - 1} V_n e^{jk(z - z_n)} ,$$

where z_n is the position of the n^{th} finger excited with voltage V_n and N_f is the total number of fingers.

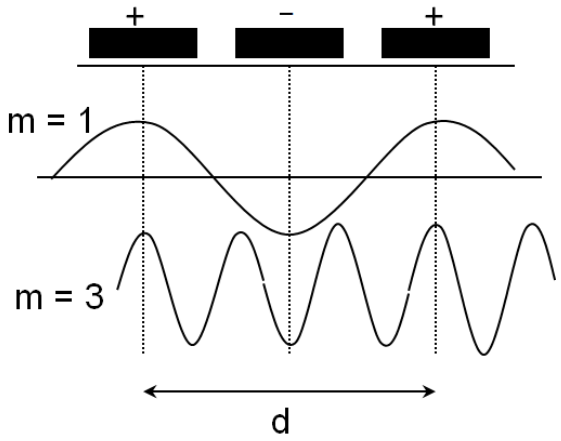

Figure 3.3: Relationship between IDT's periodicity and coherently excited waves.

If N_f identical finger pairs are spaced periodically with period d and excited with alternating voltages $V_n = (-1)^n V_0$, then the above equation becomes:

$$\varphi^+(0) = \mu_s V_0 \sum_{n=0}^{N_f-1} (-1)^n e^{-jnkd/2},$$

where the term $nd/2$, in the exponential factor, denotes the position of each finger starting with z_0=0, $n=0$ for the first finger, for the second finger $n=1$, $z_1 = d/2$, for the third $n=2$, $z_2 = d$, and so forth.

Now, if $\frac{kd}{2} = m\pi$, where m is an odd integer, then:

$$\varphi^+(0) = \mu_s V_0 (-1)^0 e^0 + \mu_s V_0 (-1)^1 [\cos m\pi - i \sin m\pi] + \mu_s V_0 (-1)^2 [\cos 2m\pi - i \sin 2m\pi]$$
$$+ \mu_s V_0 (-1)^3 [\cos 3m\pi - i \sin 3m\pi] + \mu_s V_0 (-1)^4 [\cos 4m\pi - i \sin 4m\pi] + \ldots\ldots\ldots\ldots \Rightarrow$$
$$\Rightarrow \varphi^+(0) = \mu_s V_0 + \mu_s V_0 + \mu_s V_0 + \mu_s V_0 + \mu_s V_0 + \ldots\ldots\ldots\ldots\ldots$$

Furthermore, $\frac{kd}{2} = m\pi \Rightarrow \frac{2\pi}{\lambda} = \frac{2m\pi}{d} \Rightarrow d = m\lambda$, ($m$: odd integer)

For $m=1$, $d = \lambda \Rightarrow f_0$
$m=3$, $d = 3\lambda \Rightarrow 3f_0$
$m=5$, $d = 5\lambda \Rightarrow 5f_0$
…….
……and so forth

$\Rightarrow$ for coherent addition

Therefore the IDT excites odd harmonics at odd multiples of the synchronous frequency (f_0), i.e. $f_m = mf_0$ (Fig. 3.3).

Moving away from the synchronous frequency, the addition of components from individual fingers becomes incoherent giving rise to a frequency response of a sinc function:

$$\left|\phi^+(f)\right| = \left|\frac{\sin(X)}{X}\right|$$

in which $X = \frac{N_p \pi (f - f_0)}{f_0}$, $N_p = N_f / 2$ is the number of IDT periods and f_0 is the transducer's synchronous frequency.

A typical SAW bandpass filter characteristic is depicted in figure 3.4, based on own measurements on a typical commercial SAW filter operating at 171MHz nominal frequency.

The upper graph depicts the magnitude while the lower one depicts the phase of the transmitted signal as a function of the excitation frequency. The four points denoted by filled circles, indicate the four frequencies oscillating with less insertion loss (less than 20db) and a round-trip phase shift of zero.

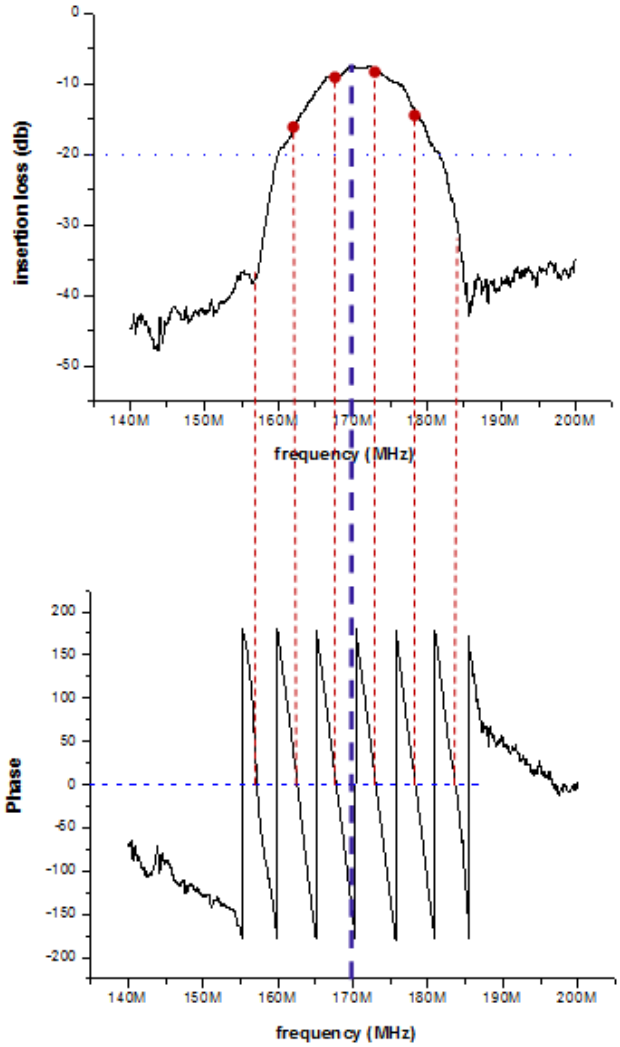

Figure 3.4: Frequency response of a SAW bandpass filter operating at a NF 171MHz showing both magnitude (upper curve) and phase (lower curve).

SAW devices are normally fabricated using photolithography, a technique that gives accurate control of the electrode geometry. This is one reason for the success of the technology, another being that the crystal substrates have very reproducible properties, so that devices with very predictable performance can be produced. The minimum linewidth is in the region of the light wavelength. In production, the narrowest linewidth obtainable is around 0.3μm with 365nm UV photolithography typically used in the industry. This corresponds to $\lambda/4$ and for a typical velocity of 3500m/s it gives a maximum frequency of about 3GHz. Narrower linewidths are obtainable using special techniques, for example electron beam exposure, but these are not applicable to large-scale manufacturing. The effectiveness of these devices is also due to the fact that the wave propagates in an almost ideal manner, with very little attenuation, dispersion or diffraction. Additionally, as already stated, a particular advantage is the slow acoustic velocity that enables long delays to be obtainable in a small space.

However, their performance is constrained by the properties of the substrate material. For SAW devices, the substrate is usually one of a number of standard materials already known to have suitable SAW properties. One property of interest is the piezoelectric coupling constant K^2, which determines the strength of coupling between electrical and mechanical fields. In general, a larger K^2 value enables lower insertion loss to be obtained, or wider bandwidth for the same loss. Another major property is the temperature coefficient of delay (TCD), which specifies how the delay varies with temperature (this involves velocity and dimensional changes). This also gives the temperature coefficient for the centre frequency of a filter. Some data for common materials is given in table 3.1.

Material	SAW velocity m/s	K^2	TCD (ppm/°C)
Quartz, 34° Y-X	3152	0.13 %	0
$LiNbO_3$, 128° Y-X	3978	5.40 %	75
$LiTaO_3$, X-112° Y	3302	0.84 %	18
$LiTaO_3$, 42° Y-X	4214	5.00 %	23

Table 3.1: Materials basic characteristics.

Quartz has low piezoelectric coupling, but particular substrate orientations give good temperature stability. The TCD is zero at a particular temperature, around 20°C. Lithium niobate exhibits the opposite behavior with strong coupling but rather bad temperature stability. Lithium tantalate is intermediate in both respects.

Finally, there are many different types of SAW filters, all consisting of a metal film etched to a specified geometry using a photolithography process similar to that used for semiconductor processing. Another factor is that a compact device, with length e.g. 1cm, can have many SAW wavelengths inside it and hence many degrees of freedom.

3.2 Experimental process and results

Regarding SAW devices for gas sensing applications two major approaches have been employed. In the first case layered SAW devices (delay line structures) were fabricated on XY-$LiNbO_3$ wafers in the framework of a bilateral collaboration between FORTH and RMIT-Melbourne. DC Magnetron sputtering was used to deposit In_2O_{3-x} as active layer on top. Two sensors were developed with 20nm and 100nm In_2O_{3-x} thin films respectively at SAW operating frequencies of 138.2MHz and 139.6MHz. The reason for selecting these active layer thicknesses lies on previous work [3.13] where it has been observed that the films with thickness of 100nm or less exhibited higher sensitivities to ozone compared to thicker ones. The above mentioned sensors were examined

towards oxidizing gases such as NO_2 and O_3 as well as towards reducing gases such as H_2.

In a second approach again DC sputtered In_2O_{3-x} films with thickness of the order of 100nm were deposited onto commercially available SAW filters operating in a wide range of central frequencies ranging from 139MHz-930MHz. All depositions were carried out under identical conditions and the only parameter changing was the filter's central operating frequency. The filter responses were tested over a range of operating temperatures and towards oxidizing and reducing gases such as O_3, NO_2 and H_2 with varying concentrations.

Initial measurements were carried out in RMIT-Melbourne and at a later stage in FORTH's facilities. To achieve this, a specially designed cell capable of hosting SAW filters onto temperature controlled substrates was developed at FORTH's machinery shop (Fig. 3.5).

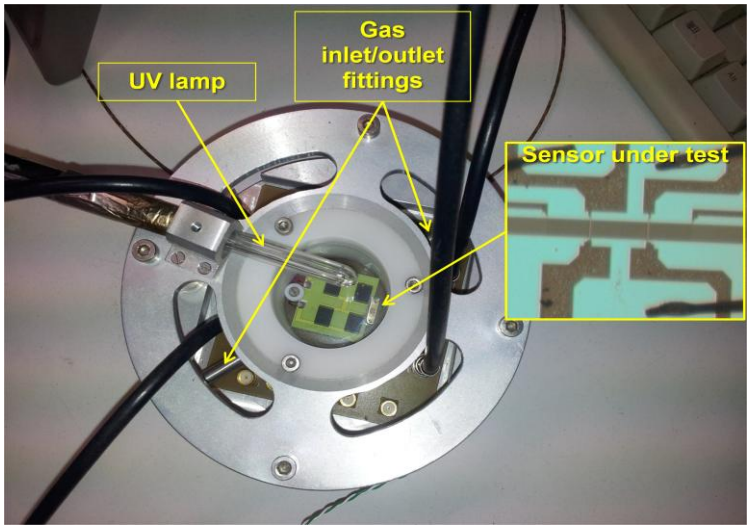

Figure 3.5: Home-made cell for hosting SAW filter sensitivity measurements.

The cell incorporated a UV pencil style lamp fitting together with a quartz glass located directly opposite the filter structure and it was open to gas flow through inlet and outlet fittings while a labview based program was developed to facilitate automatic computer calculations.

At a later stage, the new cell was incorporated into the already developed homemade experimental setup used for conductivity-based

photoreduction and oxidation measurements depicted in figure 2.10. The schematic of the new setup emerged is shown in figure 3.6.

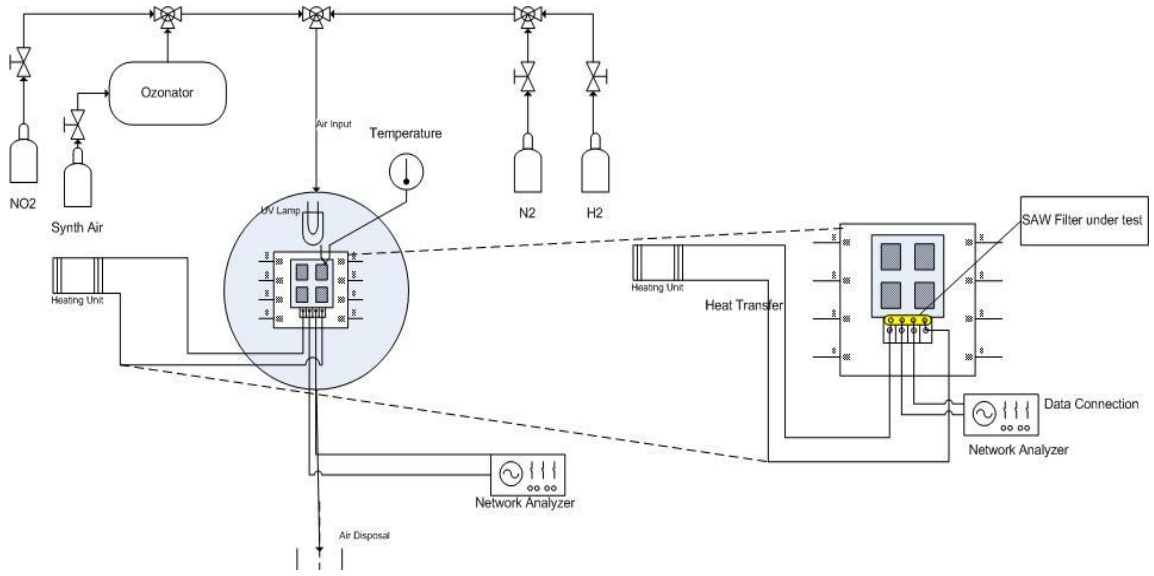

Figure 3.6: Schematic of SAW filter sensitivity measurement setup.

3.2.1 Results on low-frequency delay line SAW transducers

Figure 3.7 demonstrates a cross-section diagram of a layered SAW device fabricated in the framework of a bilateral project between the FORTH and RMIT research groups [3.14]. Two SAW devices were fabricated on XY $LiNbO_3$ wafers, using an Al metallisation layer (250nm) deposited onto a Cr adhesion layer (30nm) by electron beam evaporation. Electrodes with a periodicity of 24μm were patterned using a wet-etch process to create a 2-port delay line with 64 finger pairs in each port. A centre-to-centre distance of 85 wavelengths with an aperture width of 1.25mm was used. ZnO piezoelectric guiding layers were deposited by RF magnetron sputtering using a 99.99% pure ZnO target. DC Magnetron Sputtering was used to deposit In_2O_{3-x}. Two sensors were developed with 20nm and 100nm In_2O_{3-x} thin films, respectively.

The SAW devices were mounted on a micro-heater and enclosed in a Teflon based gas chamber, approximately 30ml in volume. The micro-heater was controlled by a regulated DC power supply, which provided different operating temperatures. Using a computerized multi-channel

gas calibration system, each sensor was exposed to a known sequence of NO_2 and H_2 gas pulses over a range of operating temperatures between room temperature and 185°C.

- **Substrate: XY**
- **$LiNbO_3$**
- **ZnO guiding layer: 1 μm**
- **Al electrodes: 250 nm**
- **Periodicity d: 24 μm**
- **Finger pairs number, N_p: 64**
- **L: 85λ**
- **W: 1.25 mm**

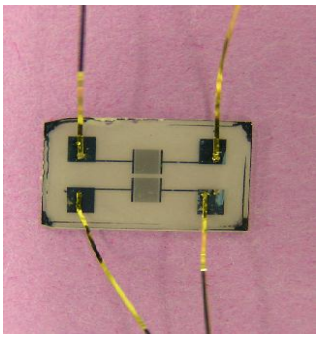

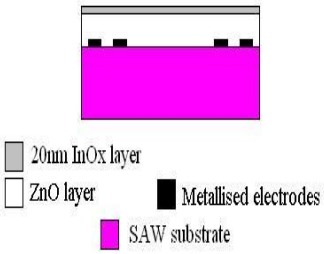

Figure 3.7: SAW sensor structure.

The exposed NO_2 and H_2 gas concentration range was varying from 510ppb to 8.5ppm and from 0.06 to 1.0% in synthetic air, respectively. The synthetic air composed of 20% oxygen balanced in nitrogen. A constant flow rate of 0.2lit/min and certified gas bottles balanced in synthetic air were used. At each operating temperature, the baseline gas was maintained for a period of 90min to allow the device to stabilize. Then, the device was exposed to the different concentration sequences of NO_2 and H_2 for several hours.

Both the 20 and 100nm In_2O_{3-x} layer SAW devices were tested separately, however all tests were carried out under the same conditions. The SAW devices were used as positive feedback elements in a closed-loop circuit along with an amplifier to form an oscillator. Thus, the frequency of the system could then correlate to the corresponding target gas concentration. The operating frequencies for the 20nm and 100nm sensor at room temperature were 138.2MHz and 139.6MHz, respectively.

Figure 3.8 illustrates the response of a 20nm (top) and 100nm (bottom) In_2O_{3-x} layered SAW sensor towards successive NO_2 pulses of 510ppb, 1.063ppm, 2.125ppm, 4.2ppm, 8.5ppm and 1.063ppm in synthetic air at 168°C. It can be seen that the sensor with 20 nm of In_2O_{3-x} largely outperforms the 100nm sensor. The 20nm In_2O_{3-x} sensor produced a 73.562kHz frequency shift for 510ppb of NO_2 at an operating temperature of 168°C. It was observed that, at higher concentrations, the sensor response saturated.

Unlike NO_2, H_2, as a reducing gas, increases the conductivity of In_2O_{3-x}, therefore the acoustic wave velocity decreases and this is the reason for the observed decrease in the oscillation frequency in the presence of H_2. The H_2 pulse sequence consisted of 0.06%, 0.125%, 0.25%, 0.5%, 1% and 0.125% H_2 in synthetic air (Fig. 3.9). The last cycle was carried out for repeatability reasons. Once again both sensors were tested at an operating temperature of 168°C and the sensor with 20nm In_2O_{3-x} on top largely outperformed once more the 100nm sensor. Responses towards H_2 gas concentrations of 600ppm to 10000ppm were in the range of 78.5kHz to 319.4kHz. Compared to the NO_2 exposure situation, the sensor response towards H_2 did not appear to saturate, and exhibited a large dynamic response range towards H_2.

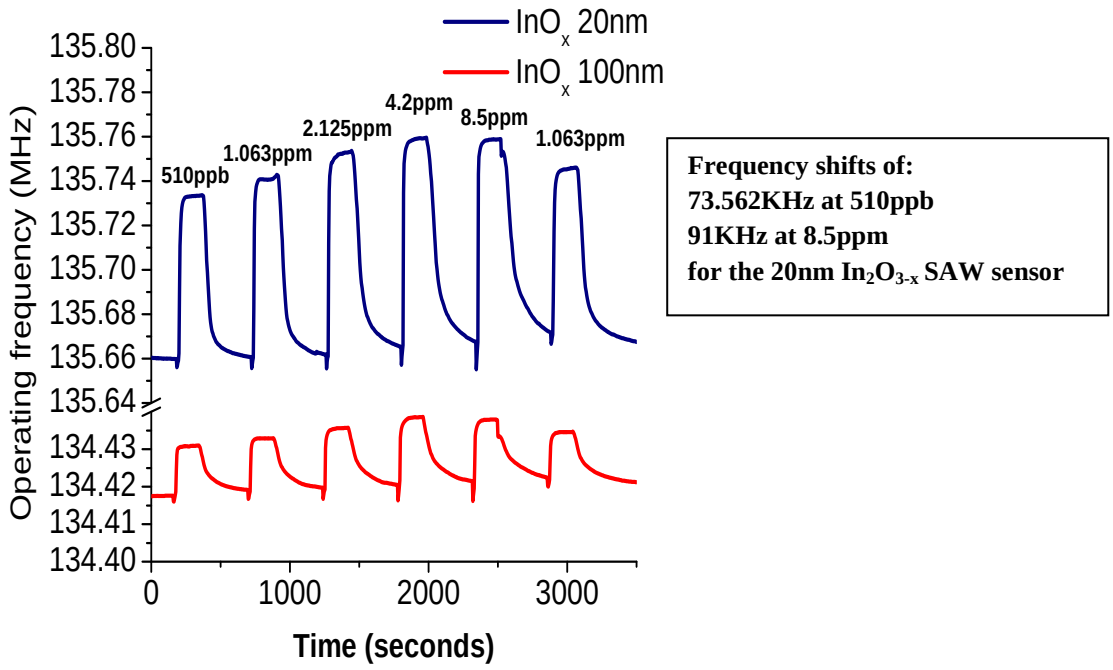

Figure 3.8: Response of 20nm (top) and 100nm (bottom) In_2O_{3-x} layered SAW sensor towards a sequence of NO_2 pulses in synthetic air at 168°C.

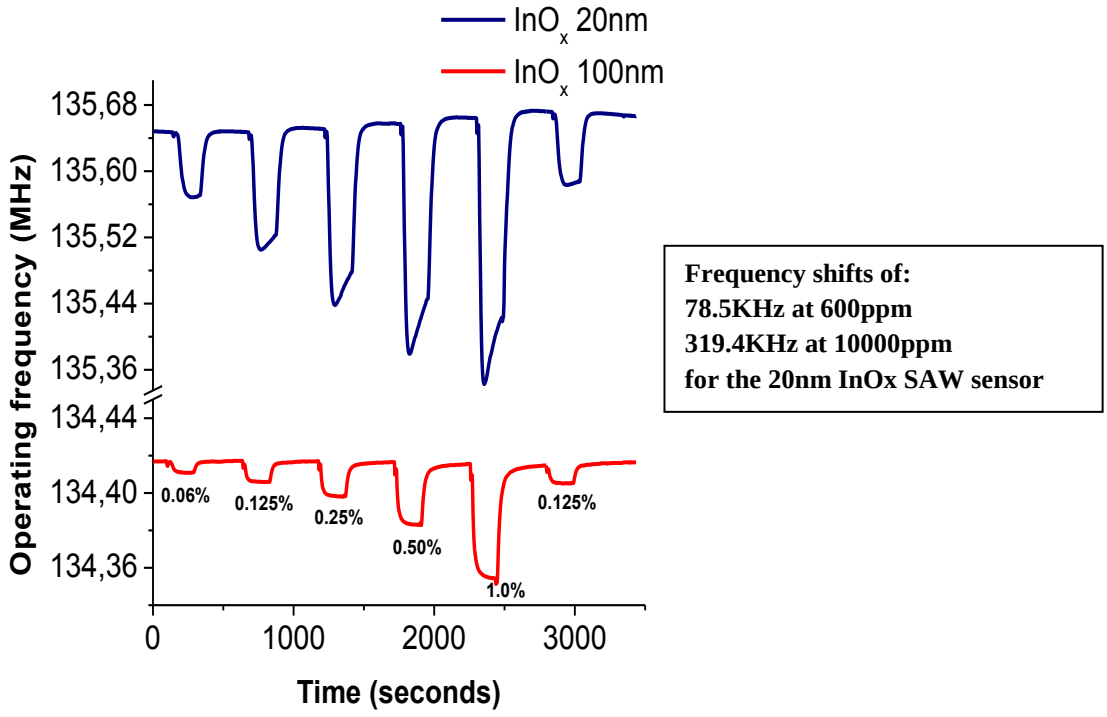

Figure 3.9: Response of 20nm (top) and 100nm (bottom) In_2O_{3-x} layered SAW sensor towards a sequence of H_2 pulses in synthetic air, at 168°C.

Figure 3.10 illustrates the response of the 100nm (top) and 20nm (bottom) In_2O_{3-x} layered SAW sensor towards a sequence of O_3 pulses in synthetic air. This time the 100nm thick In_2O_{3-x} sensor exhibited a higher sensitivity than its 20nm counterpart, with fast response and recovery times.

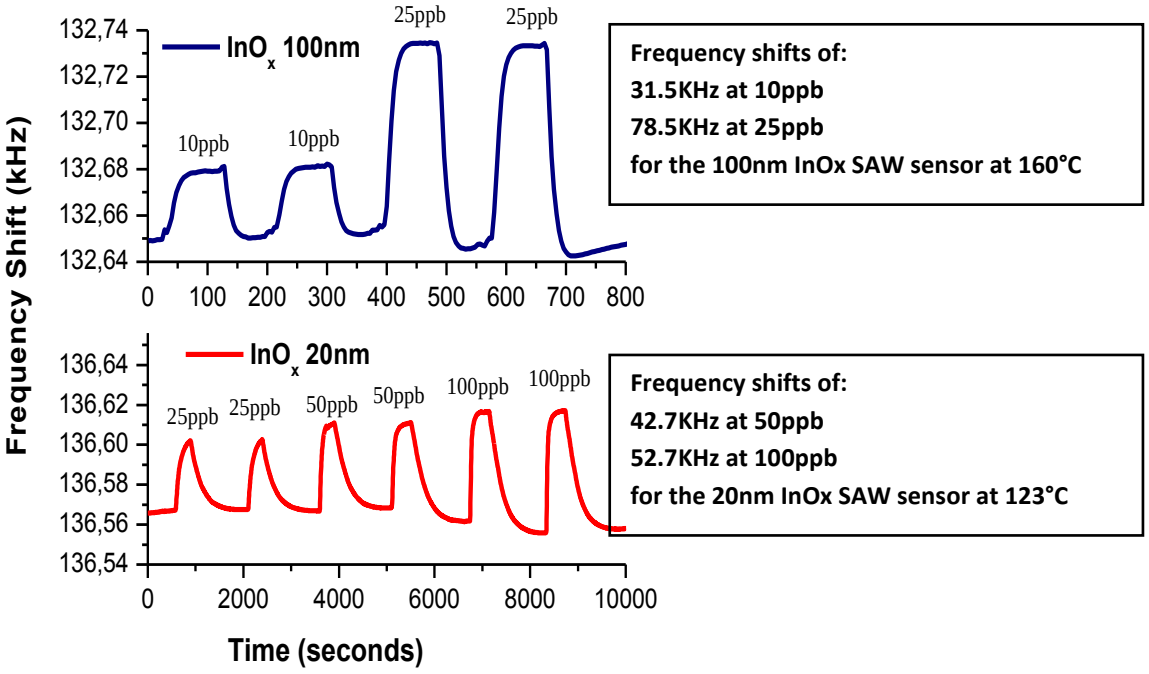

Figure 3.10: Response of 100nm (top) and 20nm (bottom) In_2O_{3-x} layered SAW sensors towards a sequence of O_3 pulses in synthetic air.

At an operating temperature ranging from 150°C to 175°C, a frequency shift of 31.5kHz for 10ppb and 78.5kHz for 25ppb was observed for the 100nm sensor when using an exposure and recovery time of 90 seconds (Fig. 3.11). For the 20nm sensor a 5-minute exposure and 20-minute recovery time was used. At an operating temperature of 123°C a frequency shift of 42.7kHz for 50ppb and 52.7kHz for 100ppb of ozone were recorded (Fig.3.12).

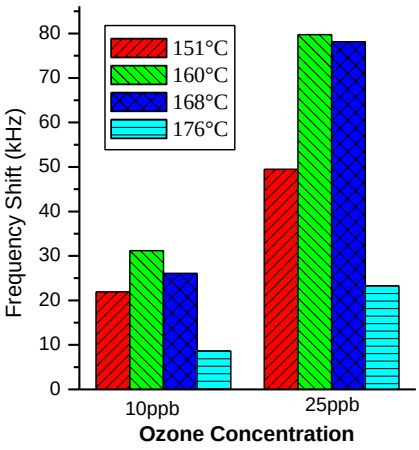

Figure 3.11: Frequency shifts of 100nm In_2O_{3-x} sensor at various temperatures.

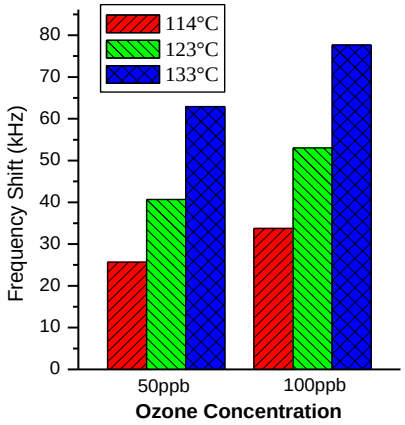

Figure 3.12: Frequency shifts of 20nm In_2O_{3-x} sensor at various temperatures.

Consequently, it was proved that the above layered SAW gas sensors are capable of detecting ultra low ozone concentrations of the order of 10ppb, a value which is comparable with that obtained by the simple conductivity-based method shown earlier.

3.2.2 Results on the use of SAW filters

On a second approach, a set of commercially available SAW filters were used as the base for the investigation of the material (In_2O_{3-x}) sensing characteristics.

In order to deposit the active In_2O_{3-x} layer on top of the SAW filters, the top cap of the commercially available device was carefully removed without damaging the inner sensitive interdigital transducer structure as shown in figure 3.13.

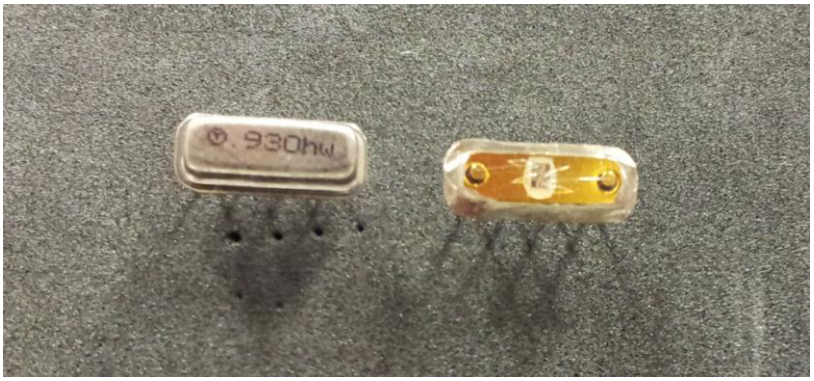

Figure 3.13: 930MHz commercial filter (left) with top cap removed (right).

Furthermore, five specially designed substrate holders were manufactured at FORTH's workshop, capable of hosting the SAW filters during depositions (Fig. 3.14).

Figure 3.14: Substrate holders for SAW filters.

Figures 3.15 and 3.16 reveal typical interdigitated transducer structures and frequency responses of a 280MHz and a 930MHz SAW filters respectively.

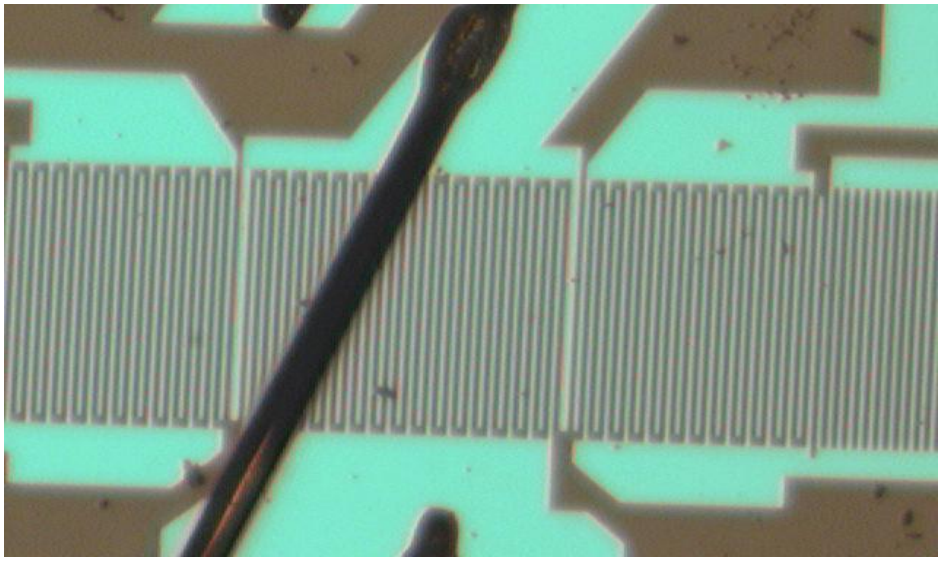

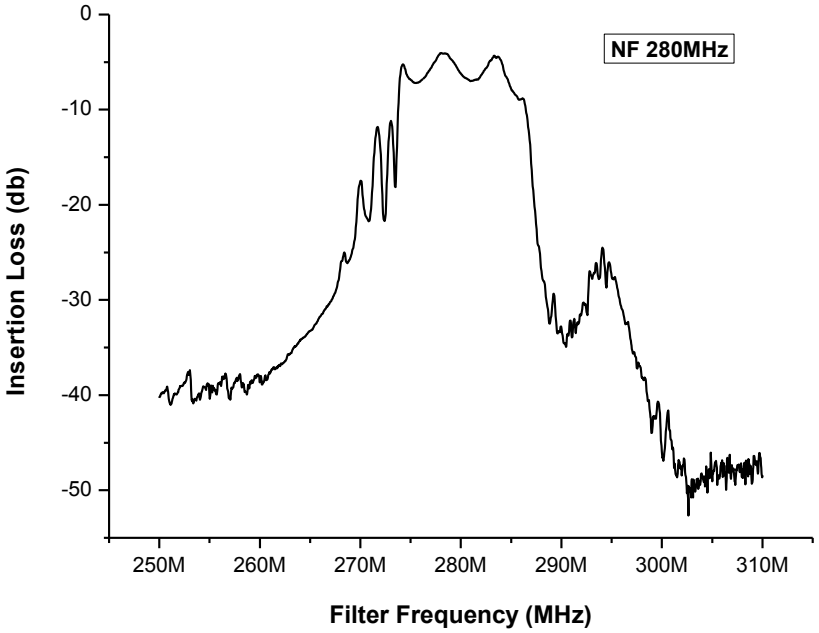

Figure 3.15: Typical interdigital transducer structure and frequency response of a commercial 280MHz SAW filter.

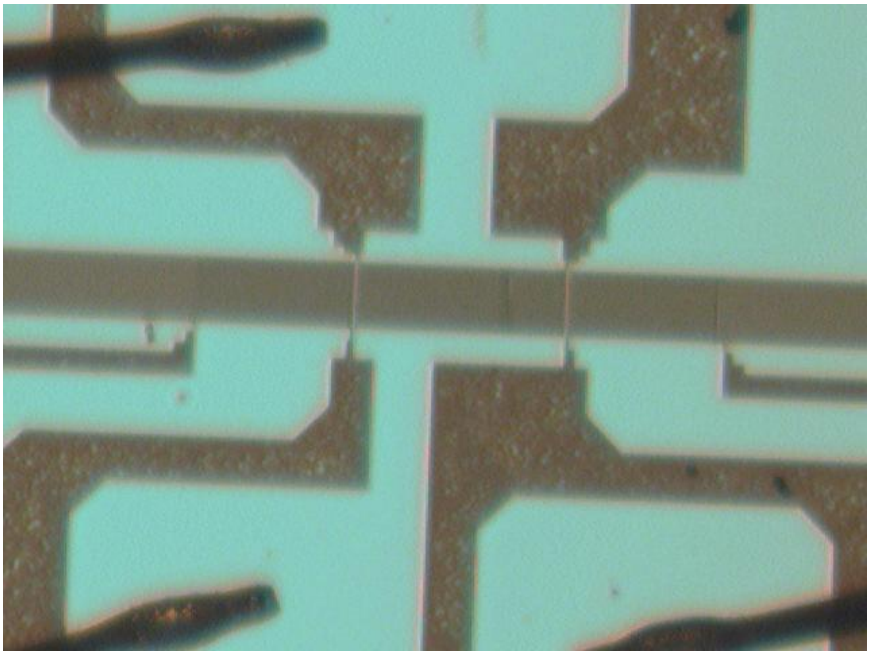

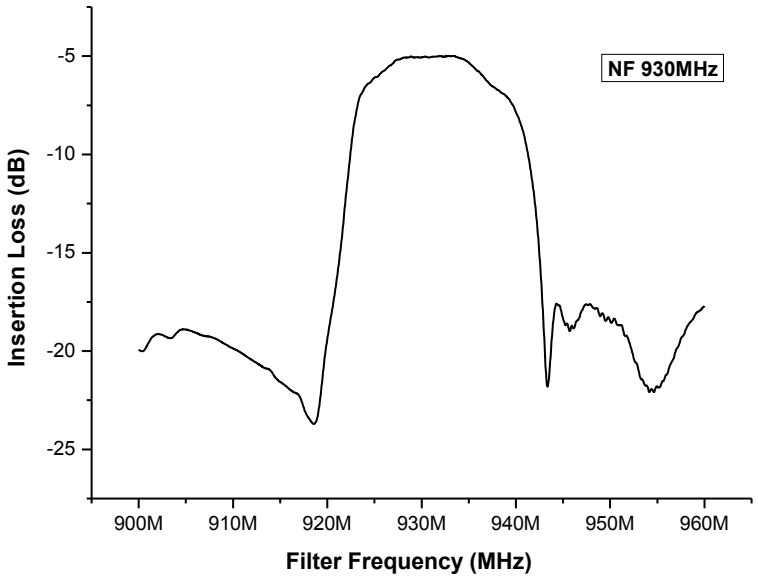

Figure 3.16: Typical interdigital transducer structure and frequency response of a commercial 930MHz SAW filter.

Utilising these SAW filters, an attempt was made to investigate the correlation and the degree of contribution of the two main parameters, namely the "mass loading" and the "acoustoelectric response" upon the operation frequency of the investigated filters operating up to 1GHz.

3.2.2.1 Verification of the "mass loading" effect on commercial SAW transducers

SAW mass loading is the most utilized and simplest interaction in SAW sensor applications. The recorded responses due to mass loading are due to changes in the wave velocity (or, equivalently oscillation frequency) by the addition or removal of mass at the surface of the sensor. Surface mass changes can result from sorptive interactions (i.e. adsorption or absorption) or chemical reactions between analyte and coating and can be used for sensing applications in both liquid and gas phases.

Motion of a wave in a surface layer that is sufficiently thin or rigid that moves synchronously with the wave causes an increase in the kinetic energy density U_k without dissipating any wave energy. This is expected to change the wave propagating velocity without affecting attenuation due to the thin surface layer. The change in average kinetic energy per area of surface is expressed as [3.15]:

$$\Delta U_k = \frac{\rho_s}{4}\left(v_{x0}{}^2 + v_{y0}{}^2 + v_{z0}{}^2\right) \qquad (3)$$

where v_{x0}, v_{y0}, v_{z0} are the SAW particle velocities at the surface and ρ_s is the surface mass density.

An increase in kinetic energy density results in a decrease in wave velocity, assuming that the power density P is constant i.e. lossless medium.

$$P = Uv \Rightarrow \frac{\Delta U}{\Delta v} = \frac{\Delta(P/v)}{\Delta v} = -\frac{P}{v^2} = -\frac{Uv}{v_2} = -\frac{U}{v} \Rightarrow$$

$$\frac{\Delta v}{v_0} = -\frac{\Delta U}{U_0} \text{ (lossless medium)……(4)}$$

where v_0 and U_0 denote unperturbed propagation velocity and energy density respectively.

Equation (4) denotes that any fractional change in wave velocity is equal to the negative of the fractional change in wave energy density, meaning that changes of the medium that affect the wave energy density will cause changes of the wave velocity.

Combining equations 3 & 4 results in a fractional velocity shift varying with operating frequency f_0 and decreasing linearly with the surface mass density as depicted in figure 3.16.

$$\frac{\Delta v}{v_0} = -\frac{\omega v_0 \rho_s}{4}\left(\frac{{v_{x0}}^2}{\omega P} + \frac{{v_{y0}}^2}{\omega P} + \frac{{v_{z0}}^2}{\omega P}\right) \Rightarrow$$

$$\Rightarrow \frac{\Delta v}{v_0} = -c_m f_0 p_s \text{.....(5)}$$

where $c_m = \frac{\pi v_0}{2}\left(\frac{{v_{x0}}^2}{\omega P} + \frac{{v_{y0}}^2}{\omega P} + \frac{{v_{z0}}^2}{\omega P}\right)$ is the mass density factor

Equation (5) denotes that the fractional velocity change $\Delta v / v_0$ varies with operating frequency f_0.

An example of velocity and attenuation changes resulting from depositing a mass layer on a 97MHz SAW device using an ST-cut quartz substrate are shown in figure 3.17 [3.15]. As it can easily be observed velocity decreases linearly with thickness while the relative attenuation change $\Delta\alpha / k$ (where α is the attenuation and $k = 2\pi/\lambda$ is the wavenumber) due to mass loading is negligible in comparison with $\Delta v / v_0$ shown on the same scale.

The above analysed theoretical and experimental results section regarding mass loading effects were fully verified in our case. All the commercially available SAW filters were deposited with an active In_2O_{3-x} thin film on top of their structures.

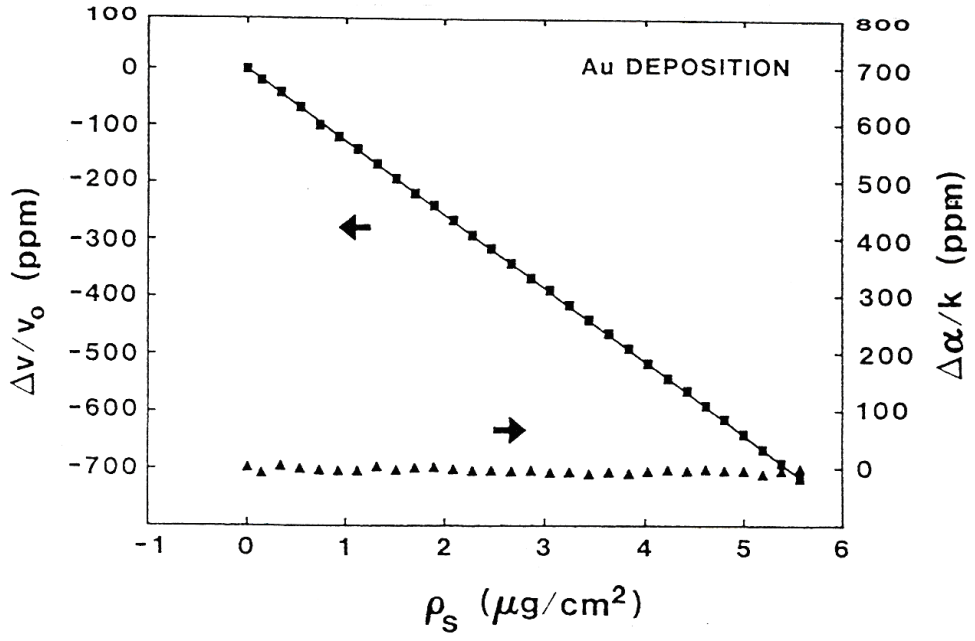

Figure 3.17: Fractional change in SAW propagation velocity and attenuation vs thickness of an evaporated metal film.

Figure 3.18 depicts a typical 934MHz SAW filter frequency response before (solid line) and after (dashed line) depositing a 100nm In_2O_{3-x} thin film. Following the theoretical predictions, film deposition causes a decrease in the wave velocity and this is the reason for observing a decrease in the oscillation frequency. A considerable frequency shift of ~20MHz was recorded for the specific filter followed by a negligible recorded attenuation. This frequency shift results from the difference between the frequencies that propagate with the minimum attenuation in each case. Similar results were obtained for all filter responses. This new shifted centre frequency arising from thin film deposition was taken as the reference point before any sensitivity measurements carried out.

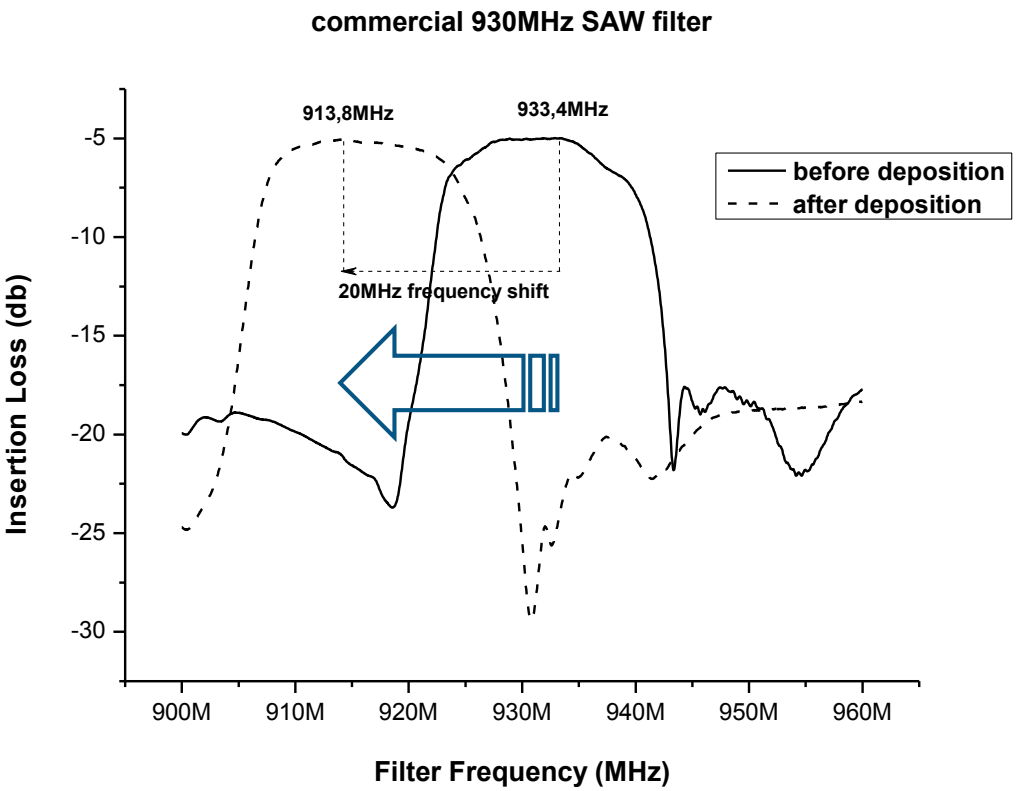

Figure 3.18: Frequency shift due to active layer deposition.

The central operating frequency behavior was examined towards consecutive 100nm In_2O_{3-x} thin film depositions. This was done for all SAW filter structures ranging from 139MHz-930MHz nominal frequency. It was found that all samples exhibited a linear decrease in their operating frequency with the surface mass density as observed in figure 3.19, thus verifying once more the respective theoretical predictions regarding mass loading.

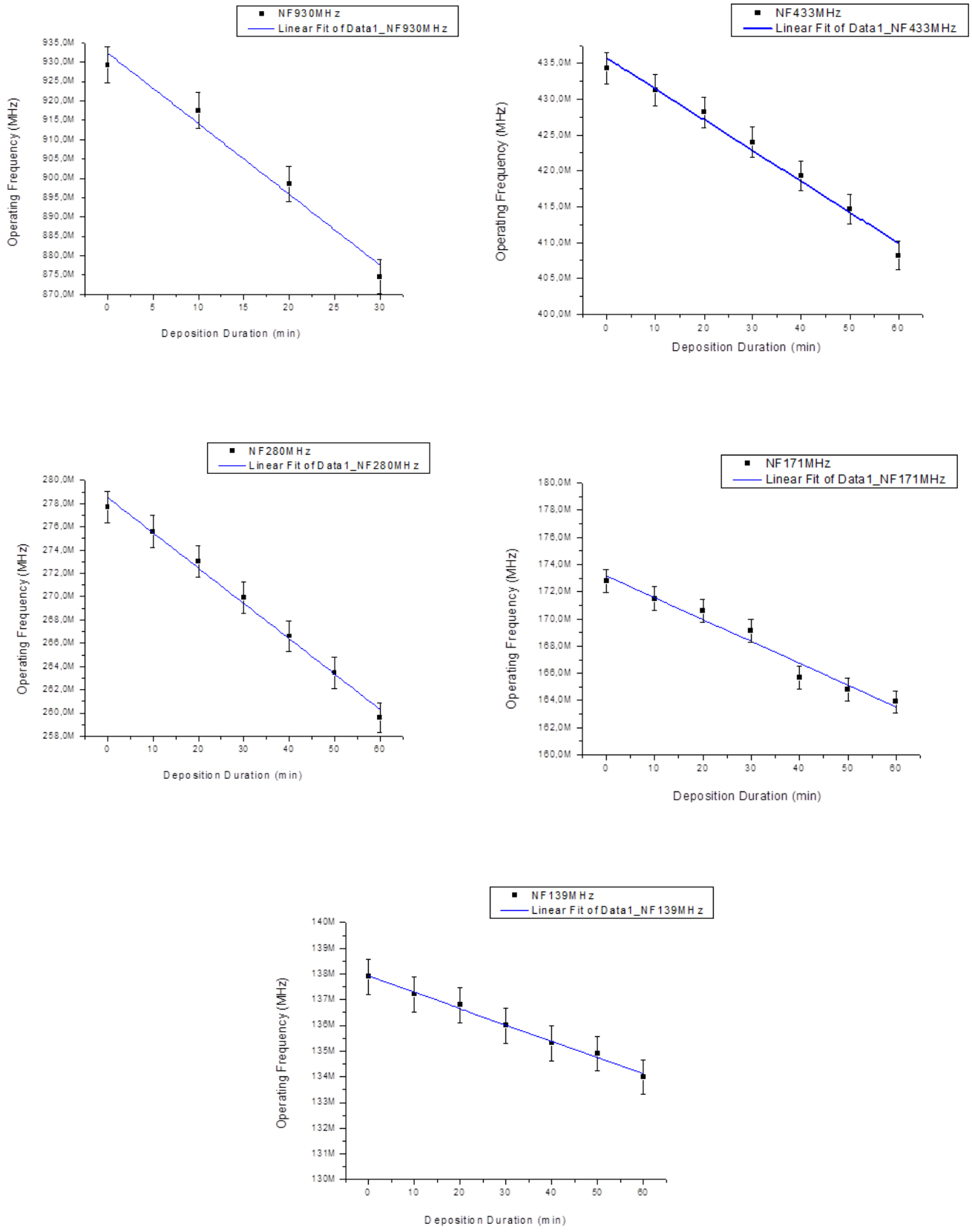

Figure 3.19: SAW filter central operating frequency dependence vs In_2O_{3-x} deposition duration-thickness.

Establishing that due to mass loading effect of the sensing film on the SAW devices their nominal operating frequencies do shift to a new value, any further changes during gas sensing should be associated with variations on the SAW surface conductivity. Such conductivity changes caused by the sorbed gas molecules should be taken into consideration in addition to the load mass effect due to the sensing film deposition. However, since in the case of gas sensors the mass loading caused by the sorbed gases particularly at the low ppm and ppb levels is negligible, any detected frequency shift should be attributed to variations in the film's surface conductivity [3.16]. Furthermore, unlike mass sensitivity, where the addition of mass on the sensor surface generally causes a decrease in frequency, sheet conductivity changes may cause either an increase or decrease in resonant frequency, depending on whether the analyte gas is respectively oxidizing or reducing. Therefore, the acoustoelectric response of a SAW filter becomes the prime sensing parameter that controls the film's gas sensitivity.

3.2.2.2 Verification of the "acoustoelectric response" on commercial SAW transducers

When a SAW propagates along the surface of a piezoelectric material, the mechanical wave is accompanied by a traveling electric field that interacts with charge carriers on or adjacent to the surface. Hence, the interaction between the gas molecules and the sensitive layer perturbs the electrical boundary conditions at the surface of the structure. As a result, the velocity and attenuation of the electromechanical waves are perturbed.

The effect of the coupling of wave and charge carriers can be illustrated by an equivalent circuit model shown below [3.15]:

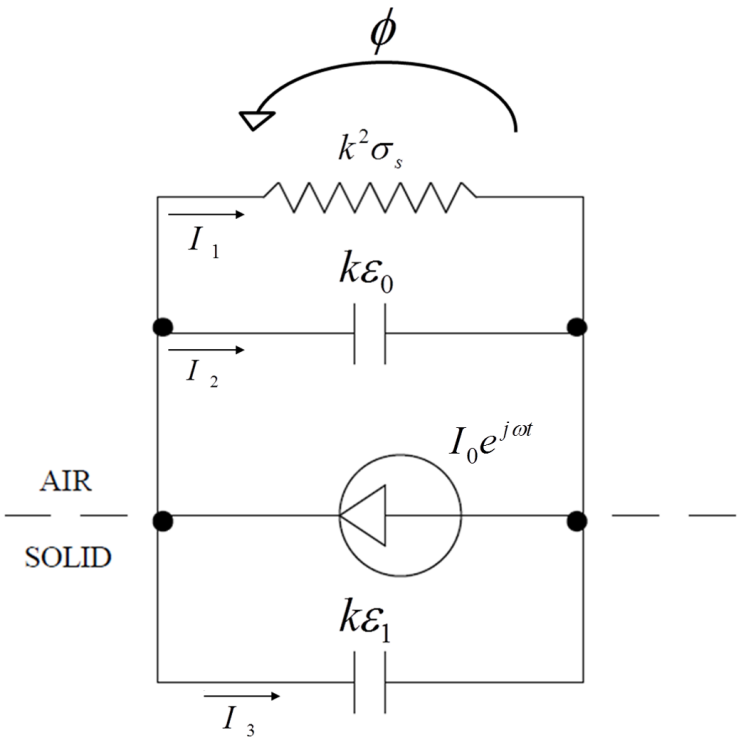

Figure 3.20: Equivalent circuit model for SAW "acoustoelectric response".

The current generated per unit area of surface, I_0 is given as:

$$I_0{}^2 = 2K^2\omega k^2(\varepsilon_0 + \varepsilon_s)P \qquad (1)$$

where,

K^2 is the electromechanical coupling coefficient

ε_0 and ε_s are air and substrate dielectric permittivities

k is the acoustic wavenumber

P is the power density

Displacement currents generated in the substrate and air arise from capacitances of $k\varepsilon_s$ and $k\varepsilon_0$ respectively.

Shunt conductance $k^2\sigma_s$ accounts for the conduction currents in the film overlay.

To derive the changes in the velocity and attenuation because of acoustoelectric coupling we will study two different cases

1. Without conductive film – In the absence of conductive film the energy generated by the wave gets stored in the evanescent electric field. The power flow in this case is given as,

$$P_{T1} = \frac{{I_0}^2}{2j\omega k(\varepsilon_0 + \varepsilon_s)} \quad (2)$$

2. With the conductive film, the power flow becomes,

$$P_{T2} = \frac{{I_0}^2}{2[k^2\sigma_s + j\omega k(\varepsilon_0 + \varepsilon_s)]} \quad (3)$$

The total "acoustoelectric response" is nothing but the difference between the two power flows, which entirely depend on the film conductivity

$$P_T = P_{T2} - P_{T1} = -\frac{{I_0}^2}{2}\frac{k^2\sigma_s}{j\omega k c_s(k^2\sigma_s + j\omega k c_s)} \quad (4)$$

where $c_s = \varepsilon_0 + \varepsilon_s$

Substituting equation for ${I_0}^2$ into equation (4) and taking into account the changes in the complex propagation factor γ caused by a generalized perturbation

$$\Delta\gamma = \frac{\Delta\alpha}{k_0} - j\frac{\Delta v}{v_0} = \frac{P_T}{2k_0 P}$$

and by equating real and imaginary parts we end up with two equations depicting that acoustoelectric coupling results in both wave velocity and attenuation alterations:

$$\frac{\Delta v}{v_0} = -\frac{K^2}{2}\frac{{\sigma_s}^2}{{\sigma_s}^2 + (v_0 c_s)^2} \quad \textit{(velocity)}$$

$$\frac{\Delta \alpha}{k} = \frac{K^2}{2}\frac{v_0 c_s \sigma_s}{{\sigma_s}^2 + (v_0 c_s)^2} \quad \textit{(attenuation)}$$

Plot of the above mentioned equations (Fig. 3.21) reveal that the wave velocity decreases monotonically as sheet conductivity of the film increases while attenuation goes through a peak [3.15]. The peak in attenuation ($\frac{\Delta \alpha}{k} = \frac{K^2}{4}$) which concurs with the maximum rate of velocity decrease happens when the sheet conductivity equals the critical value $\sigma_s = \sigma_c = v_0 c_s$.

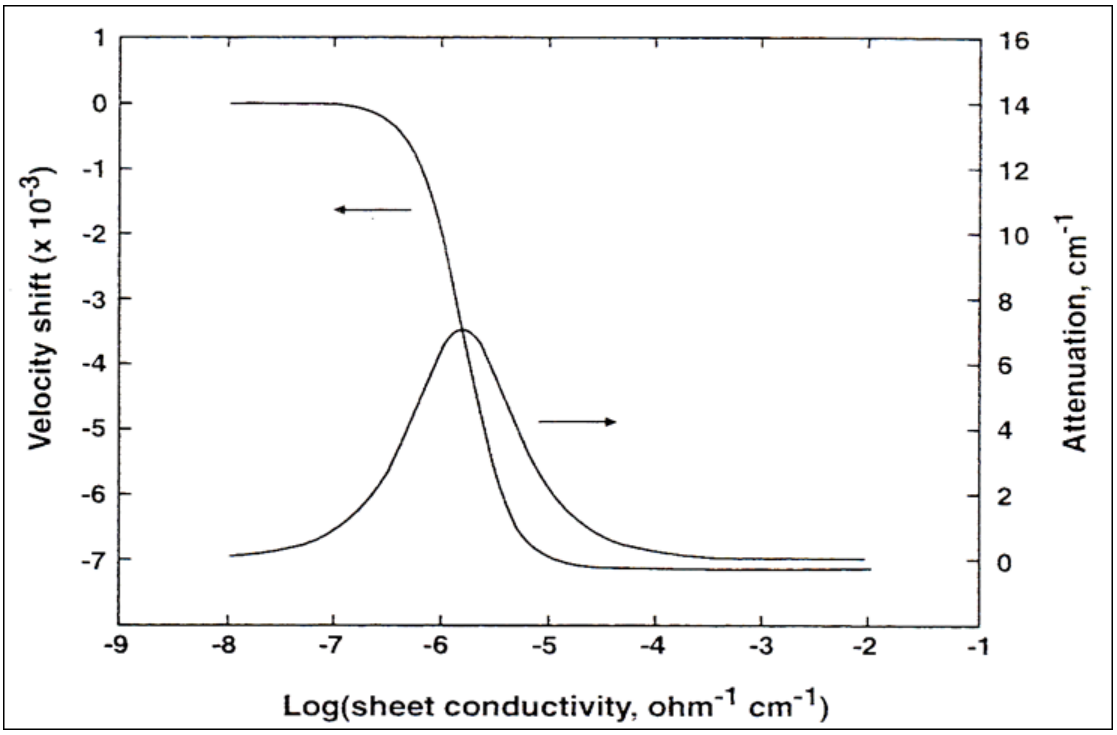

Figure 3.21: Acoustoelectric interaction.

Furthermore the above mentioned equations imply that for larger K^2 at the device surface the influence of sheet conductive changes on the

acoustic wave velocity is greater. K^2 is a measure of how strongly the electrical potential and mechanical displacements associated with a wave interact and is substrate dependent. Table 2 gives values of K^2, as well as unperturbed wave velocity v_0 and capacitance c_s per unit length.

The "acoustoelectric response" can be very significant with SAW devices, particularly those using strongly piezoelectric substrates. In fact, the "acoustoelectric response" can be much greater than the mass loading response in certain circumstances.

All our samples incorporated materials with strong piezoelectric properties such as $LiNbO_3$ and $LiTaO_3$ employed in the commercially available SAW filters.

Substrate Cut Propagation Direction	v_0 ($\times 10^5$cm/sec)	$K^2(\%)$	c_s (pF/cm)
Quartz ST X	3.158	0.11	0.5
$LiNbO_3$ Y Z	3.488	4.8	4.6
$LiTaO_3$ MDC -	3.37	1.6	4.4
Gallium Arsenide Z X+22.5°	2.763	0.022	1.2

Table 3.2: Acoustoelectric properties of SAW substrate materials.

In addition to the mass loading results, SAW filters responses were tested over a range of operating temperatures and towards reducing and oxidizing gases such as H_2 and NO_2 respectively, with varying concentrations, in order to examine their acoustoelectric behaviour with respect to the theoretical predictions. Figures 3.22 and 3.23 illustrate that in the presence of a reducing gas such as H_2 film conductivity increases therefore the acoustic wave velocity decreases followed by a respective decrease in the filter's centre frequency while in the presence

of an oxidizing gas such as NO_2 opposite phenomena take place thus completely verifying the theoretical predictions.

Strong frequency shifts as high as 225kHz and 450kHz were observed towards 10000ppm H_2 and 8.5ppm NO_2 respectively at 100°C, while a 300kHz frequency shift has been recorded for the above mentioned H_2 and NO_2 concentrations at 160°C, as far as the 930MHZ nominal frequency SAW filter is concerned.

Similar results have been obtained from the 280MHz nominal frequency SAW filter. Frequency shifts of 19kHz and 37.5kHz have been recorded towards 10000ppm H_2 and 8.5ppm NO_2 respectively at 100°C, while the same 19kHz frequency shift has been observed for the above mentioned concentrations at 155°C.

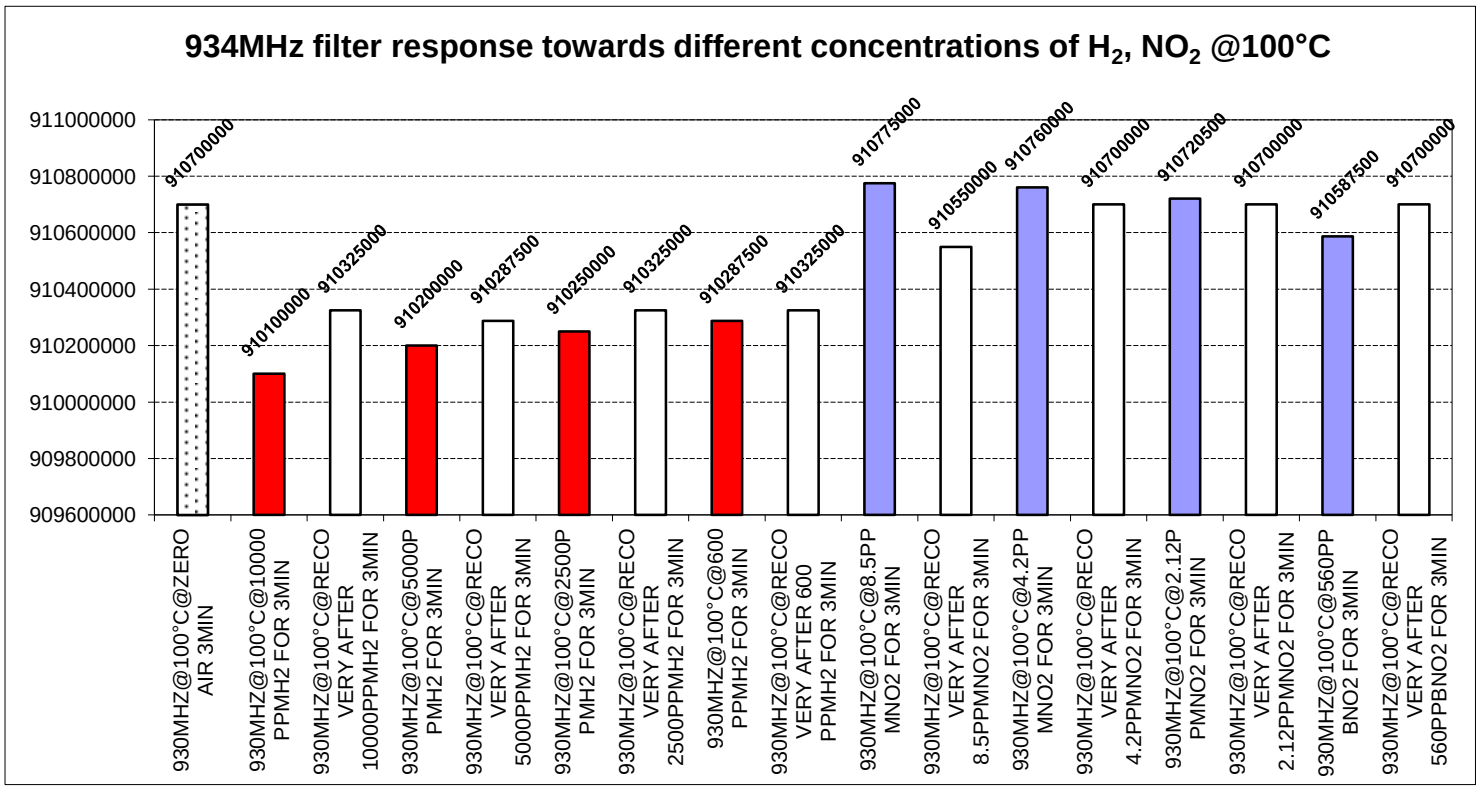

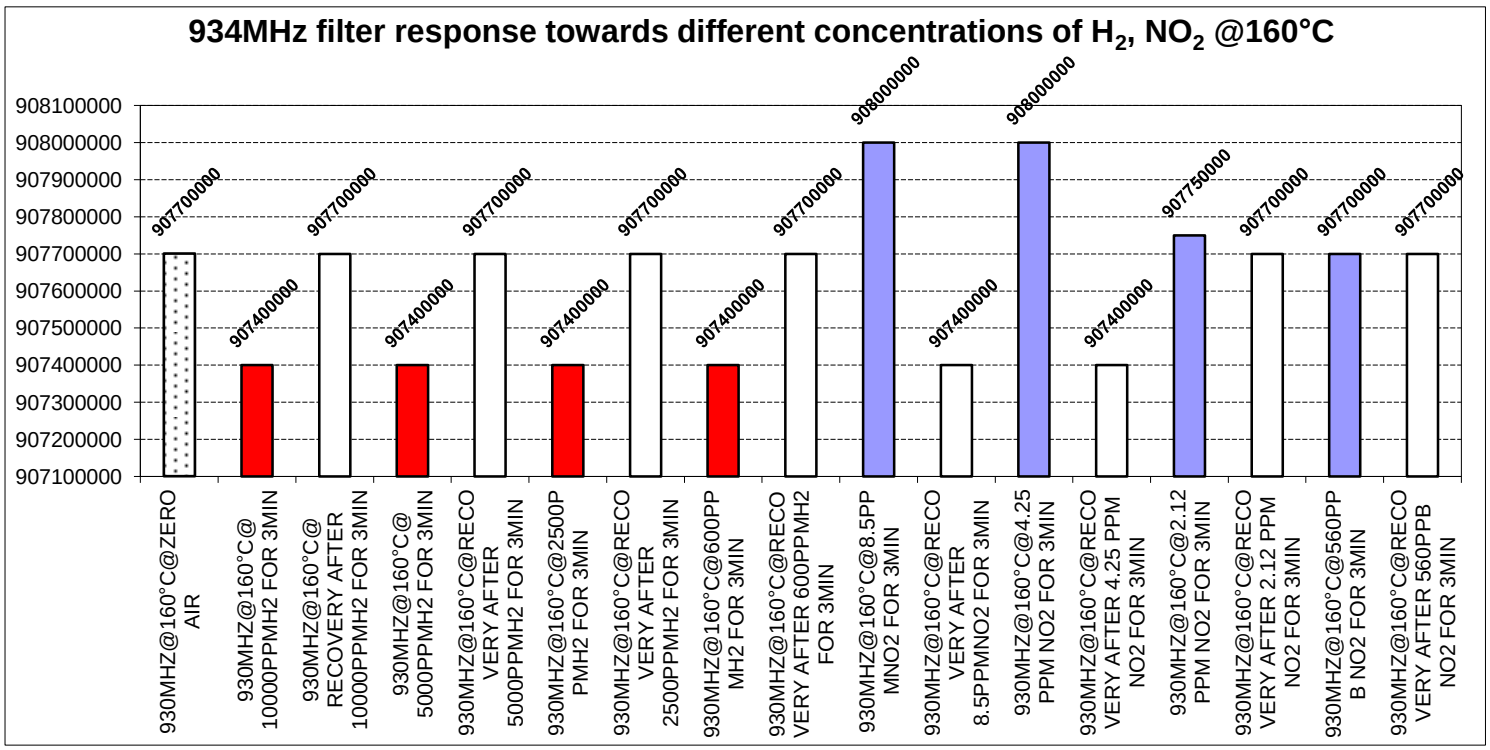

Figure 3.22: Recorded responses of a commercially available SAW filter operating at NF934MHz, utilizing 100nm In_2O_{3-x} as selective layer on top, tested at 100° and 160°C.

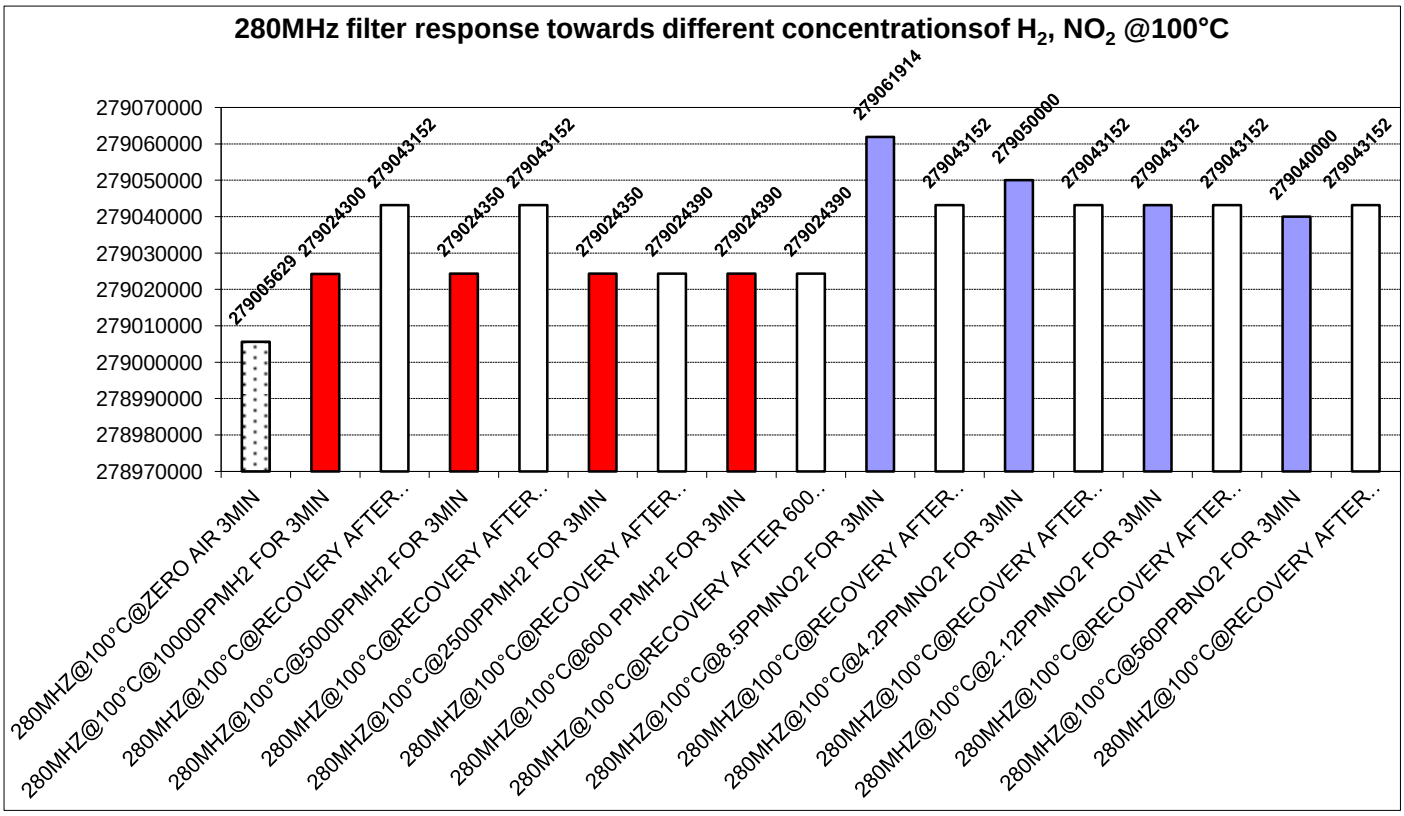

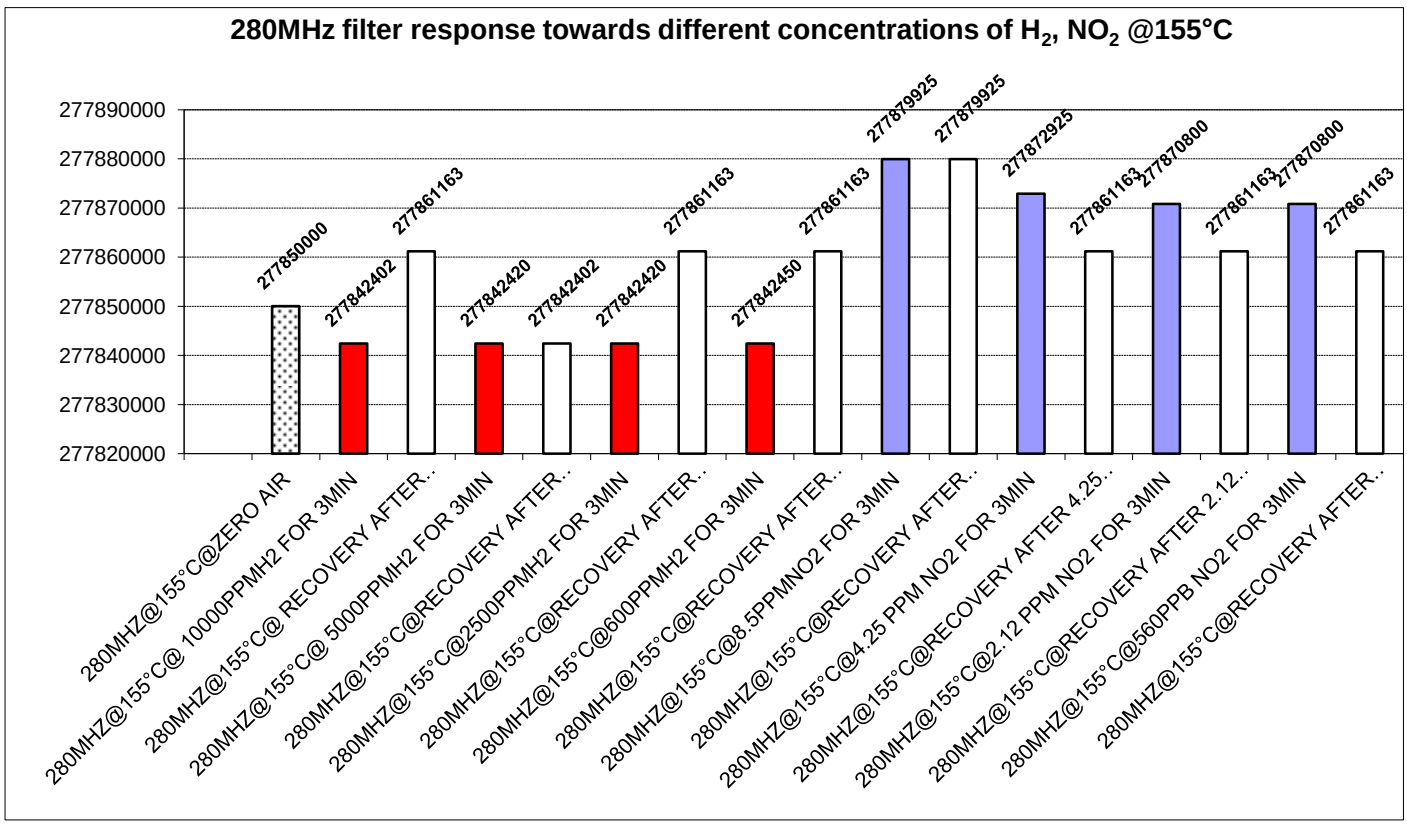

Figure 3.23: Recorded responses of a commercially available SAW filter operating at NF280MHz, utilizing 100nm In_2O_{3-x} as selective layer on top, tested at 100° and 155°C.

The above measurements and corresponding graphs were taken by means of a network analyzer using the cell shown in figure 3.4. Though a network analyzer may not be convenient for routine laboratory raw measurements of real-time perturbations, it is a very useful tool for monitoring both the velocity and attenuation simultaneously.

Experiments were repeated this time using a Fluke PM6680B timer and frequency counter which through a GPIB interface connection with a computer provided continuous raw oscillation frequency data.

The filter responses were tested over a range of operating temperatures, and towards reducing and oxidizing gases such as H_2 and NO_2 respectively, with varying concentrations. Figure 3.24 shows a typical response of a 280MHz SAW filter towards increasing NO_2 concentrations at 160°C while figure 3.25 exhibits the same filter response towards increasing H_2 levels at the same temperature. In the time interval between two consecutive gas concentrations, synthetic air was introduced into the chamber for the recovery of the sensor. Once more it is evident that in the presence of oxidizing agents such as NO_2, the operating frequency increases while in the presence of reducing gases the opposite phenomenon takes place.

It is worth noticing that, with these high frequency SAW devices, detection of NO_2 and H_2 is feasible at concentrations of the order of 0.5 - 0.6ppm at a relatively medium operating temperature of 160°C. Such low detection limits although moderate for H_2 are particularly important for NO_2 as they indicate a sensitivity limit far below the values attainable by the current electrochemical sensor of 3ppm [3.17] which is often used for detection of NO_2.

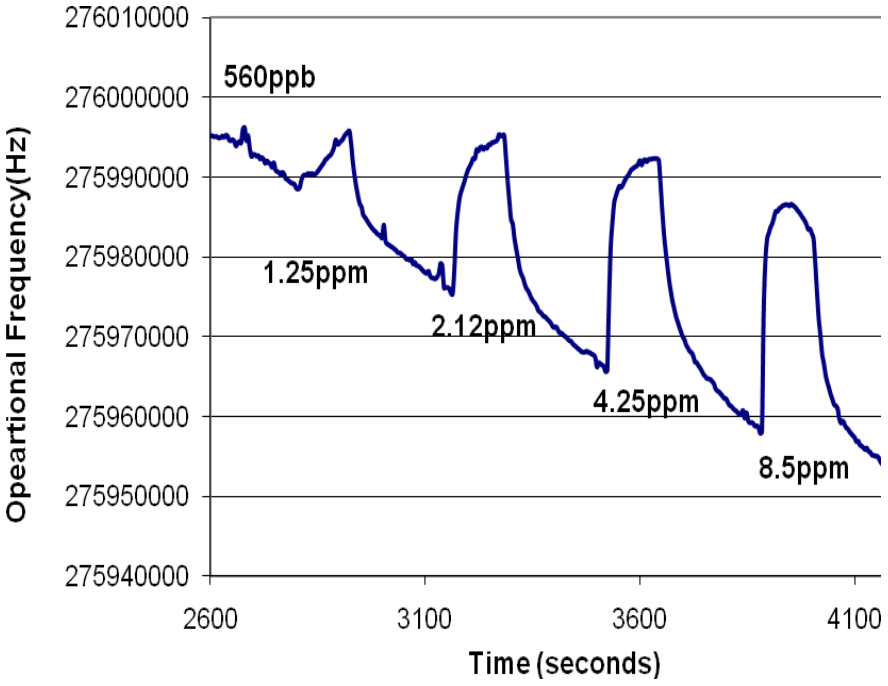

Figure 3.24: 280MHz Saw Filter response towards different NO_2 concentrations at 160°C.

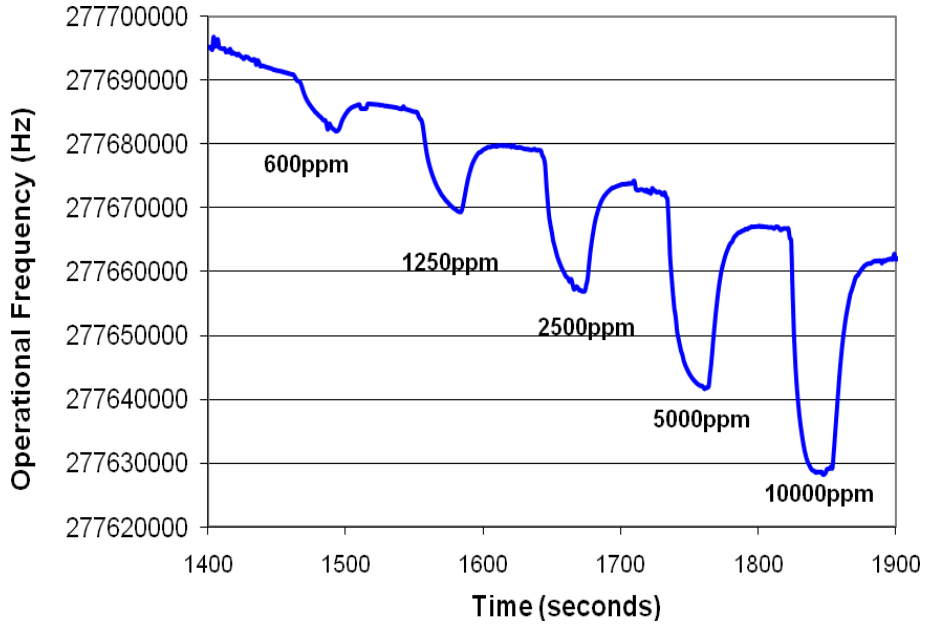

Figure 3.25: 280MHz Saw Filter response towards different H_2 concentrations at 160°C.

Additional sensitivity measurements were carried out utilizing FORTH's equipment. SAW filters sitting on a power resistor which was connected to a temperature controller for elevating temperatures, were examined towards well controlled ozone concentrations produced be a Thermo 49i ozone analyzer with a range capacity of 0-0.05 to 1ppm. An electronic "printed circuit board" (PCB) was fabricated in order to achieve both temperature elevation and signal transfer from the filters under test to a Network Analyzer (Agilent, model E5061A, 300KHz-1.5GHz). A labview program was developed in order to monitor continuously the filter's centre frequency variations therefore allowing raw data acquisition. This time the oxidizing atmosphere was solely achieved through the well controlled ozone concentrations while the conducting state of the sensitive In_2O_{3-x} sensitive layer was acieved through photoreduction by using a UV pencil style lamp with average intensity of 4mW/cm^2. A more detailed description of the apparatus is depicted in figure 3.26

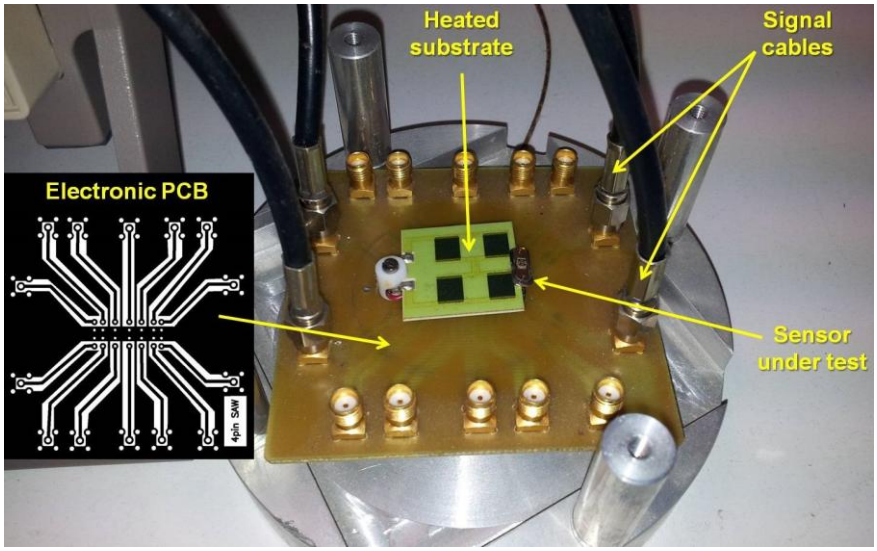

Figure 3.26: Experimental setup with the electronic PCB configuration for SAW filter measurements.

A SAW filter operating at a nominal frequency of 934MHz was sputtered with a 100nm In_2O_{3-x} sensitive layer on top. After the deposition the filter's osillation frequency decreased to 910MHz, as expected theoretically, due to the weight of the film. This new shifted centre

frequency was taken as the reference point for detecting future acoustic wave velocity variations. Figure 3.27 reveals centre frequency variations towards consecutive photoreduction and oxidizing cycles against four different ozone concentrations of 190, 680, 1146 and 1540ppb. In each 20min cycle, the photoreduction of the film lasted 5min while the oxidation process (recovery) lasted 15min since it is well known that it is a much slower process. The gas flow rate was kept the same at 300ml for both processes and during all cycles under RT conditions. In the case of photoreduction the flowing gas was N_2 while in the case of oxidization the gas was ozone with the aforementioned concentrations. As can be seen the higher the ozone concentration the larger the increase in the filter's centre frequency. Once more clear responses and well separated signals have obtained against the different minute ozone concentrations.

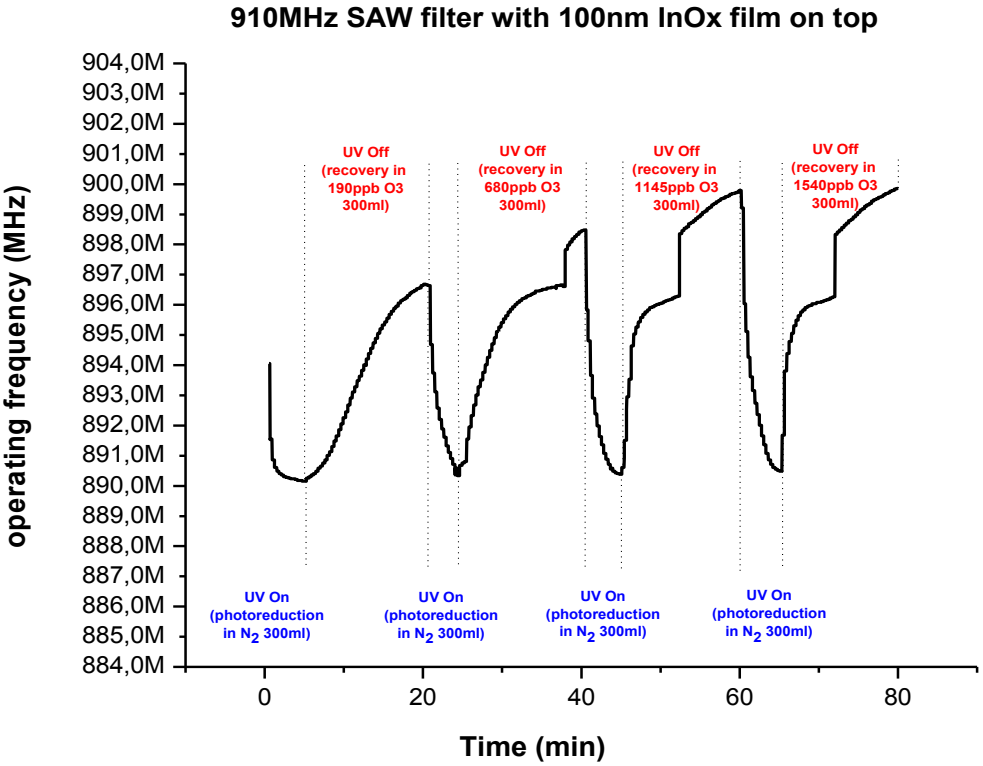

Figure 3.27: Consecutive photoreduction-oxidation cycles under different ozone pulses ranging from 190-1540ppb. Gas flow was kept constant at 300ml.

In addition figure 3.28 reveals the same filter's response towards repetitive 1ppm ozone pulses in synthetic air at 150°C. This time the frequency variations were only due to the presence and absence of the oxidizing gas. No photoreduction effect took place and the sensitivity experiment took place under 300ml of alternating ozone and synthetic air flow rates. Although vast frequency shifts of the order of 9MHz, compared to the previous situation, could not be recorded, adequate frequency variations of 2MHz with remarkable repeatability were obtained indicating once more the potential of the material to detect extremely low ozone concentrations.

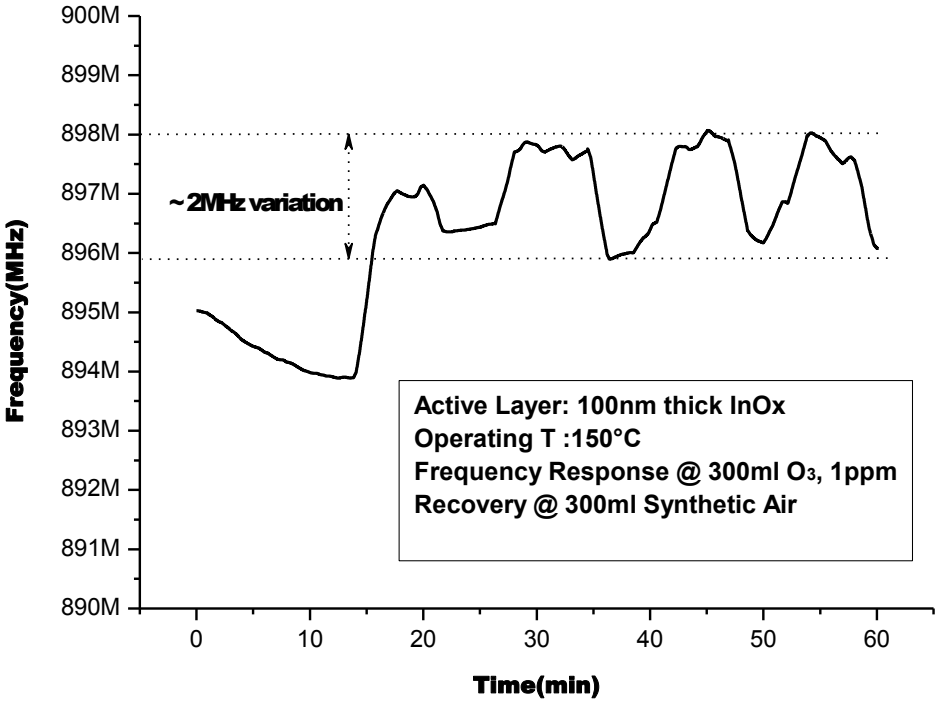

Figure 3.28: Response of a high operating frequency (910MHz) SAW filter utilizing 100nm thick In_2O_{3-x} active layer towards repetitive 1ppm ozone pulses in synthetic air, at 150°C.

References

[3.1] Lord Rayleigh, "On Waves Propagated along the Plane Surface of an Elastic Solid" *Proc. London Math. Soc.* 17 (1885), 4-11

[3.2] H. Wohltjen, R. Dessy "Surface acoustic wave probes for chemical analysis. II. Gas chromatography detector" *Anal. Chem.*, 1979, 51 (9), pp 1465–1470.

[3.3] J.W. Grate, S.J. Martin, R.M. White, "Acoustic Wave Microsensors", *Anal. Chem.*, 1993, 65 (21), pp 940A–948A.

[3.4] A. D'Amico, A. Palma, E. Verona, "Surface acoustic wave hydrogen sensor", *Sensors and Actuators*, Volume 3, 1982–1983, Pages 31-39.

[3.5] A. D'Amico, A. Palma, E. Verona, "Hydrogen sensor using a palladium coated surface acoustic wave delay-line", *Proceedings of the IEEE,* Ultrasonics Symposium 1982, 308–311

[3.6] M.S. Nieuwenhuizen, A.J. Nederlof, "A SAW gas sensor for carbon dioxide and water. Preliminary experiments", *Sensors and Actuators B: Chemical*, Vol.2, Issue 2, (1990), 97-101.

[3.7] J.D. Galipeau, R.S. Falconer, J.F. Vetelino, J.J. Caron, E.L. Wittman, M.G. Schweyer, J.C. Andle, "Theory, design and operation of a surface acoustic wave hydrogen sulfide microsensor", *Sensors and Actuators B: Chemica,l* Vol. 24, Issues 1–3, (1995), 49–53.

[3.8] M. Penza, L. Vasanelli, "SAW NO_x gas sensor using WO_3 thin-film sensitive coating", *Sensors and Actuators B: Chemical*, Vol. 41, Issues 1–3, (1997), 31–36.

[3.9] M. Rapp, R. Stanzel, M.v. Schickfus, S. Hunklinger, H. Fuchs, W. Schrepp, H. Keller, B. Fleischmann "Gas detection in the ppb-range with a high frequency, high sensitivity surface acoustic wave device", *Thin Solid Films*, Vol. 210–211, Part 2, (1992), 474-476.

[3.10] D. Rebière, C. Déjous, J. Pistré, J.F. Lipskier, R. Planade, "Synthesis and evaluation of fluoropolyol isomers as saw microsensor coatings: role of humidity and temperature", *Sensors and Actuators B: Chemical*, Vol. 49, Issues 1–2, (1998), 139–145.

[3.11] H. Wohltjen, "Mechanism of operation and design considerations for surface acoustic wave device vapor sensors", *Sensors and Actuators* Vol. 5, Issue 4, (1984), 307-325.

[3.12] C.K. Campbell, "Surface Acoustic Wave Devices for Mobile and Wireless Communications", San Diego, USA: Academic Press; 1998.

[3.13] G. Kiriakidis, M. Bender, N. Katsarakis, E. Gagaoudakis, E. Hourdakis, E. Douloufakis, V. Cimalla, "Ozone Sensing Properties of Polycrystalline Indium Oxide Films at Room Temperature", *Phys. Stat. Sol. (a)*, 185, No1, 27-32, (2001).

[3.14] S.J. Ippolito, S. Kandasamya, K. Kalantar-zadeh, W. Wlodarski, K. Galatsis, G. Kiriakidis, N. Katsarakis, M. Suchea, "Highly sensitive layered ZnO/LiNbO3 SAW device with InOx selective layer for NO_2 and H_2 gas sensing", *Sensors and Actuators B* 111–112 (2005), 207–212.

[3.15] D.S. Ballantine, R.M. White, S.J. Martin, A.J. Ricco, E.T. Zellers, G.C. Frye, H. Wohltjen, "Acoustic Wave Sensors: Theory, Design and Physico-Chemical Applications", Academic Press, New York, 1997.

[3.16] L. Fan, F. M. Zhou, C. Wang, H. D. Gao, S.Y. Zhang, H. Zhang, X.B. Wang "Influence of surface conductivity on sensitivity of acoustic wave gas sensors based on multilayered structures", *IEEE Transactions on Ultrasonics, Ferroelectrics and Frequency Control,* vol. 58, No2 (2011)

[3.17] Y. Mizutani, H Matsuda, T Ishiji, N Furuya, K Takahashi, "Improvement of electrochemical NO_2 sensor by use of carbon–fluorocarbon gas permeable electrode", *Sensors and Actuators B* 108 (2005), 815–819.

4. Conclusions

The first part of this work has been dedicated to an extensive research on the selection of the suitable metal-oxide material to be deposited as active layer on top of surface acoustic wave structures and devices for sensing minute hazardous gas concentrations.

Among the vast variety of metal-oxides available, we have focused on In_2O_{3-x} and ZnO. The motive behind this lied on previous work on both materials which revealed not only high conductivity changes upon photoreduction and subsequent oxidation in ozone atmosphere but also unique structural properties. In general, semiconductor oxides are non-stoichiometric in which the oxygen vacancies are the main bulk point defects. This non-stoichiometric characteristic makes them very active in "redox" reactions since the electron configuration of the solid can be altered. Due to the material's oxygen deficient surface strong reaction of the material with oxidizing species is expected and therefore a subsequent reduction process, as a rule, leads to the formation of free carriers, which greatly increase the material's conductivity, a fact that is crucial for sensor applications.

In_2O_{3-x} thin films were deposited via DC Magnetron Sputtering using an In metallic target while ZnO thin films were deposited via the Aerosol Spray Pyrolysis (ASP) technique, using a home-made apparatus, and via DC Magnetron Sputtering, same as for In_2O_3 films, using both metallic Zn as well as ceramic ZnO targets. DC Magnetron Sputtering technique was preferred among others due to process stability, excellent film properties and gained experience through years of depositing various metal-oxides. On the other hand ASP provided an alternative, cost effective technique for depositing ZnO films with inherent structural properties and their influence on material's sensitivity to be upon investigation.

As far as the ZnO films prepared by DC Magnetron Sputtering are concerned, the effect of plasma gas flow ratio (Ar to O_2) on the

morphology of ZnO thin films and their correlation with the optical properties and conductivity changes of the films were investigated. AFM and XRD characterization of the films revealed polycrystalline morphology with roughness increasing as the argon partial pressure increases. The surface of the films grown from ceramic targets had a complete different morphology, which is mainly dominated by grain agglomeration and the presence of very tall features. ZnO films sputtered from a metallic target in pure oxygen plasma show smaller grains and smaller E_{gap}. Moreover, they exhibit better sensitivity to ozone due to larger surface-to-volume ratio. On the contrary, films sputtered from a ceramic target at high Ar concentration in the plasma exhibit larger E_{gap}, better conductivity and much worse sensitivity to ozone. Notwithstanding the above, when the films were exposed to different ozone concentrations and the exponential decay curves were plotted in a normalized form, it was apparent that there was no clear distinction between the different ozone levels, denoting a major drawback of the subject films in detecting specific accurate ozone concentrations.

Unlike their sputtered counterparts, ZnO films produced via ASP exhibited clear response signals to different ozone concentrations as low as 16ppb with a satisfactory resolution of 5% compared to synthetic air even within the first minute of exposure. Such detection limits of 16ppb for spray pyrolysis films, at room temperature, are, to the best of our knowledge, the lowest ever reported to the open literature. In order to verify these results, measurements have been reiterated giving the same outcome. Structural analysis (XRD, TEM, and SEM) carried out on these films revealed a highly porous surface structure for the ASP samples with agglomerated grains sized on average 80nm i.e. well within the range of those produced by sputtering (40nm). This combination of fine grain sizes together with a high porosity with porous

sizes of the same order (~100nm) plays a crucial role in the material's ability to yield adequate responses in the low-ppb range.

Finally, from the material's point of view, In_2O_{3-x} was the last material to be investigated before proceeding to the active layer deposition on top of SAW structures and devices. Structural analysis utilizing cross-section TEM carried out in these films revealed a crystalline columnar morphology which is an inherent property of the growth technique independent of the selected substrate. The mean width of the columnar grains was estimated to be 20nm with a preferred [111] orientation. The dynamic ability of the material itself to provide reliable readouts even at the extremely low ozone concentration of 6ppb has been demonstrated together with the remarkable repeatability (produced the same signal under the same conditions) and reproducibility (sensor recovery back to its original background conditions) of the results. Again, this was, to the best of our knowledge, the first time that such extremely low ozone sensing levels have been reported for metal oxide films at room temperature (RT) on flexible substrates.

Furthermore, ageing characteristics of In_2O_{3-x} films were investigated. In particular, selected samples were re-evaluated in terms of surface structure, optical and electrical properties seven years after their deposition date. It was shown that material's structural characteristics such as transparency, surface morphology, crystallinity, and optical bandgap were largely remained unaffected with time. In addition, the very strong recorded conductivity changes of up to 8 orders of magnitude, even seven years after film's fabrication date on these samples (upon photoreduction with UV light and subsequent oxidation in ozone atmosphere) revealed the material's potential use as an effective and reliable ageing resistant O_3 sensor.

Having already achieved such extra low sensing levels using conventional conductometric methods, we proceeded in adopting In_2O_{3-x}, as the active layer on top of SAW structures and devices in order to achieve further enhancement or at list similar sensitivity levels

this time applying a more device oriented scenario. This was implemented by employing two major approaches with their corresponding setups, i.e. layered SAW devices (delay line structures) and commercially available SAW filters operating at various nominal frequencies. Propagation of a surface acoustic wave along a piezoelectric solid yields both mechanical deformation and electric potential. Therefore both mechanical and electrical coupling between the SAW and the film are possible giving rise to two major interactions "mass loading" and "acoustoelectric response".

As far as "mass loading" is concerned, it becomes significant when depositing the active In_2O_{3-x} layer on top of SAW devices producing a linear decrease of the filter's oscillation frequency with increased material's thickness (increased material's weight). This is consistent with the theoretical predictions while it becomes insignificant in the case of gas sensing procedure where the mass loading caused by the sorbed gas particularly at the low-ppm or ppb range is negligible and the detected frequency shifts are associated with conductivity changes.

As far as "acoustoelectric response" is concerned, as interaction with an analyte increases the conductivity of the coating film (reducing gases) then the acoustic wave velocity decreases and this is the reason for observing a decrease in the oscillation frequency. The opposite rationale applies in the presence of oxidizing gases.

Frequency shifts of 73.5kHz at 510ppb NO_2 and 78.5kHz at 600ppm H_2 as well as 319.4kHz at 10000ppm H_2 have been recorded for the 20nm In_2O_{3-x} sensor at 168°C, while shifts of 31.5kHz at 10ppb O_3 and 78.5kHz at 25ppb O_3 were recorded for the 100nm In_2O_{3-x} sensor at 160°C as far as layered SAW delay line structures are concerned.

Similar results have been obtained with SAW filters exhibiting approximately a frequency shift of 300kHz at both 8.5ppm NO_2 and 600ppm H_2 at 160°C for the 930MHz filter employing a 100nm In_2O_{3-x} active layer. An exceptionally strong frequency shift of the order of 2MHz was recorded for the same filter at an operating temperature of

150°C towards 1ppm O_3 under an alternating flow of 300ml between ozone and synthetic air pulses exhibiting a fully reversible sensing behavior.

Consequently, the SAW sensors examined exhibited high electro-mechanical coupling which is advantageous for many gas sensing dedicated applications in the field of indoor air-quality control and in commercial certified ventilation systems. On the other hand, one may look forward to expand the sensing capabilities of the SAW sensors to higher frequencies i.e. in the GHz regime which is of paramount importance for basic research such as in single electron devices for metrology applications as well as for consumer-product applications like wireless LAN with frequencies around 5GHz already commercially available.